



POLITECNICO DI TORINO
MSc in Aerospace Engineering

Master's Degree Thesis

**Monitorization of the relative Minimum
Orbital Intersection Distance (MOID)
between terrestrial orbits**

Author: Massimiliano Gorno

Tutor: Manuela Battipede

July 2019

Abstract

This final work presents a new tool for the rapid calculation of the Minimum Orbital Intersection Distance (MOID) evolution between objects orbiting the Earth. It is primarily intended as a filtering stage (the second filtering stage proposed by Hoots) for the assessment of the collision risk between a selected object and a huge number of detected and potentially dangerous space debris.

The tool combines:

- The speed of a new orbit propagator developed by the Space Dynamics Group of the Technical University of Madrid (SDG-UPM) called DROMO (SDG-DROMO);
- The rapidity of MOID computation given by a new available routine developed by the same group (SDG-MOID).

The result is a routine (SDG-DROMOID) which sequentially applies the former tools. This modular design guarantees the possibility of an easy replacement of any of the tools whenever an improved versions were available.

Briefly, the *modus operandi* is the following:

1. Download of the TLE list given by the NORAD for a huge number of space debris (ideally all the public objects tracked by the NORAD).
2. Propagation of every object and the primary object for a given period of time. This propagation passage is made considering only the *Main Problem* (the analysis of the perturbed motion of an object under the influence of the J_2 term of the Geopotential expansion).
3. Calculation of the MOID at every step of time where the two objects osculating orbits are available.
4. Record of the evolution of the MOID between the primary and the space debris given by the NORAD in the studied period of time.
5. Analysis of the MOID variation in the selected period and possible conclusions that could be drawn (MOID decrease or increase, global minimum of the MOID, ability to discard objects without any possibility of impact in the considered period).

Between all spacecraft, the International Space Station (ISS) is an object of particular interest for its relevance. For this reason, the method is developed and tested using the ISS as main target.

Acknowledgements

I would like to thank my thesis Supervisor, Prof. José Manuel Hedo Rodríguez, of the Escuela Técnica Superior de Ingeniería Aeronáutica y del Espacio, Universidad Politécnica de Madrid, for his invaluable support in this work. His teachings, from computational programming to Mechanics and Astrodynamics constituted a conspicuous contribution to my formation as an Aerospace Engineer. I really appreciate his vast knowledge and intellectual honesty.

I would also like to thank my thesis Academic Tutor, Prof. Jesús Peláez Álvarez of ETSIAE-UPM as well, for proposing me this interesting thesis topic and for introducing me to the fascinating subject of Astrodynamics.

I would express my gratitude to my Family, for believing in my dreams and projects and for their total support during these years full of sacrifice and satisfactions. Thanks also to all my Friends in Brescia, Torino and Madrid for accompanying me in this great adventure.

Finally, my biggest thanks go to Marta, whose patience and optimism have resulted essentials to the good outcome of this work.

Per Aspera Ad Astra

Massimiliano Gorno

Contents

| | | |
|----------|--|-----------|
| 1 | The Space Debris problem | 14 |
| 1.1 | The origin of space debris | 14 |
| 1.2 | Risks for active spacecraft | 17 |
| 1.3 | A current method for threatening space encounters assessment | 18 |
| 1.4 | Aim of this work | 19 |
| 2 | Source of the data | 20 |
| 2.1 | The Two Line Element Set | 20 |
| 2.2 | Data Processing | 25 |
| 2.2.1 | Propagation Models | 25 |
| 2.2.2 | SGP4/SDP4 Model | 25 |
| 2.2.3 | SGP4/SDP4 Reference Frame | 26 |
| 2.3 | TEME to GCRF conversion | 26 |
| 2.3.1 | Precession and Nutation | 26 |
| 2.3.2 | Transformations | 27 |
| 2.3.3 | TEME to TOD transformation, Equation of the Equinoxes | 28 |
| 2.3.4 | TOD to MOD transformation: Nutation | 30 |
| 2.3.5 | MOD to GCRF transformation: Precession | 32 |
| 2.3.6 | TEME to GCRF complete transformation | 34 |
| 3 | Propagation based on DROMO | 36 |
| 3.1 | Space perturbations | 36 |
| 3.2 | The Earth Gravitational Field | 37 |
| 3.3 | DROMO propagator | 39 |
| 3.3.1 | Geometric and kinematic aspects of DROMO | 39 |
| 3.3.2 | DROMO variables definition | 41 |
| 3.3.3 | Initial conditions | 44 |
| 3.3.4 | From DROMO variables to the state vector | 45 |
| 3.4 | DROMO propagator implementation | 45 |
| 3.4.1 | DROMO formulation of the <i>main problem</i> | 45 |
| 3.4.2 | Propagation | 47 |
| 3.5 | Propagation results | 49 |
| 4 | MOID calculation | 50 |
| 4.1 | Basis of the method | 50 |
| 4.2 | Algorithm 1 | 51 |
| 4.2.1 | Distance computation | 52 |
| 4.2.2 | In-plane distance between a point and an ellipse | 52 |
| 4.2.3 | Parametric solution approach | 54 |
| 4.3 | Algorithm 2 | 56 |
| 4.3.1 | Discretization and minimum distance computation | 56 |
| 4.3.2 | Global minimum search | 56 |
| 4.4 | Implementation | 56 |

| | | |
|----------|--|-----------|
| 5 | Results analysis | 58 |
| 5.1 | DROMO theory and MOID computation implementation | 58 |
| 5.2 | Short term analysis | 60 |
| 5.3 | Long term analysis | 70 |
| 5.4 | Real time monitoring | 81 |
| 5.5 | Hazardous situations | 86 |
| 6 | Conclusions | 90 |
| 6.1 | Software development | 90 |
| 6.2 | MOID time evolution analysis | 90 |
| 6.3 | Future development | 91 |
| | Appendix A Discrete Fourier Transform | 94 |
| A.1 | Discrete Fourier Transform theory | 94 |
| A.2 | MOID evolution DFT | 95 |
| | Appendix B DROMO Asymptotic Solution | 98 |
| B.1 | Asymptotic solution theory | 98 |
| B.2 | Application and results | 99 |

List of Figures

| | | |
|------|--|----|
| 1.1 | Results of the Chinese ASAT test [2]. | 15 |
| 1.2 | Results of the Iridium-Cosmos 2251 collision of 2009 [3]. | 16 |
| 1.3 | Monthly Number of Cataloged Objects in Earth Orbit by Object Type [4]. | 16 |
| 1.4 | Sentinel-1A's solar array before and after the impact of a millimetre-sized particle [6]. | 17 |
| 2.1 | ISS TLE structure. | 22 |
| 2.2 | Example of a text file containing TLEs. | 23 |
| 2.3 | Precession and Nutation of the Earth's Equatorial Plane [17]. | 27 |
| 2.4 | Mean Equinox and True Equinox concepts. | 29 |
| 2.5 | Transformation Geometry Due to Nutation [17]. | 31 |
| 2.6 | The general precession connects the mean equinox of epoch, γ_0 , to the mean equinox of date γ_M [18]. | 33 |
| 2.7 | The precession angles connect the mean pole of epoch, \mathcal{P}_0 , to the mean pole of date, \mathcal{P} , ecliptic pole of epoch, \mathcal{C}_0 , and the ecliptic pole of date, \mathcal{C} [18]. | 34 |
| 3.1 | The kinds of spherical harmonics: (a) zonal, (b) sectoral, (c) tesseral. | 38 |
| 3.2 | Reference frames definition [22]. | 40 |
| 3.3 | Orbital Frame, Departure Frame and Departure Perifocal Frame [22]. | 41 |
| 3.4 | Linear interpolation scheme. | 48 |
| 3.5 | Propagation output line format. | 49 |
| 4.1 | Relative geometry of two confocal elliptical orbits [23]. | 50 |
| 4.2 | Distance from a point to an ellipse in \mathbb{R}^3 [23]. | 51 |
| 4.3 | In-plane distances between an ellipse and a coplanar point [23]. | 52 |
| 4.4 | Reference frames definition [23]. | 53 |
| 4.5 | Tangent lines to the plane evolute of an ellipse from an interior point [23]. | 54 |
| 4.6 | Geometry of the in-plane distance problem in parametric equations. [23] | 55 |
| 4.7 | MOID calculation output line format. | 57 |
| 5.1 | ISS MOID evolution of some representative debris during 1 day. | 59 |
| 5.2 | ISS MOID evolution of some representative debris during 1 day, MOIDs under 250 km. | 59 |
| 5.3 | Considered TLEs for the short term analysis. | 60 |
| 5.4 | Cosmos 2251 debris MOID to ISS evolution during 1 day. | 63 |
| 5.5 | Cosmos 2251 debris MOID to ISS evolution DFT. | 63 |
| 5.6 | Aurora 1 MOID to ISS evolution during 1 day. | 64 |
| 5.7 | Aurora 1 MOID to ISS evolution DFT. | 64 |
| 5.8 | Breeze M debris MOID to ISS evolution during 1 day. | 66 |
| 5.9 | Breeze M debris MOID to ISS evolution DFT. | 66 |
| 5.10 | Fengyun 1C debris MOID to ISS evolution during 1 day. | 68 |
| 5.11 | Fengyun 1C debris MOID to ISS evolution DFT. | 68 |
| 5.12 | Globalstar M046 MOID to ISS evolution during 1 day. | 69 |
| 5.13 | Globalstar MOID to ISS evolution DFT. | 69 |
| 5.14 | Considered TLEs for the long term analysis. | 70 |
| 5.15 | Cosmos 2251 MOID to ISS evolution over 1250 days. | 71 |
| 5.16 | Breeze M debris MOID to ISS evolution over 1250 days. | 74 |
| 5.17 | Breeze M debris MOID to ISS evolution during the first 300 days. | 75 |
| 5.18 | SYLDA MOID to ISS evolution over 1250 days. | 77 |
| 5.19 | SYLDA MOID to ISS evolution during the first 200 days. | 78 |
| 5.20 | Detailed view of SYLDA MOID to ISS evolution in 200 days for lower MOID values. | 79 |
| 5.21 | Falcon 9 Rocket Booster MOID to ISS evolution over 600 days. | 80 |

| | | |
|------|---|-----|
| 5.22 | Breeze M debris cloud MOID to ISS analysis over 14 days. | 82 |
| 5.23 | Breeze M debris cloud MOID to ISS analysis over 14 days (MOIDs under 125 km). | 83 |
| 5.24 | Iridium 33 debris cloud MOID to ISS analysis over 14 days (MOIDs under 125 km). | 83 |
| 5.25 | Cosmos 2251 debris cloud MOID to ISS analysis over 14 days (MOIDs under 50 km). | 84 |
| 5.26 | Fengyun 1C debris cloud MOID to ISS analysis over 14 days (MOIDs under 100 km). | 84 |
| 5.27 | Microsat R debris cloud MOID to ISS analysis over 14 days (MOIDs under 100 km). | 85 |
| 5.28 | A pair of close encountering space objects as reported by SOCRATES. | 86 |
| 5.29 | TLEs of the two objects with high probability of collision. | 86 |
| 5.30 | CBERS 1 DEB MOID to STEX evolution over 1 week since 2019, June the 16 th 12:00. | 87 |
| 5.31 | CBERS 1 DEB MOID to STEX evolution between day 5 and day 6 since 2019, June the 16 th 12:00. | 87 |
| B.1 | Radius vector | 101 |
| B.2 | Velocity vector | 102 |
| B.3 | Asymptotic solution error evolution over 1 day. | 103 |
| B.4 | Cowell's method error evolution over 1 day. | 103 |

List of Tables

| | | |
|---|--|-----|
| 1 | List of acronyms. | 11 |
| 2 | TLE characters meaning. | 24 |
| 3 | Selected EGM-96 coefficients. | 38 |
| 4 | DROMO non-dimensionalization characteristic values. | 42 |
| 5 | 3812 debris propagation and MOID calculation computational time. | 85 |
| 6 | Sample LEO object. | 100 |
| 7 | Comparison after 1 day propagation. | 101 |

Table 1: List of acronyms.

| Acronym | Meaning |
|-----------|---|
| AFSPC | Air Force Space Command |
| ASAT | Anti Satellite |
| CSSI | Center for Space Standard and Innovation |
| DAM | Debris Avoidance Manoeuvre |
| DFT | Discrete Fourier Transform |
| DoD | Department of Defense |
| EGM | Earth Gravity Model |
| EOP | Earth Orientation Parameter |
| ESA | European Space Agency |
| GAST | Greenwich Apparent Sidereal Time |
| GCRF | Geocentric Celestial Reference Frame |
| GEO | Geosynchronous Equatorial Orbit |
| GMST | Greenwich Mean Sidereal Time |
| GP | General Perturbations |
| IAU | International Astronomical Union |
| ISS | International Space Station |
| ITRF | International Terrestrial Reference Frame |
| IVP | Initial Value Problem |
| JSPOC | Joint Operations Center |
| LEO | Low Earth Orbit |
| MJD | Modified Julian Date |
| MOD | Mean (Equator) Of Date |
| MOID | Minimum Orbital Intersection Distance |
| NASA | National Aeronautics and Space Administration |
| NORAD | North American Aerospace Defense Command |
| ODE | Ordinary Differential Equations |
| PEF | Pseudo Earth Fixed |
| RAAN | Right Ascension of the Ascending Node |
| RK4 | Runge-Kutta (of) 4 th (order) |
| SATCAT | Satellite Catalog |
| SDG | Space Dynamics Group |
| SGP | Simplified General Perturbations |
| SOCRATES | Satellite Orbital Conjunction Reports Assessing Threatening Encounters in Space |
| SOFA | Standards Of Fundamental Astronomy |
| STK/CAT | Satellite Tool Kit/Conjunction Analysis Tool |
| SYLDA | SYstème de Lancement Double Ariane |
| TAI | Temps Atomique International (International Atomic Time) |
| TCA | Time of Closest Approach |
| TEME | True Equator Mean Equinox |
| TLE | Two Line Element |
| TOD | True (Equator) Of Date |
| TT | Terrestrial Time |
| UPM | Universidad Politécnica de Madrid |
| US | United States (of America) |
| SSN | Space Surveillance Network |
| UTC | Coordinated Universal Time |
| VOP | Variation Of Parameters |
| WDC-A-R&S | World Data Center-A for Rockets and Satellites |

1 The Space Debris problem

After 60 years of space travel history a new threat for space missions has become of capital importance. Since many years, Low Earth Orbit (LEO) spacecraft are facing a problem which has arisen in the already challenging mission of orbiting the Earth. The ever growing population of space debris (or space junk), especially in the LEO zone, is posing serious issues to the survival of man made objects in space. Every mission planner has now to take into account the possibility of the satellite to collide with relative small pieces of debris which, travelling at orbital speeds, could jeopardise the survival of the mission.

The ability to predict possible collision risks is fundamental. A lot of effort is being made among the scientific community in the development of effective and powerful tools to compute and assess collision risks between spacecraft and space debris. These tools permit to choose the correct avoidance manoeuvres in order to prevent space collisions which mean both the loss of the mission and the formation and spreading of new dangerous space debris. For this reason, in a more general view, fast tools are needed not only to estimate the direct risk of collision but also to point the hazardous objects out of a catalogue of thousands of them.

The present work aims to create an effective analysis tool which can help in the more and more difficult task of finding spacecraft's potential threats in order to select them for further and deeper analysis. The tool achieves this objective by the monitorization and subsequent analysis of Minimum Orbital Intersection Distance (MOID) over time. Moreover it can be seen as a first filtering stage of a more complex tool which could analyse thousands of space debris and determine the risk of collision with a selected spacecraft in a rapid and reliable way.

1.1 The origin of space debris

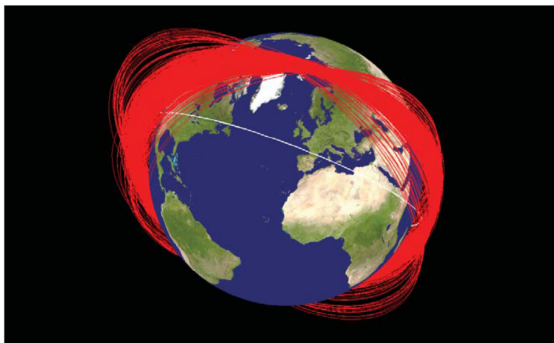
Space debris are defined as rests of old satellites, spent rocket stages as well as the fragments from their disintegrations and collisions. Amongst all the objects orbiting the Earth, space debris constitute the vast majority of them and they are present in the near Earth space at all altitudes, their distribution being denser in two principal zones: the Geosynchronous Equatorial Orbit (GEO) ring and the LEO.

As of January 2019, the European Space Agency (ESA) states that there are about 5000 satellites still in space, 1950 of them being still active. They are part of the about 22 300 debris objects regularly tracked by space surveillance networks and maintained in their catalogue. Moreover, the number of debris objects estimated by statistical models to be in orbit is: 34 000 objects bigger than 10 cm, 900 000 objects ranging from 1 cm to 10 cm and 128 million objects ranging from 1 mm to 1 cm [1]. The problem of space debris is already of capital importance for space agencies. National Aeronautics and Space Administration (NASA) has an entire office addressed to the issue of space debris, the Orbital Debris Program Office at the Johnson Space Center.

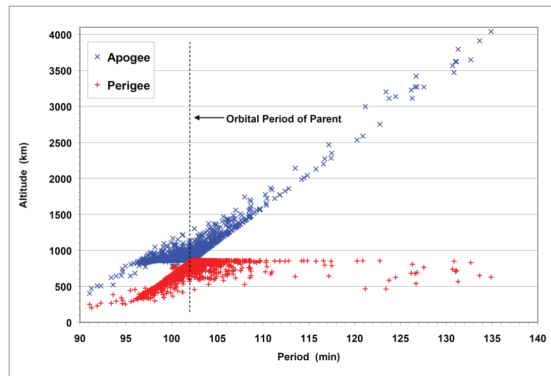
Over the years, the principal sources of space debris have been: collisions between spacecraft, jettisoned rocket stages breaks up due to the decomposition of unvented unburned fuel and missile tests to shoot down targeted satellites.

Four major powers have demonstrated in the years the capacity to shoot down satellites in orbit with anti-satellite weapons: the US, the Soviet Union, China and India. One particular case, the 2007 China's anti-satellite missile test was heavily condemned also for its consequences for the space environment. The 11th of January 2007 the Chinese anti-satellite system (ASAT) test has represented the single worst contamination of low Earth orbit during the previous 50 years. The target of the test was an old Chinese 960 kg meteorological spacecraft, Fengyun-1C, orbiting at an altitude of 845 km (apogee) by 865 km (perigee) with an inclination of 98.6°. Two

months after the test the amount of tracked space debris was around 1600 with an estimation of 35 000 debris bigger than 1 cm forming the debris cloud. The orbital planes of the debris, being subjected to the perturbations, have been dispersing from the initial disc they were confined in, scattering the debris in the entire LEO zone. Due to its altitude, the debris cloud will remain in LEO for many years to come [2].



(a) Known orbit planes of Fengyun-1C debris one month after its disintegration by a Chinese interceptor. The white orbit represents the ISS [2].



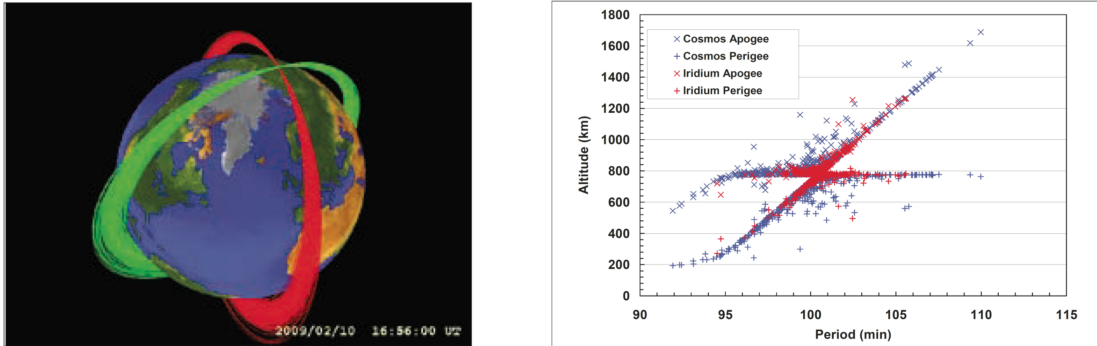
(b) By 31 March 2007 more than 1600 debris from the Chinese ASAT test had been identified and were being tracked by the U.S. Space Surveillance Network (SSN) [2].

Figure 1.1: Results of the Chinese ASAT test [2].

The space collisions are the second source of space debris. Although the probability of accidental space encounters between two spacecraft is remote, the growing population of spacecraft, especially in polar orbits, makes probabilities higher over time. On the 10th of February 2009 the first accidental hypervelocity collision occurred between two intact spacecraft. The Iridium 33 US operational communications satellite and the Cosmos 2251 Russian decommissioned communications satellite collided over extreme northern Siberia at an altitude of 790 km. Their orbits were nearly circular and inclined by 86.4° and 74.0° respectively. At the time of impact, the two orbital planes intersected at nearly right angle, thus the collision velocity resulted higher than 11 km s⁻¹. The collision generated many debris which spread at different altitudes (by the end of March that year, 823 larger debris had been classified by the US Space Surveillance Network (US SSN)) but even more debris would have been expected if the two satellites had hit body-to-body. In this case as well, due to the differential orbital periods of the debris, in the subsequent months they spread in LEO forming a shell of debris which poses future collisions hazards to other satellites in the same zone [3].

An interesting graphics showing the debris population increase up to 2019 (Fig. 1.3) highlights the dimensions of the problem. It displays a summary of all objects in Earth orbit officially cataloged by the U.S. Space Surveillance Network. *Fragmentation debris* include satellite breakup debris and anomalous event debris, while *mission-related debris* includes all objects dispensed, separated, or released as part of the planned mission [4]. It is interesting to notice how the 2007 and 2009 debris events have constituted huge instantaneous contributions to the population of *Fragmentation Debris*. Moreover, the graphics show how the population of *Rocket Bodies* and *Spacecraft* is in constant growth, with the *Spacecraft* growing at an increased rate in the last 5 years. Space access is in fact becoming easier to ever more companies, and missions including

huge constellations of satellites are already becoming reality¹.



(a) The orbital planes of Iridium 33 and Cosmos 2251 were at nearly right angles at the time of collision [3]. (b) Altitude distribution of 731 cataloged debris on 20 March 2009 [3].

Figure 1.2: Results of the Iridium-Cosmos 2251 collision of 2009 [3].

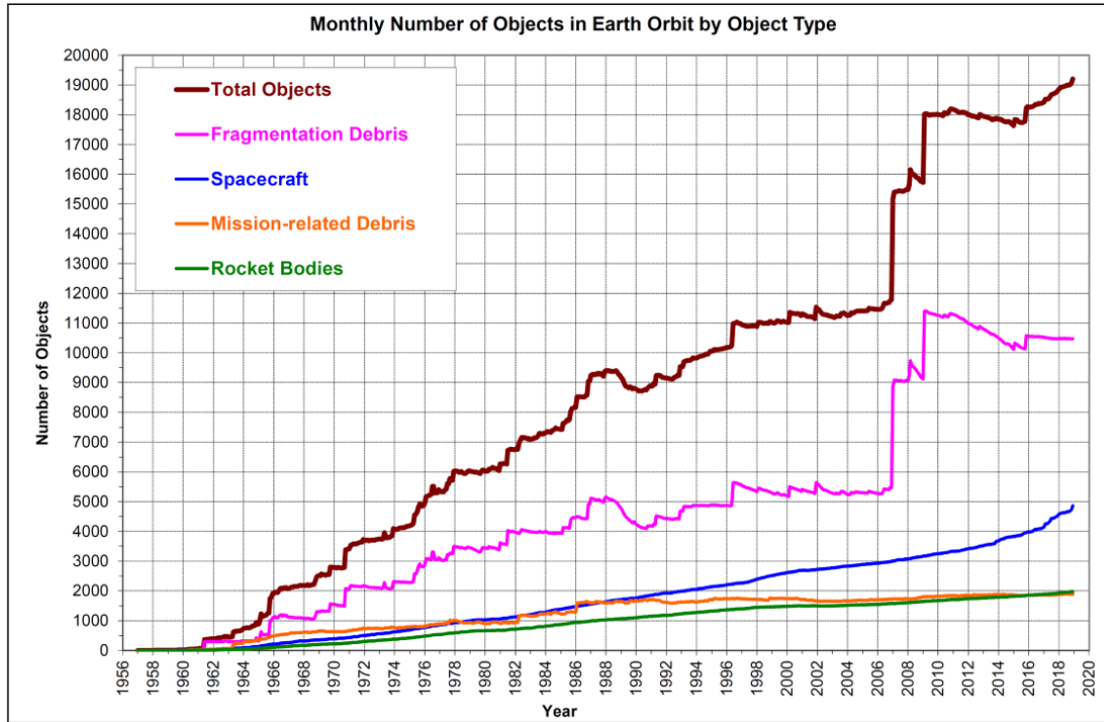


Figure 1.3: Monthly Number of Cataloged Objects in Earth Orbit by Object Type [4].

¹Space based satellite internet service able to connect all the world needs dense constellations of satellites. Projects like *OneWeb* or *Starlink* plan to develop constellations of about 650 and 12000 satellites respectively, in order to fulfill this requirement. *OneWeb* already launched its first six satellites in February 2019, while *Starlink* has launched 60 satellites on the 24th of May 2019 for test purposes.

1.2 Risks for active spacecraft

Most of the nowadays active satellites, the ISS included, orbit in LEO and space debris constitute a very important hazard to their survival. Even for very tiny particles such as paint flakes, their impact with an active satellite moving at orbital speed could signify the loss of the entire mission.

There are many examples of recorded space junk related damages to active spacecraft. The Russian (former Soviet Union's) space station MIR and the Hubble space telescope had their solar arrays damaged by micro debris impacts which resulted in performance degradation. The Space Shuttle had its radiators damaged during missions STS-115 (Sept 2006) and STS-118 (Aug 2007) due to impact events (the shuttle payload bay door radiator sandwich panel was completely perforated) [5].

One of the best well documented cases of space debris impact occurred to the ESA's Copernicus mission Sentinel-1A satellite. It suffered a sudden and permanent power reduction in a solar array on the 23rd August 2016. The anomaly was suspected to be caused by a hypervelocity impact, thus the flight control team managed to take a photo of the affected solar array and found out a very large damage area of about 40 cm in diameter (Fig. 1.4). Subsequent investigation deduced that the impactor must have had a small size, inferior to 1 cm [6].

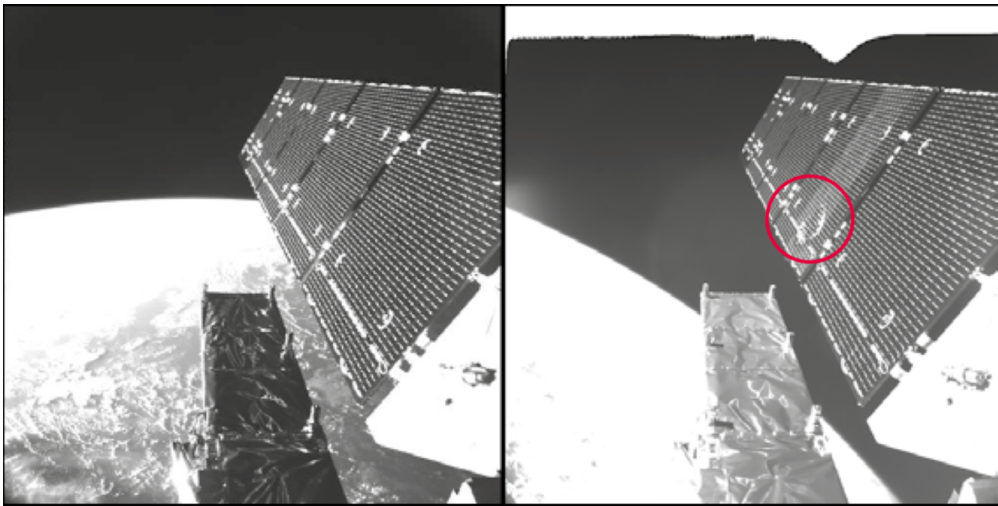


Figure 1.4: Sentinel-1A's solar array before and after the impact of a millimetre-sized particle [6].

In the case of the ISS, the risk of collision with a piece of space junk poses serious problems to the crew survival. For this reason, US SSN personnel perform conjunction assessments thrice daily to identify any object which might come within a volume of 2 km (local vertical) by 25 km by 25 km (local horizontal) centred around the space station during the next three days. If an object satisfies that criterion, additional tracking of the object is tasked, and higher precision conjunction assessments are undertaken. Should the subsequently calculated probability of collision exceed a value of 0.0001 (1 in 10000), then a collision avoidance manoeuvre or Debris Avoidance Manoeuvre (DAM) is normally executed. In the case of rapidly changing orbit objects, a delayed recognition of a threat could leave no time to prepare for a DAM. In such cases, the ISS crew moves to their return vehicles and prepare to undock quickly in the unlikely event that the object does impact the ISS [3].

1.3 A current method for threatening space encounters assessment

The concern over the space debris problem is growing day by day as new missions put more objects in space at an increased rate. There is a particular service which ensures reliable data to the satellite operator community in order to inform on pending conjunctions on orbit in a determined period of time.

The Center for Space Standards & Innovation (CSSI) offers the Satellite Orbital Conjunction Reports Assessing Threatening Encounters in Space (SOCRATES) service [7], intended to help satellite operators avoid undesired close approaches through advanced mission planning. CSSI runs a list of all satellite payloads on orbit against a list of all objects on orbit using the catalogue of all unclassified North American Aerospace Defense Command (NORAD) Two Line Element (TLEs) data sets to look for satellite conjunctions for the coming week. The runs are made using Satellite Tool Kit/Conjunction Analysis Tool (STK/CAT) software and the NORAD SGP4 propagator implemented in STK.

As said at the beginning of this chapter, more than 1950 active satellites are currently in space, some collisions have already taken place and the risk of colliding with space debris is not null. Moreover, the frequency of the near misses occurring every day is even higher: for example, conjunctions within 1 km occur each week. This is a real threat to space missions and for this reason, the SOCRATES service has been developed.

SOCRATES

In order to be reliable, SOCRATES uses the most comprehensive orbital database currently available, the NORAD two-line element sets. These data are updated twice each day and made available electronically via the Space Track web site. That database is not fully comprehensive, however, because it intentionally omits those satellites deemed vital to US national security².

SOCRATES, compares a high number of satellites' payloads against the rest of catalogued objects over an one-week period time. To speed up the computation and obtain a systematic way of searching the conjunctions, an efficient search strategy is pursued. STK/CAT implements a number of standard pre-filters (out-of-date TLE, apogee/perigee, orbit path and time) to reduce the overall computational complexity of this task.

STK/CAT not only calculates the minimum distance and the time of closest approach (TCA) for all conjunctions, it also provides calculations of the true probability and the maximum probability of collision.

Each day the SpaceTrak web site releases a new TLEs database. SOCRATES run begins by dividing the data in two sets, payloads and all objects. Searches are currently limited to conjunctions involving payloads to give satellite operators an opportunity to plan to move satellites out of the hazardous zone, in the case of being manoeuvrable. STK/CAT looks for all conjunctions which are within 1 km at the time of closest approach and reports minimum distance and the maximum probability for each conjunction.

Each SOCRATES' upload includes Top 10 lists sorted by maximum probability and minimum distance at TCA, together with a set of predicted conjunctions matching the input criteria. Each report shows basic information defining which satellites are involved in the conjunction along with the specific time and circumstances of the event.

SOCRATES has thus the ability to rapidly build a complete conjunction scenario for enhanced analysis at the push of a button. This enables the satellite users to analyse the situation and have a rapid assessment over their spacecraft's short time possible threats. In this way, they can

²NORAD maintains undisclosed about 184 payloads along with the associated rocket bodies and upper stages which delivered them to orbit, as of the 28th of March 2005 [7].

plan mitigation actions and avoidance manoeuvres in order to minimize their payloads collision risk.

1.4 Aim of this work

The objective of this work is the development of a MOID analysis tool to support the search of possible close orbital encounters. This allows optimal orbital collision risk assessment for efficient mission planning.

The tool is based on the simple concept of the repeated MOID computation between two objects at successive instants of time. The calculation results permit to have the MOID time variation (allowing the analysis of its *time derivative*); the MOID monitorization is thus assured in a very effective way.

The MOID analysis tool is based on the integration of two specific tools designed by the Space Dynamics Group of the Technical University of Madrid (SDG-UPM). First of all, a space propagator is needed: the SDG's DROMO propagation method is used because of its robustness and speed. It takes the selected spacecraft starting positions and propagates them for a defined time interval. Secondly, SDG's MOID calculation method is selected because of its speed given by its innovative calculation concept. The MOID is computed at every instant in which the spacecraft osculating orbits are known thanks to the previous propagation. The final result is obtained through the optimal implementation of the two methods along with public available software for celestial mechanics calculations.

In order to prove the tool's effectiveness, it must be developed and tested using reliable ephemerides for the space objects of interest. For this reason, "the most comprehensive orbital database currently available, the NORAD two-line element set" [7] is considered. To test the tool and to see an immediate application, the most valuable and vulnerable spacecraft is selected: the International Space Station (ISS). The ISS is obviously present in the TLE database as well, along with thousands of satellites (active or not) and space debris. It is selected as the main target against which the other object's orbits will be compared.

The time evolution of the MOID between two satellites (or, in particular, between a satellite and a space debris) can be a very powerful and interesting tool for understanding how two objects will behave one respect to another in the future. It can be used as a filtering stage to individuate possible threatening objects³. Finally, this method can result in an useful discriminant in the very important task of preventing future close approaches in LEO.

The present document follows the same order of the tool's data processing. Chapter 2 presents the data source: the Two Line Element set and all the necessary theory for TLEs interpretation and processing. It is important to have reliable and consistent data for the successive propagation. Chapter 3 illustrates the main perturbation contributions to the orbital movement and the propagation based on the DROMO theory. Chapter 4 is entirely dedicated to the SDG-UPM's MOID computation method, to highlight its advantages. Chapter 5 shows the results of both the methods implementation, focusing on the short period and long period analysis. Moreover, it presents an example of the tool application. Chapter 6 ends the dissertation gathering the conclusions drawn from the analysis.

³It is in fact, an enhanced version of the second filtering stage of the three filtering stage concept proposed by Hoots, Crawford and Roehrich [8]. The idea of Hoots addresses the problem of the determination of future close approaches between satellites. From this point of view, the present work could improve the second stage effectiveness and span.

2 Source of the data

The source of the objects' ephemerides which will be analysed and whose orbits will be predicted in the present work must contain the principal satellites and space debris orbiting the Low Earth Orbit and which are potentially hazardous for the survival of the active and in some cases manned LEO spacecraft. The most common database utilised in the industry and in the astronomic field for space objects ephemerides is the TLE data set held by the NORAD [9]. NORAD maintains general perturbation element sets on all resident (LEO) space objects. The observations are made several times a day by the Joint Operations Center (JSPOC) operated by the US Air Force Space Command (AFSPC). Once the observations pass through an initial association and verification stage, they are passed to the Orbit Determination operation [10]. Finally, these element sets are provided to users through the AFSPC website (<https://www.space-track.org>) and additionally the CelesTrak website (<https://celestrak.com>) in the form of text files. Actually the TLE data constitutes the only *public* data source covering the majority of orbiting objects [11].

2.1 The Two Line Element Set

The Two Line Element set was initially intended for *punch cards*, hence the simple format of a two lines of text for every object. Nowadays, the format was replaced by text files which contain a large amount of objects, written one after another with the original TLE format, eventually including a title line preceding the element data. This first line contains the name of the object in a more readable format. Thus, a NORAD two-line element set consists of two 69-character lines of data which can be used together with NORAD's SGP4/SDP4 orbital model to determine the position and velocity of the associated satellite. The only valid characters in a two-line element set are the numbers 0-9, the capital letters A-Z, the period, the space, and the plus and minus signs; no other characters are valid [12]. The NORAD element sets are *mean* values obtained by removing periodic variations in a particular way. In order to obtain good predictions, these periodic variations must be reconstructed (by the prediction model) in exactly the same way they were removed by NORAD [9]. This topic will be addressed later on. The TLEs' format used for this work is constituted by three lines describing each satellite or space debris, presented as follows:

```
AAAAAAAAAAAAAAAAAAAAAAAAAAAA
1 NNNNNU NNNNNAAA NNNNN.NNNNNNNN +.NNNNNNNN +NNNNN-N +NNNNN-N N NNNNN
2 NNNNN NNN.NNNN NNN.NNNN NNNNNNNN NNN.NNNN NNN.NNNN NN.NNNNNNNNNNNNNN
```

Line 0 is a twenty-four character name, whereas lines 1 and 2 are the standard Two-Line Orbital Element Set Format identical to that used by NORAD and NASA. Table 2 summarizes the meaning of every character of the two lines [12].

The line number occupies the first column of it and it can be 1 or 2. Analysing the two rows, the second number which appears in them is the NORAD's Catalog Number which must be the same for the two rows otherwise the TLE is not valid. The NORAD Satellite Catalog (SATCAT) contains 44336 objects as of June, the 20th, 2019. The minimum size of objects that are maintained in the catalogue is 10cm. A diameter of 10cm is in fact the typical minimum size that current sensors from the JSPOC can track.

Continuing in the first row, the third field represents the security classification of the data, for example all the TLEs which will be analysed in this work are unclassified objects, hence the omnipresent "U" letter (the secret data have the "S" letter, thus not being publicly available).

The following three fields represent the International Designator of the object assigned by

the *World Data Center-A for Rockets and Satellites* (WDC-A-R&S) which collaborates with NORAD and NASA in maintaining the registry. These fields represent the last two digits of the launch year, the number of the launch in that year and the piece of that launch for each object. It is important to observe the cause of the difference between the International Designator and the NORAD's Catalog Number: while the first is a record of the launch itself, the latter is assigned based on the NORAD's first observation of the space object.

Fields 1.7 and 1.8 of the first line (according to the aforementioned Table 2) define the reference time of the TLE, or the *epoch* of the TLE. The interpretation of these two fields is of extreme importance for the correct use of the data and thus for the calculations. Field 1.7 represents the last two digits of the year, the numbers 57 to 99 corresponding to years 1957 to 1999 (no space activity existing prior to the year 1957) and digits 00 to 56 corresponding to years 2000 to 2056. Field 8 represents the number of the day in that year, the days starting at 1 for the 1th of January. The decimal part of the day indicates the fraction of the day, being midnight the starting point (.000) and remembering that the time is based on the Coordinated Universal Time (UTC). In order to be more clear, an example is set: the number 19001.00000000 corresponds to midnight January the 1th, 2019, UTC.

Fields 1.9 and 1.10 represent the first derivative of the mean motion divided by two and the second derivative of the mean motion divided by six respectively. Unfortunately these quantities are not used by the SGP4/SDP4 propagators and therefore are not of utility for this application.

Field 1.11 is a SGP4-type drag coefficient (it means, adapted to the SGP4 atmospheric model), it is called B^* *BSTAR* and it is an adjusted value for the ballistic coefficient B . Field 1.12 represents the ephemeris type, it is, the orbital model used to generate the data. Since all distributed element sets are created with the SGP4/SDP4 models, it is not considered in this study. The last column of each line (1.14 and 2.10) is a modulo-10 checksum on the respective line data.

Going forward with the second line, the orbital elements are presented. As said, they are mean elements calculated through the application of the SGP4/SDP4 orbital models. They are, in order, the inclination i , the Right Ascension of the Ascending Node (RAAN) Ω , the eccentricity e , the argument of the perigee ω , the mean anomaly M which is used instead of the true anomaly θ and the mean motion n which is used instead of the semi-major axis a . All the angular quantities are expressed in degrees and they range between 0° and 360° , apart from the inclination which ranges between 0° and 180° ; the mean motion is expressed in revolutions per day.

Finally, at the end of the second line, field 2.9 expresses the revolution number at epoch, which is calculated by the NORAD starting from the ascending node pass. In this convention, the 0th revolution occurs between the launch and the time the first ascending node is reached.

As an example, the ISS TLE is presented, all its fields being highlighted and described in Fig. 2.1.

| Card # | | Object Name | | | | | | | | | | | | Chk Sum | |
|------------------|-------------------|--|-----------------|--------------------------------------|--|---|-------------------------|----|-----------|--|--|--|--|---------|--|
| Card # | | I S S (Z A R Y A) | | | | | | | | | | | | Chk Sum | |
| Satellite Number | Class | International Catalog Designator Year Launch# Piece | Year | Epoch Day of Year (plus fraction) | Mean motion derivative [rev/day/2] S | Mean motion second derivative [rev/day/2] S | Bstar [ER] S S E | PF | Elem num | | | | | | |
| Satellite Number | Inclination [deg] | Right Ascension of the Node [deg] | Eccentricity | Arg of Perigee [deg] | Mean anomaly [deg] | Mean Motion [rev/day] | Epoch Rev | | | | | | | | |
| 0 | | | | | | | | | | | | | | | |
| 1 | 2 5 5 4 4 U | 9 8 0 6 7 A | 1 8 | 2 8 3 . 2 1 5 9 0 3 1 8 | . 0 0 0 0 1 8 2 4 | 0 0 0 0 0 - 0 | 3 5 1 8 3 - 4 | 0 | 9 9 9 | | | | | | |
| 2 | 2 5 5 4 4 | 5 1 . 6 4 1 9 | 1 6 5 . 4 8 9 2 | 0 0 0 3 5 3 3 | 2 6 4 . 2 4 9 1 | 2 4 2 . 0 2 3 8 | 1 5 . 5 3 7 9 8 4 0 0 | 0 | 1 3 6 4 0 | | | | | | |

Figure 2.1: ISS TLE structure.

Moreover, to make the structure more clear, an example of file containing the TLEs is shown below. Fig. 2.2 shows a typical TLE text file including some of the most known spacecraft and debris.

```

ISS (ZARYA)
1 25544U 98067A 19135.21279275 .00001725 00000-0 34935-4 0 9997
2 25544 51.6417 165.0380 0001332 355.9579 121.1393 15.52672701170139
TIANGONG-2
1 41765U 16057A 19135.12342266 .00005316 00000-0 64693-4 0 9994
2 41765 42.7822 164.0906 0007095 25.7931 73.8654 15.61511325151879
FENGYUN 1C DEB
1 29733U 99025X 19134.36466503 .00000284 00000-0 56646-3 0 9994
2 29733 99.2133 175.7138 0579360 321.3193 97.9174 12.91656368580442
IRIDIUM 33 DEB
1 33772U 97051K 19135.03027199 .00015288 00000-0 15590-2 0 9990
2 33772 86.3996 327.3183 0023881 165.0129 309.8406 14.90360134542662
COSMOS 2251 DEB
1 33757U 93036E 19134.40887939 -.00000005 00000-0 78142-5 0 9995
2 33757 74.0387 29.9571 0016015 270.2523 209.7123 14.32014817535753
METEOSAT-8 (MSG-1)
1 27509U 02040B 19134.86239095 .00000126 00000-0 00000-0 0 9998
2 27509 6.0349 55.7102 0002391 353.1345 175.2498 1.00271669 61270
BREEZE-M DEB
1 38884U 12044R 19134.49161034 .00006490 25972-5 19935-3 0 9997
2 38884 50.0025 156.2949 2305891 170.8957 194.2472 10.82027329253436
ORBCOMM-X [-]
1 21576U 91050C 19135.16595285 .00000035 00000-0 24756-4 0 9992
2 21576 98.6358 182.4410 0004453 47.6357 312.5208 14.41556324461670
E-ST@R-II
1 41459U 16025D 19135.17504412 .00003819 00000-0 19686-3 0 9994
2 41459 98.1009 219.9524 0169585 114.4572 247.4475 15.05366801167352
SENTINEL-1A
1 39634U 14016A 19135.15027484 .00000201 00000-0 52251-4 0 9999
2 39634 98.1824 142.8292 0001418 89.8600 270.2761 14.59198124272338
AEOLUS
1 43600U 18066A 19134.47634617 -.00000138 00000-0 00000+0 0 9992
2 43600 96.7209 141.8252 0007029 131.8516 228.6292 15.86835340 41946

```

Figure 2.2: Example of a text file containing TLEs.

Table 2: TLE characters meaning.

| Line 1 | | |
|--------|--------|---|
| Field | Column | Description |
| 1.1 | 01 | Line Number of Element Data |
| 1.2 | 03-07 | Satellite Number |
| 1.3 | 08 | Classification (U=Unclassified) |
| 1.4 | 10-11 | International Designator (Last two digits of launch year) |
| 1.5 | 12-14 | International Designator (Launch number of the year) |
| 1.6 | 15-17 | International Designator (Piece of the launch) |
| 1.7 | 19-20 | Epoch Year (Last two digits of year) |
| 1.8 | 21-32 | Epoch (Day of the year and fractional portion of the day) |
| 1.9 | 34-43 | First Time Derivative of the Mean Motion [rev/day ²] |
| 1.10 | 45-52 | Second Time Derivative of Mean Motion (decimal point assumed) [rev/day ³] |
| 1.11 | 54-61 | BSTAR drag term (decimal point assumed) |
| 1.12 | 63 | Ephemeris type |
| 1.13 | 65-68 | Element number |
| 1.14 | 69 | Checksum (Modulo 10) |
| Line 2 | | |
| Field | Column | Description |
| 2.1 | 01 | Line Number of Element Data |
| 2.2 | 03-07 | Satellite Number |
| 2.3 | 09-16 | Inclination [Degrees] |
| 2.4 | 18-25 | Right Ascension of the Ascending Node [Degrees] |
| 2.5 | 27-33 | Eccentricity (decimal point assumed) |
| 2.6 | 35-42 | Argument of Perigee [Degrees] |
| 2.7 | 44-51 | Mean Anomaly [Degrees] |
| 2.8 | 53-63 | Mean Motion [Revs per day] |
| 2.9 | 64-68 | Revolution number at epoch [Revs] |
| 2.10 | 69 | Checksum (Modulo 10) |

2.2 Data Processing

Once the elements are made available in the format of two lines of characters, the data must be processed in the correct way. The goal is to obtain the position and velocity vectors of the corresponding space objects, which is ultimately the information needed for their further manipulation.

As anticipated before, the NORAD generates the data which are released to the public by averaging the orbital elements and obtaining *mean* values by removing periodical variations in a particular way. In order to obtain good predictions, these periodic variations must be reconstructed (by the prediction model) in exactly the same way they are removed by the NORAD [13].

2.2.1 Propagation Models

The space objects classified by NORAD are divided into two major categories: near-Earth or deep-space objects, the first are those which period is less than 225 min whilst the second ones have a period greater than or equal to 225 min. The NORAD has developed since the 60s five different mathematical prediction models, the main differences residing on the theories utilised to define the gravitational and the atmospheric models.

These five simplified general perturbations (SGP) models are: the SGP model, the first to be introduced; the SGP4 model, used for near-Earth objects along with the SDP4 model, which is an extension of the SGP4 model for deep-space satellites and the SGP8 and the SDP8 models which are a modification of the SGP4/SDP4 ones, being based on the same theories and differing in the way the equations are integrated [13].

The mathematical model currently in use by the NORAD is the SGP4 propagation model, along with the SDP4 model in the aforementioned case of deep space objects (literature generally refers to both models with the SGP4/SDP4 model). These models are described by Hoots and Roehrich (1980) in the *SPACETRACK REPORT NO. 3* [13], presenting the FORTRAN IV subroutines for their correct implementation. At the time they wrote, NORAD intended to switch to the SGP8/SDP8 models, although this passage never occurred, as stated by Vallado [16].

2.2.2 SGP4/SDP4 Model

The SGP4 model, originally developed by Ken Cranford in 1970 was obtained considering the Brower solution for the gravitational model developed in 1959 and power density functions developed by Lane and Cranford in 1969 for the atmospheric model. On the other hand, the SDP4 was developed by Hujsak in 1979 extending the SGP4 theory by modelling the perturbations of the moon and the sun and giving a better detail of the Earth gravitation model [13].

The SGP4 code has been adapted over the years and by many authors, thus many versions of it are actually in use, each of them with slight differences. There are multiple versions of the SGP4 code even within the US Department of Defense (DoD).

Considering this last fact, as Vallado assumes in [11], the equations which represent the current mathematical theory are the ones presented by Hoots in 1980 [13] and reminded by the same author's publication of 2004 [14]. For this reason, the present study utilizes this SGP4/SDP4 in order to manage the TLEs.

Apart from the use of the TLEs in order to obtain the actual classical elements, the SGP4/SDP4 models allow to propagate every TLE forward and backwards respect to the epoch it is defined. An observation to be made is the fact that the epoch time for the TLEs is not necessarily the epoch coming from the last observation processed by the Orbit Determination of the JSPOC. The TLE is moved to the last ascending node before the release for distribution [10].

For the purposes of this study, all the considered TLEs are propagated with the SGP4/SDP4 to an epoch in the future (subsequent or simultaneous respect to the epoch of the most *recent* TLE) in order to have all the objects defined at the same instant of time, ready to be propagated with a different propagation method from the same starting point.

Implementation: Zeptomoby OrbitTools Libraries

In the present work, the TLE processing functions, as well as the NORAD SGP4/SDP4 propagators, have been programmed in C++ using the *Zeptomoby OrbitTools Libraries* already available in the world wide web [15].

2.2.3 SGP4/SDP4 Reference Frame

The results of the SGP4/SDP4 model are presented in the form of state vectors in the same time instant. Every state vector is composed by the position vector and the velocity vector defined in a given reference frame. The reference frame utilised by the AFSPC for its analytical theories is the *True Equator Mean Equinox* (TEME) frame. Its definition is based on the *uniform equinox* concept, which resides along the true equator *between* the origin of the intermediate Pseudo Earth Fixed (PEF) and True Of Date (TOD) frames [17]. Although it is not a common reference frame, it must be considered in order to transform the data to a standard reference frame, the Geocentric Celestial Reference Frame (GCRF), in order to allow the data's further manipulation.

2.3 TEME to GCRF conversion

In order to have a solid reference for astrodynamical calculations, an inertial reference frame is needed. The TEME reference frame developed by the AFSPC for the TLEs description is not a standard frame because of its very nature. The TEME reference is time related, i.e. it depends on the date on which the TLE is defined and this constitutes a limitation; every TLE in fact, will have a different reference. To refer every object to a common frame all the data obtained in the TEME frame must be transformed to a common and standard inertial reference frame which, as stated in the latest convention, is the aforementioned GCRF.

2.3.1 Precession and Nutation

The Earth linked frames, (such as TEME) are not inertial because they follow Earth's equator and ecliptic movement in the inertial space, it is, relative to the stars. The motion of a coordinate system fixed to the Earth is due to its *precession* and *nutation*.

The Earth's *precession* is composed by two terms: the *precession of the ecliptic* caused by the gravitational forces of the planets affecting Earth's orbit and the *luni-solar precession* (much more intense respect to the first component) caused by the Sun and Moon's gravitational fields acting on the Earth, which being not perfectly spherical, undergoes a small torque. The two effects are collectively called *general precession* and its effect is a smooth wobbling or precessional motion of the Earth. This motion causes the Earth's axis of rotation to trace out a quasi-circular shape forming a cone in the space whose half angle is equal to 23.5° (because of the obliquity of the elliptic being equal to 23.5°). The period needed to the axis of rotation to complete a circle is about 26 000 years.

The *nutation* of the Earth is produced by the additional torque that the Moon exerts on the Earth's equatorial bulge, because of the 5° inclination of Moon's orbital plane respect to Earth's equatorial plane. The Moon's orbital plane itself has a precession period of about 18.6 years, caused by the Sun perturbation. As a consequence, the Earth's nutation has a main period equal to 18.6 years, which is commonly called *precession of the equator*. The Earth's nutation

has more components which create secondary effects and which have many different frequencies. The overall results of the nutation are small oscillations of the Earth's rotation axis which are superimposed to the main precessional movement of the axis. The maximum amplitude of these oscillations is of about 0.0025° .

It is important to note that precession and nutation are caused by disturbances of the same nature acting upon the Earth. The nutation effect is the *periodic* component, while the precession effect is the *secular* component of the disturbances as can be seen in Fig. 2.3.

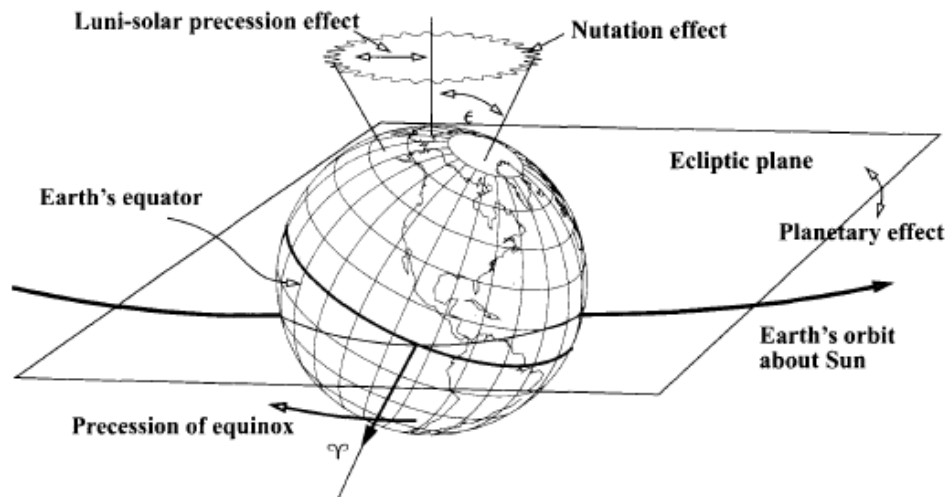


Figure 2.3: Precession and Nutation of the Earth's Equatorial Plane [17].

The general precession causes the equinox direction to move in the plane of the equator. To fix its position on a particular date it is possible to associate its orientation to an ideal inertial frame on that date: the *ecliptic of date*. The precession of the Earth's rotation axis causes the equator to wobble respect to the ecliptic. For this reason, the *mean equator of date* (MOD) is measured accounting for the nearly secular motion of the axis. The intersection of the two planes already defined in a particular date, defines the *mean equinox of date*. By including the nutation on the equator, the *true equator of date* (TOD) is obtained.

With the aim to define the standards in astronomy, the International Astronomical Union (IAU) has defined a series of conventions in order to have a common rule whenever is needed to pass between reference frames. The latest version of the standards published by the IAU are the *IAU-2000 Resolutions*. They, in particular, define the transformations between the body-fixed International Terrestrial Reference Frame (ITRF), and the GCRF [17]. This latest version of the convention is followed in this work.

2.3.2 Transformations

Considering all the terms affecting Earth's motion, now, it is important to define the transformations (which must be placed in the right order) to rotate the state vector obtained with the SGP4/SDP4 theory from the TEME to the GCRF reference frames. This is achieved through successive passages. First of all, the reference frame must be rotated from TEME to TOD using the equation of the equinoxes. Then, the TOD reference frame must be modified with the

nutaton correction in order to obtain the Mean Of Date (MOD) reference frame. Finally, the precession correction permits to pass from the MOD reference to the GCRF frame. The detailed passages will be further explained.

It is important to remember that a coordinate rotation changes only the basis of the vector, i.e. the vector after the transformation will have the same length and direction, but the three component will differ from one basis to another. Since coordinate rotations are a series of single-axis rotations, the single-axis rotations must be easily represented with some intuitive notation. In this study, the transformation matrices follow the convention utilized by Vallado in his handbook [17].

Every right-handed vector rotation is thus expressed with the following transformation:

$$\{\mathbf{x}'\} = \mathbf{R}_n(\alpha) \cdot \{\mathbf{x}\} \quad (2.1)$$

where \mathbf{x} is the initial vector, $\mathbf{R}_n(\alpha)$ the rotation matrix and \mathbf{x}' the rotated vector. The general formulas adopted for the right-handed axes rotations are defined in eq. (2.2) where the \mathbf{R} subscript indicates the principal rotation axis ($I - 1, J - 2, K - 3$).

$$\begin{aligned} \mathbf{R}_1(\alpha) &= \begin{bmatrix} 1 & 0 & 0 \\ 0 & \cos(\alpha) & \sin(\alpha) \\ 0 & -\sin(\alpha) & \cos(\alpha) \end{bmatrix} \\ \mathbf{R}_2(\alpha) &= \begin{bmatrix} \cos(\alpha) & 0 & -\sin(\alpha) \\ 0 & 1 & 0 \\ \sin(\alpha) & 0 & \cos(\alpha) \end{bmatrix} \\ \mathbf{R}_3(\alpha) &= \begin{bmatrix} \cos(\alpha) & \sin(\alpha) & 0 \\ -\sin(\alpha) & \cos(\alpha) & 0 \\ 0 & 0 & 1 \end{bmatrix} \end{aligned} \quad (2.2)$$

2.3.3 TEME to TOD transformation, Equation of the Equinoxes

Because the planes of the Earth's equator and the ecliptic are moving, the equinox which is derived from their intersection is also moving. This leads to the distinction between the *Mean sidereal time* which refers to a mean equinox that moves only with secular motion (precession) and the *apparent sidereal time* from true vernal equinox that includes all the contributions to the motion of the vernal equinox. The difference between the mean equinox (which defines the Greenwich Mean Sidereal Time: GMST) and the apparent equinox (which defines the Greenwich Apparent Sidereal Time: GAST) as measured in the plane of the true equator, is the *Equation of the Equinoxes*.

The TEME and TOD references both share the same z axis. Moreover, the TEME reference x axis is linked to the *Mean Equinox* concept while the TOD reference x axis is linked to the *True Equinox* concept. The difference between these references is represented by a rotation angle around the Earth's z axis: the *Equation of the Equinoxes* (E_{qeq}). All these concepts can be easily represented in order to give a more clear picture of the concept (Fig. 2.4).

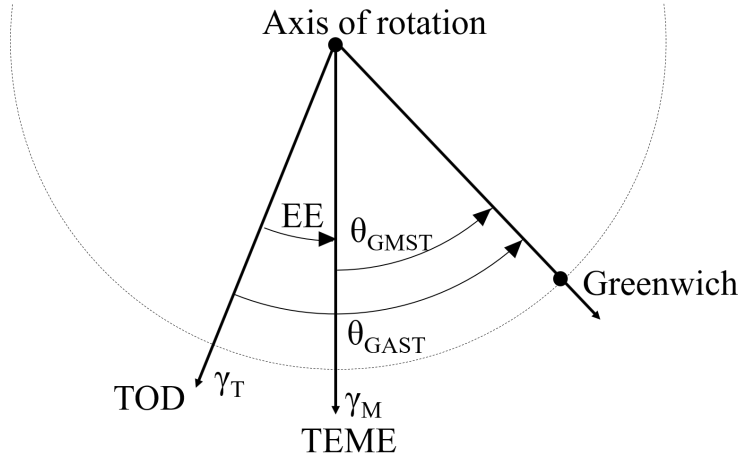


Figure 2.4: Mean Equinox and True Equinox concepts.

The mathematical relation between these reference frames is defined by the IAU-2000 Resolutions as follows:

$$\theta_{GAST2000} = \theta_{GMST2000} + Eq_{equinox2000} \quad (2.3)$$

Focusing on the Equation of the Equinoxes (which is ultimately the one needed), the same convention defines is as follows:

$$Eq_{eq} = \Delta\Psi \cos \varepsilon_A + \sum_k (C'_k \sin A_k + S'_k \cos A_k) + 0.000\,000\,87'' T_{TT} \sin \Omega_{\mathcal{C}} \quad (2.4)$$

where $\Delta\Psi$ is the total nutation in longitude, ε_A is the mean obliquity of the ecliptic, $\Omega_{\mathcal{C}}$ is the mean longitude of the ascending node of the Moon, and the coefficients C'_k and S'_k and the angular arguments A_k are used to describe the complementary terms arising from coupling between precession and nutation. The coefficients are defined by the IAU-2000 Resolutions as well. The dependence from the time is expressed through the T_{TT} term, which is the *Terrestrial Time* (TT) expressed in Julian Centuries⁴ from J2000.0⁵. In the SGP4 theory, several approximations are made in the calculation of the nutation and in the mean obliquity of the ecliptic terms, and second-order terms are neglected. The final equation to consider is thus:

$$Eq_{eq} = \Delta\Psi \cos \varepsilon_A \quad (2.5)$$

which at least maintains the Terrestrial Time (TT) dependence.

The *Terrestrial Time* needed in the equation of above, is by convention defined as the timescale of apparent geocentric ephemerides of bodies in the solar system [17], it was defined by an

⁴A Julian Century corresponds to 36 525 Julian Days. Moreover, the *Julian date*, JD, is the interval of time measured in days from the epoch January 1, 4713 B.C., 12:00. Because the values are typically large, the IAU recommends using the *Modified Julian Date*, MJD, calculated subtracting 2 400 000.5 days from the original Julian Date. This leads to lower numbers and to the simplification of days beginning at midnight instead of noon.

⁵The *epoch J2000.0* reference is a common reference in astronomy because Julian Centuries are often used as time scale. The epoch J2000.0 corresponds to January the 1st, 2000, 12:00 TT (2 451 545.5 JD = 51 545.0 MJD).

IAU resolution in 1991. It is referenced to the *International Atomic Time* TAI⁶ through the following relation:

$$TT = TAI + 32.184s + 32.184s \quad (2.6)$$

the 32.184 seconds difference being the predefined constant offset between the two systems.

The TAI must be thus related to the UTC time which is ultimately the scale of time in which the TLEs are defined. The relation between the two timescales is the following:

$$TAI = UTC + \Delta AT \quad (2.7)$$

where the ΔAT quantity is the accumulated difference between the two. It is an *Earth Orientation Parameter* (EOP) that describes the motion of the Earth and can be found in ephemeris tables.

Once the UTC time is defined in a TLE, the *Equation of the Equinoxes* consists in a straightforward substitution of terms and the relation between the two reference frames (TEME-TOD) reduces to a sidereal rotation about the Z axis of rotation of the Earth.

$$\mathbf{r}_{[TOD]} = [\mathbf{R}_3(-\mathbf{E}\mathbf{q}_{\text{eq}})] \cdot \mathbf{r}_{[TEME]} \quad (2.8)$$

The last correction that could be considered here is the polar motion correction. There is, in fact, a movement of the Earth's rotation axis respect to the crust of the Earth, which introduces more perturbations on the selected reference frames. Because the polar motion has been historically neglected for General Perturbation (GP) applications, the correction due to the polar motion is not considered in this transformations [11]

2.3.4 TOD to MOD transformation: Nutation

The nutation, as said before, is the non-secular term of the more general movement of the rotation axis of the Earth respect to a space-fixed coordinate frame. It must be considered when passing from the TOD to the MOD reference frames.

The IAU-2000A Theory of Nutation resolves the nutation into three angular components: the $\Delta\Psi$ in longitude, the $\Delta\varepsilon$ in obliquity and the mean obliquity of the ecliptic of date ε_A , as can be seen in the following representation:

⁶The International Atomic Time, (*Temps Atomique International*, *TAI*) is based on cesium-133 atomic clocks and it is needed in order to have an highly accurate system independent of the average rotation of the Earth.

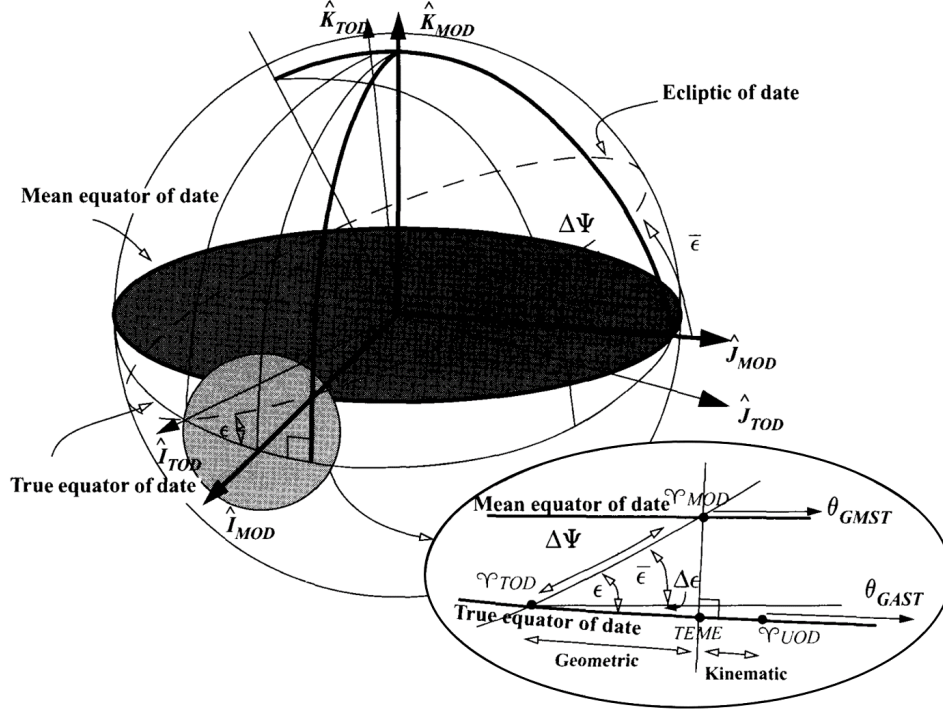


Figure 2.5: Transformation Geometry Due to Nutation [17].

The expressions for the mean and true obliquity of the ecliptic of date are:

$$\begin{aligned} \epsilon_A = & 23^\circ 26' 21.406\,00'' - 46.836\,769''T - 0.000\,183\,1''T^2 \\ & + 0.002\,003\,40''T^3 - 5.76'' \times 10^{-7} T^4 - 4.34'' \times 10^{-8} T^5 \end{aligned} \quad (2.9)$$

$$\epsilon = \epsilon_A + \Delta\epsilon \quad (2.10)$$

where the time T is, as usual, expressed in Julian Centuries since epoch J2000.0. Addressing the nutation angles $\Delta\Psi$ and $\Delta\epsilon$, their definitions are the following:

$$\Delta\Psi = \sum_{i=1}^n (S_{\Delta\Psi_i} + \dot{S}_{\Delta\Psi_i} T) \sin A_i + C_{\Delta\Psi_i} \cos A_i \quad (2.11)$$

$$\Delta\epsilon = \sum_{i=1}^n S_{\Delta\epsilon_i} \sin A_i + (C_{\Delta\epsilon_i} + \dot{C}_{\Delta\epsilon_i} T) \cos A_i \quad (2.12)$$

where the time is expressed in Julian Centuries, the terms composing the A_i coefficients are given in tables within the IAU-2000A theory and all the rest of coefficients are given in the IAU-2000A Nutation Series.

Actually, since the 1st of January 2009 the IAU released a revised version of the precession theory, the IAU-2006/2000A theory, which implies small changes in the amplitudes of the Nutation Series. Though, the use of the latest version or the theory (as has been done in this work)

requires a small correction to the nutation angles ($\Delta\Psi$ and $\Delta\varepsilon$) defined in the IAU-2000A theory as follows:

$$\Delta\Psi - \Delta\Psi_{2000A} = (0.4697'' \times 10^{-6} - 2.7774'' \times 10^{-6}T)\Delta\Psi_{2000A} \quad (2.13)$$

$$\Delta\varepsilon - \Delta\varepsilon_{2000A} = -2.7774'' \times 10^{-6}T\Delta\varepsilon_{2000A} \quad (2.14)$$

The resulting rotation matrix \mathbf{N} is a sequence of the following three rotations:

$$\begin{aligned} \mathbf{N} &= \mathbf{R}_1(-\varepsilon)\mathbf{R}_3(-\Delta\Psi)\mathbf{R}_1(+\varepsilon_A) \\ &= \begin{bmatrix} \cos \Delta\Psi & -\sin \Delta\Psi \cos \varepsilon_A & -\sin \Delta\Psi \sin \varepsilon_A \\ \sin \Delta\Psi \cos \varepsilon & \cos \Delta\Psi \cos \varepsilon \cos \varepsilon_A + \sin \varepsilon \sin \varepsilon_A & \cos \Delta\Psi \cos \varepsilon \sin \varepsilon_A - \sin \varepsilon \cos \varepsilon_A \\ \sin \Delta\Psi \sin \varepsilon & \cos \Delta\Psi \sin \varepsilon \cos \varepsilon_A - \cos \varepsilon \sin \varepsilon_A & \cos \Delta\Psi \sin \varepsilon \sin \varepsilon_A + \cos \varepsilon \cos \varepsilon_A \end{bmatrix} \end{aligned} \quad (2.15)$$

Actually, for the current application there is no need for an accuracy better than one part in 10^8 , thus, following the resolution, the nutation matrix can be simplified and it results:

$$\mathbf{N} = \begin{bmatrix} 1 & -\Delta\Psi \cos \varepsilon & -\Delta\Psi \sin \varepsilon \\ +\Delta\psi \cos \varepsilon & 1 & -\Delta\varepsilon \\ +\Delta\psi \sin \varepsilon & +\Delta\varepsilon & 1 \end{bmatrix} \quad (2.16)$$

where $\Delta\Psi$ and $\Delta\varepsilon$ are expressed in radians.

The transformation between the TOD and the MOD reference frames is thus represented by the following matrix product:

$$\mathbf{r}_{[MOD]} = [\mathbf{N}] \cdot \mathbf{r}_{[TOD]} \quad (2.17)$$

2.3.5 MOD to GCRF transformation: Precession

The precession, being the secular term in the movement of the Earth's rotation, has less strong effect respect to the nutation, nevertheless it must be considered when passing from the MOD reference frame to the GCRF reference frame.

As said before, in 2009 revision, the IAU adopted the IAU-2006/2000A precession theory which implements the P03 precession theory by Capitaine, Wallace and Chapront (2003). Their theory separates the precession of the equator, Ψ_A and ω_A (the precession in obliquity) from the precession of the ecliptic, P_A and Q_A .

The angles Ψ_A and ω_A are defined in the theory:

$$\begin{aligned} \Psi_A &= 5038.481\,507''T - 1.079\,006\,9''T^2 - 0.001\,214\,045''T^3 \\ &\quad + 0.000\,132\,851''T^4 - 9.51'' \times 10^{-8}T^5 \end{aligned} \quad (2.18)$$

$$\begin{aligned} \omega_A &= 84\,381.406\,000 - 0.027\,754''T + 0.051\,262\,3''T^2 - 0.007\,725\,03''T^3 \\ &\quad - 4.67'' \times 10^{-7}T^4 + 3.337'' \times 10^{-8}T^5 \end{aligned} \quad (2.19)$$

Whereas the quantities P_A and Q_A represents two polynomials which together give the expressions for the angles π_A , the angle between the ecliptic at a fixed epoch and the ecliptic of date,

and Π_A , the angular distance from the mean equinox, γ_0 , at the fixed epoch along the fixed ecliptic of epoch to the ascending node of the ecliptic of date (Fig. 2.6).

$$P_A = \sin \pi_A \sin \Pi_A = 4.199\,094''T + 0.193\,987\,3''T^2 - 0.000\,224\,66''T^3 - 9.12'' \times 10^{-7}T^4 + 1.20'' \times 10^{-8}T^5 \quad (2.20)$$

$$Q_A = \sin \pi_A \cos \Pi_A = -46.811\,015''T + 0.051\,028\,3''T^2 - 0.000\,524\,13''T^3 - 6.46'' \times 10^{-7}T^4 - 1.72'' \times 10^{-8}T^5 \quad (2.21)$$

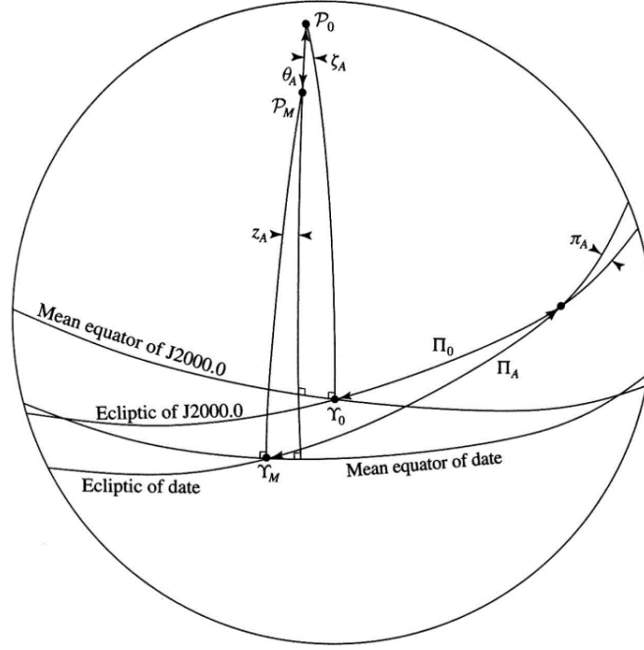


Figure 2.6: The general precession connects the mean equinox of epoch, γ_0 , to the mean equinox of date γ_M [18].

The transformation matrix needed to consider the precession is thus:

$$\mathbf{P} = \mathbf{R}_3(\chi_A)\mathbf{R}_1(-\omega_A)\mathbf{R}_3(-\Psi_A)\mathbf{R}_1(\varepsilon_0) \quad (2.22)$$

where ε_0 is the obliquity at epoch J2000.0 ($\varepsilon_0 = 23^\circ 26' 21.40600''$) and χ_A is the spherical angle from the ecliptic pole of epoch to the ecliptic pole of date with its apex at the mean equatorial pole of date. A representation of this last angle along with the rest of the angles considered in this theory can be seen in Fig. 2.7. The angle χ_A is derived from the already known parameters of precession using the following relations:

$$\begin{aligned} \cos \varepsilon_A &= \cos \pi_A \cos \omega_A - \sin \pi_A \sin \omega_A \cos(\Pi_A + \Psi_A) \\ \sin \chi_A &= \frac{\sin \pi_A}{\sin \varepsilon_A} \sin(\Pi_A + \Psi_A) \end{aligned} \quad (2.23)$$

Equation of the Equinoxes and the Precession and Nutation matrices have been implemented in the program through the *Standards Of Fundamental Astronomy* (SOFA) C++ routines by the IAU, available in the world wide web [19]. Actually, the Precession and Nutation matrices have been obtained through a single function which provides the *Precession-Nutation Matrix* according to the IAU-2006/2000A Resolution.

3 Propagation based on DROMO

After the data have been collected and propagated with the SGP4/SPD4 propagator up to a common instant of time and after the transformation of the state vectors has been carried out, the propagation of the objects is needed in order to make possible the analysis of their behaviour during the selected interval of time.

Because of the ever increasing quantity of space debris in LEO, a large amount of elements must be considered when assessing the risk of collision between the ISS and them. Their orbits, along with the orbit of the ISS, must be necessarily propagated ensuring the least possible computational time. For this reason, a routine which gets the initial condition of all the objects and propagates them in a rapid and precise way is needed. The DROMO propagator, developed by the Space Dynamics Group of the UPM has been selected. Actually, to accelerate the propagation, only the J_2 gravitational perturbation will be considered.

In this section, an analysis of the possible orbit perturbations will be carried out, along with the exposition of the reasons why only one term of the geopotential expansion is considered for the orbit propagation. After this first introduction, the DROMO propagator will be analysed, explaining its fundamentals and applying the J_2 simplification in order to fit the tool to the problem of the rapid propagation of thousands of objects.

3.1 Space perturbations

When considering the problem of orbit propagation there are many perturbations which should be considered. The orbit of a spacecraft is primarily defined by its Keplerian motion about a primary body. Perturbations intervene to modify this simple motion and all of them should accurately be modelled in order to have a very reliable propagator. In this section, some of the most important perturbations are described. Once understood, a justification can be given for including only those that contribute the most in a rapid propagator like the selected one.

The principal perturbation components for a LEO spacecraft are presented:

- *Earth's oblateness* which will be deeply analysed in the following section, causes the gravitational field not to be like the one generated by a point mass.
- *Atmospheric drag* most strongly influences the motion of a satellite *near Earth*; in fact, during the last few revolutions of the satellite's life, drag effects can be more dominant than those from the Earth's oblateness.
- *Third Body* perturbations account for Moon's and Sun's gravitational fields contributions acting upon the satellite. Third bodies have a greater effect on satellites in higher altitude orbits. Their effects become noticeable when the effects of drag begin to diminish.
- *Solar radiation pressure* which is the effect of the *solar wind* impacting upon the surface of the spacecraft or whatever object in the Sun's line of sight. It gives a *pressure* component pulling away the object from the Sun.

Ideally, to have a fine propagation all the perturbation terms shall be considered. For the aim of this work, only the Earth's oblateness will be considered, being in this case the most important perturbation term compared with all the other possible terms.

3.2 The Earth Gravitational Field

Since this work applies to Earth orbits and in particular to LEO, the motion of the considered objects will be mainly governed by the Earth. This leads to neglect the third body perturbations generated by the Moon and the Sun. The principal force acting upon a spacecraft is due to the gravitational field of the Earth. In a very rough approach, the Earth gravitational field can be considered as the field generated by a point mass at the centre of the mass distribution. In this case, the study reduces to the analysis of the *two body problem* for which the solution is analytical and already known; it corresponds to the Keplerian motion of the spacecraft around its central body. Unfortunately, to study the forces acting upon an object in LEO, a more accurate model of the gravitational field must be considered. The Earth gravitational field is not that of a point mass. Because of its rotation the Earth bulges at the equator. Also, the continental blocks, ocean basins, mountain ranges, etc., produce local deviations from a spherical Newtonian point mass field. All these effects must be considered through a gravitational field mathematical.

Gravity is a conservative force, it can thus be described in terms of a potential. For any distribution of mass, the acceleration of a test particle can be expressed as:

$$a = -\nabla V(x, y, z) \quad (3.1)$$

Where V represents the specific potential and must be modelled in order to obtain the correct components of the force acting upon every position in space. The manipulation of the Earth gravitational potential to take into account the perturbation forces caused by its real shape leads to the mathematical modelling of the Earth's shape using spherical harmonics. The resulting potential function here expressed in spherical coordinates (radius r , colatitude θ and longitude ϕ) is thus:

$$V(r, \theta, \phi) = -\frac{\mu_{\oplus}}{r} \sum_{n=0}^{\infty} \sum_{m=0}^n \left(\frac{R_{\oplus}}{r}\right)^n P_n^m(\cos \theta) \cdot (C_{nm} \cos m\phi + S_{nm} \sin m\phi) \quad (3.2)$$

Where μ_{\oplus} is Earth's gravitational constant, $P_n^m(\cos \theta)$ are the *associated Legendre polynomials*, n and m indices are respectively the *degree* and the *order* of the geopotential expansion, while the constants C_{nm} and S_{nm} are defined so that the potential fits to the Earth real gravity field. The Newtonian point mass potential appears as the first term ($n = 0, m = 0$) in the geopotential expansion. Since $m = 0$, $\cos m\phi = 1$, $\sin m\phi = 0$, and since the first Legendre polynomial $P_0^0 = 1$, the first term does not depend on either the longitude nor the colatitude.

The Spherical Harmonics

The terms for order $m = 0$ are called *zonal harmonics*, where the dependence of the potential on longitude vanishes and the field is symmetrical about the polar axis. Some authors use a " J " to identify these terms; in this case they are defined as the opposite of the " C " zonal harmonics.

$$-C_{n0} = J_n \quad (3.3)$$

The first zonal harmonic, for $n = 1$ and $m = 0$ shifts the center of mass of the entire Earth north of south along the z axis. Choosing as origin the centre of mass of the Earth thus makes $J_1 = 0$ and the first zonal harmonic vanishes. The first non-vanishing zonal harmonic is thus the $n = 2$ term.

$$V_{20} = \frac{\mu_{\oplus} R_{\oplus}^2 J_2}{2r^3} (3 \cos^2 \theta - 1) \quad (3.4)$$

For the Earth, the coefficient $J_2 = -C_{20} = 0.001082$, which is about 10^{-3} of the contribution of the Newtonian point mass term. Physically, this coefficient represents the Earth's oblateness.

This is the dominant term in the Earth’s potential expansion after the Newtonian term, and for all other planets as well. J_2 is almost 1000 times larger than the next largest coefficient (J_3).

Sectoral harmonics occur when $n = m$ and they are functions of longitude only, so they represent bands of longitude. They divide the sphere into $2n$ “orange-slice” sectors. The $n = m = 1$ sectoral harmonic moves the Earth’s center of mass off the origin of the coordinate system to some other point within the equatorial plane. Again, the most suitable choice is to set $C_{11} = S_{11} = 0$, leading to the first not null sectoral harmonic being the $n = m = 2$ term which is in fact the largest sectoral term. It is noticeable that the C_{22} and S_{22} coefficients are about 10^{-6} , it is, three orders of magnitude smaller than J_2 .

The general case when $m \neq 0$ and $n \neq m$, is called a *tesseral harmonic*. It combines the latitude dependent banding of the zonal harmonics with the longitude related sectoral harmonics to produce a checkerboard of low and high potential regions of the sphere. These *tiles* can finally describe all the different facets of the Earth’s shape.

To better understand the geometric distribution of the different harmonics, they are graphically represented in Fig. 3.1.

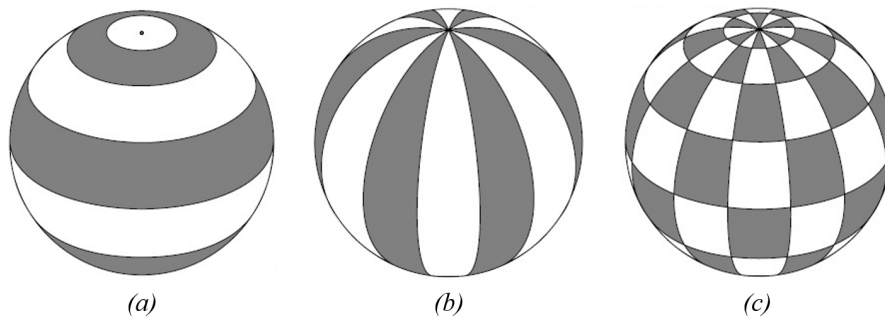


Figure 3.1: The kinds of spherical harmonics: (a) zonal, (b) sectoral, (c) tesseral.

Table 3: Selected EGM-96 coefficients.

| Zonal harmonics | | Sectoral and Tesseral harmonics | | |
|-----------------|---------------------------------------|---------------------------------|--|---------------------------------------|
| n | J_n | n, m | C_{nm} | S_{nm} |
| 2 | $1.082\,626\,683\,55 \times 10^{-3}$ | 2 1 | $-2.414\,000\,000\,00 \times 10^{-10}$ | $1.543\,100\,000\,00 \times 10^{-9}$ |
| 3 | $-2.532\,656\,485\,33 \times 10^{-6}$ | 2 2 | $1.574\,460\,374\,56 \times 10^{-6}$ | $-9.038\,038\,066\,39 \times 10^{-7}$ |
| 4 | $-1.619\,621\,591\,37 \times 10^{-6}$ | 3 1 | $2.192\,638\,529\,17 \times 10^{-6}$ | $2.684\,248\,902\,97 \times 10^{-7}$ |
| 5 | $-2.272\,960\,828\,69 \times 10^{-7}$ | 3 2 | $3.089\,892\,068\,81 \times 10^{-7}$ | $-2.114\,376\,124\,37 \times 10^{-7}$ |
| 6 | $5.406\,812\,391\,07 \times 10^{-7}$ | 3 3 | $1.005\,487\,780\,64 \times 10^{-7}$ | $1.972\,225\,590\,06 \times 10^{-7}$ |
| 7 | $-3.523\,599\,084\,18 \times 10^{-7}$ | 4 1 | $-5.087\,993\,604\,04 \times 10^{-7}$ | $-4.491\,448\,728\,39 \times 10^{-7}$ |
| 8 | $-2.047\,994\,669\,85 \times 10^{-7}$ | 4 2 | $7.841\,758\,598\,44 \times 10^{-8}$ | $1.481\,778\,682\,96 \times 10^{-7}$ |
| 9 | $-1.206\,169\,673\,65 \times 10^{-7}$ | 4 3 | $5.920\,994\,026\,29 \times 10^{-8}$ | $-1.200\,776\,676\,34 \times 10^{-8}$ |

The EGM-96 Gravity model

A table of the C_{nm} and S_{nm} coefficients is called a *gravity model* and several are available. For the purpose of this work, the Earth Gravity Model EGM-96 was selected and in Table 3 the

first and most important terms are presented. As can be seen from the table the higher order terms fall off as r^{-n-1} in the potential, which means that the force terms they generate fall off as r^{-n-2} . High order terms are thus only significant in the immediate vicinity of the planet. The geopotential expansion in fact, reverts to its first terms as the distance from the planet increases. At long distances from the Earth, the field is that generated by a Newtonian point mass.

The Main Problem

The selection of the geopotential model precision depends on the precision needed for a particular application and thus, a higher or lower number of spherical harmonics could be used. It can be seen that the largest coefficient is J_2 , which is of the order of 10^{-3} of the point mass term. The next coefficient is itself of the order of 10^{-3} respect to J_2 ; which leads to an order of 10^{-6} respect to the unity. In most of the applications, an expansion to the J_2 term is sufficient for the purposes of the analysis, especially when high rapidity combined with acceptable accuracy are needed. The J_2 term is in fact so important that the problem of solving for the J_2 perturbation effects has gained the name of “the main problem of artificial satellite theory” [21]. In the present work, the *main problem* will be considered and the propagation of all the objects in LEO will be held using a tool optimized for the *main problem*.

3.3 DROMO propagator

The DROMO propagator developed by the UPM Space Dynamics Group is, as described by the authors “a regular, robust and efficient propagator” [22]. It means that DROMO combines numerical stability, accurate results at low computational cost and absence of singularities for Keplerian orbits. For these reasons, it was selected as a starting point for the propagation of LEO objects. DROMO propagator is a *special perturbation method*⁷ of variation of parameters (VOP) based in a set of redundant variables including quaternions.

The peculiarity of this new method is that the description of motion is broken into three steps [22]: (1) movement of a reference frame attached to the orbital plane; (2) osculating trajectory in the orbital plane; (3) pin-point the position in the osculating trajectory as a function of time. This vision permits to separate the movement in the orbital plane and the movement of the orbital plane itself. The introduced *modularity* of the movements leads to computational speeding.

The core of the propagator is a set of eight Ordinary Differential Equations (ODE) and the independent variable is a fictitious time which reduces to the true anomaly when the motion is purely Keplerian. The DROMO set of dependent variables is redundant and seven dependent variables are *generalized elements*, that is, they take constant values in the Keplerian motion.

3.3.1 Geometric and kinematic aspects of DROMO

Propagating an orbit consists in the numerical integration of the set ODEs of the motion with the initial conditions. In the simpler case of a particle M of mass m moving in a fixed inertial frame $Ox_1y_1z_1$ (rigid body 1, in this case the Earth, whose center of mass O is the origin of the frame), the forces acting upon it are: the Earth gravitational field as seen in section 3.2, and all the forces included in the perturbing force \mathbf{F}_p . Under these conditions, the motion equation

⁷A *special perturbation method* is a method which numerically integrates the equations of motion including all necessary perturbing accelerations.

which represents the movement of M is the following:

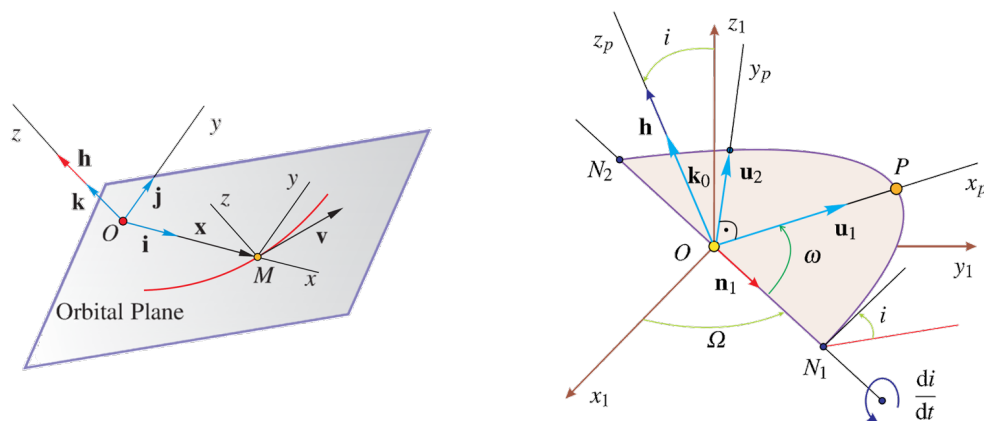
$$m \frac{d^2 \mathbf{x}}{dt^2} = -\frac{m\mu}{|\mathbf{x}|^3} \mathbf{x} + \mathbf{F}_p \quad (3.5)$$

which should be integrated from the appropriate initial conditions:

$$\text{for } t = t_0 : \quad \mathbf{x} = \mathbf{x}_0, \quad \mathbf{v} = \mathbf{v}_0 \quad (3.6)$$

In DROMO, this problem is addressed through a transformation which implies a preliminary geometric definition of the problem.

The orbital frame $Mxyz$ is defined considering the relative position of the particle M respect to the mass center of the central body (i.e. the Earth). As can be seen in Fig. 3.2a, it is defined with Mx axis along the radius vector \mathbf{x} of M , the plane Mxy generated by the vectors \mathbf{x} and \mathbf{v} , so that $\mathbf{v} \cdot \mathbf{j} \geq 0$, and the axis Mz completing a right-handed orthogonal frame. The plane Mxy is the *orbital plane*. In the pure Keplerian motion ($\mathbf{F}_p = \mathbf{0}$), it is fixed to the inertial frame $Ox_1y_1z_1$ and it contains the trajectory of M . In the perturbed motion ($\mathbf{F}_p \neq \mathbf{0}$) the orbital plane is moving in the inertial space and contains the osculating orbit.



(a) Orbital frame

(b) Perifocal frame

Figure 3.2: Reference frames definition [22].

Once the *orbital plane* is defined, it is oriented in the inertial space. In the pure Keplerian motion the orbital plane is located by three Euler angles that take constant values: the longitude of the ascending node Ω , the inclination i and the argument of the pericenter ω . In the perturbed motion, these angles vary and the orbital plane needs to be referenced to an initial reference frame which is chosen between the *departure frame* $Ox_0y_0z_0$ or the *perifocal frame* $Ox_p y_p z_p$ at the initial instant (Fig. 3.2b).

In order to finally locate the unit vectors of the perifocal frame $Ox_p y_p z_p$ respect to the unit vectors of the inertial frame, a rotation matrix P_0 is needed, thus the rotation is:

$$[\mathbf{u}_1, \mathbf{u}_2, \mathbf{k}_0] = [\mathbf{i}_1, \mathbf{j}_1, \mathbf{k}_1] P_0 \quad (3.7)$$

where the matrix P_0 is expressed in terms of the Euler angles:

$$P_0 = \begin{bmatrix} +\cos \Omega \cos \omega - \cos i \sin \Omega \sin \omega & -\cos \Omega \sin \omega - \cos i \sin \Omega \cos \omega & +\sin i \sin \Omega \\ +\sin \Omega \cos \omega + \cos i \cos \Omega \sin \omega & -\sin \Omega \sin \omega + \cos i \cos \Omega \cos \omega & -\sin i \cos \Omega \\ +\sin i \sin \omega & +\sin i \cos \omega & \cos i \end{bmatrix} \quad (3.8)$$

Within the idea of the *orbital plane* a complication arises. In the perturbed motion of M the orbital plane is no longer fixed to the inertial frame. From a geometric point of view, there is an infinite number of planes that satisfy the geometric conditions exposed in the previous description. Every one of them has in fact its own rotation velocity relative to the inertial frame with different component along the inertial axis Oz . Between all the possible planes, DROMO theory selects the plane whose angular velocity component along the Oz axis is null and calls it the *ideal frame*. Thus, for consequence, the angular velocity of the orbital plane, in the new optics of the ideal frame, lies strictly in the plane Oxy . Many different frames which satisfy these conditions can be associated to the *orbital plane*, in particular the *departure frame* $Ox_0y_0z_0$ and the *departure perifocal frame* $Ox_p y_p z_p$ are two possible candidates. The DROMO development finally selects the *departure perifocal frame* demonstrating that its angular velocity lies strictly in the Ox axis and it depends solely on the perturbation force \mathbf{F}_p , calling the so obtained orbital plane *rigid body 0*. Fig. 3.3 presents the relation between the orbital frame and the two possible ideal frames.

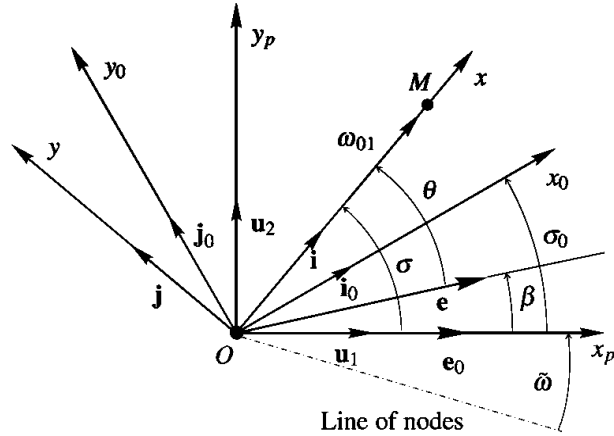


Figure 3.3: Orbital Frame, Departure Frame and Departure Perifocal Frame [22].

3.3.2 DROMO variables definition

DROMO variables are non-dimensionalized. The characteristic values selected for the *longitude*, *time* and *mass* nondimensionalization are:

$$L_c = |\mathbf{x}_0|, \quad \omega_c = \sqrt{\frac{\mu}{L_c^3}}, \quad m_c = m \quad (3.9)$$

which lead to the definition of all the consequent characteristic values:

Table 4: DROMO non-dimensionalization characteristic values.

| DROMO non-dimensionalization characteristic values | | | | | |
|--|------------|--------------|----------------------|------------------|------------------|
| Length | L_c | Acceleration | $\omega_c^2 L_c$ | Angular Momentum | $\omega_c L_c^2$ |
| Velocity | ω_c | Force | $m_c \omega_c^2 L_c$ | Time | ω_c^{-1} |

In particular, the expression for the non-dimensional time is:

$$\tau = \omega_c(t - t_0) \quad (3.10)$$

As said in the introduction to this section, because the DROMO theory splits the motion in two components (the motion *in* the orbital plane and the motion *of* the orbital plane), the most suitable independent variable utilized in the propagation is a fictitious time which will have the characteristics of an angle, the *ideal anomaly*. The *ideal anomaly* σ is defined as the angle between the Ox axis of the orbital frame and the Ox_p axis of the departure perifocal frame and it can be observed in Fig. 3.3 along with the true anomaly θ . At the initial time t_0 both angles are coincident but during the propagation they differ because of the perturbation \mathbf{F}_p .

$$\text{for } t = t_0 : \quad \sigma_0 = \theta_0 \quad (3.11)$$

To introduce the derivatives of motion variables, it is important to fully understand the inertial motion of the orbital plane. Its motion is a *pure rotation* about an axis which lies totally in the inertial plane xy and passes from the origin O , which keeps a fixed position. Thus, following the DROMO notation, first of all it is important to define the attitude of the departure perifocal frame $Ox_p y_p z_p$. It is more effectively represented in terms of an unit *quaternion* \mathbf{n} whose components are defined in terms of the Euler angles of the perifocal frame:

$$\mathbf{n} = \eta_4 + (\eta_1, \eta_2, \eta_3) \quad (3.12)$$

$$\begin{aligned} \eta_1 &= \sin\left(\frac{i}{2}\right) \cos\left(\frac{\Omega - \omega}{2}\right), & \eta_2 &= \sin\left(\frac{i}{2}\right) \sin\left(\frac{\Omega - \omega}{2}\right) \\ \eta_3 &= \cos\left(\frac{i}{2}\right) \sin\left(\frac{\Omega + \omega}{2}\right), & \eta_4 &= \cos\left(\frac{i}{2}\right) \cos\left(\frac{\Omega + \omega}{2}\right) \end{aligned} \quad (3.13)$$

And the aforementioned rotation matrix P_0 in terms of the unit quaternion \mathbf{n} remains:

$$P_0 = \begin{bmatrix} 1 - 2(\eta_2^2 + \eta_3^2) & 2\eta_1\eta_2 - 2\eta_3\eta_4 & 2\eta_1\eta_3 + 2\eta_2\eta_4 \\ 2\eta_1\eta_2 + 2\eta_3\eta_4 & 1 - 2(\eta_1^2 + \eta_3^2) & 2\eta_2\eta_3 - 2\eta_1\eta_4 \\ 2\eta_1\eta_3 - 2\eta_2\eta_4 & 2\eta_2\eta_3 + 2\eta_1\eta_4 & 1 - 2(\eta_1^2 + \eta_2^2) \end{bmatrix} \quad (3.14)$$

The \mathbf{n} quaternion or, what is equivalent, the P_0 rotation matrix are both constant in the Keplerian motion and evolve in the perturbed motion. DROMO theory evaluates the derivatives of the unit quaternion in function of the non-dimensional time:

$$\frac{d\eta_1}{d\tau} = \frac{1}{2} \frac{r}{h} a_{pz} \{\eta_4 \cos \sigma - \eta_3 \sin \sigma\} \quad (3.15)$$

$$\frac{d\eta_2}{d\tau} = \frac{1}{2} \frac{r}{h} a_{pz} \{\eta_3 \cos \sigma + \eta_4 \sin \sigma\} \quad (3.16)$$

$$\frac{d\eta_3}{d\tau} = \frac{1}{2} \frac{r}{h} a_{pz} \{-\eta_2 \cos \sigma + \eta_1 \sin \sigma\} \quad (3.17)$$

$$\frac{d\eta_4}{d\tau} = \frac{1}{2} \frac{r}{h} a_{pz} \{-\eta_1 \cos \sigma - \eta_2 \sin \sigma\} \quad (3.18)$$

It is easy to observe that the variation of the quaternion \mathbf{n} only depends on the orbital plane perpendicular acceleration a_{pz} . This component of the perturbation acceleration depends on the position of the perturbed object in the inertial space, thus, its value has to be determined at every time. To do so, the position of the orbital frame $Oxyz$ is required. Its attitude in the inertial space is given by another unit quaternion, \mathbf{q} :

$$\mathbf{q} = \epsilon_4 + (\epsilon_1, \epsilon_2, \epsilon_3) \quad (3.19)$$

Since the orbital frame only rotates respect to the departure perifocal frame around Oz axis, the relation between the two frames is depicted by the following rotation:

$$[\mathbf{i}, \mathbf{j}, \mathbf{k}] = [\mathbf{u}_1, \mathbf{u}_1, \mathbf{k}] R_3(\sigma) \quad (3.20)$$

Which finally leads to the definition of the \mathbf{q} quaternion in function of the \mathbf{n} quaternion and the ideal anomaly σ .

$$\begin{aligned} \epsilon_1 &= \eta_1 \cos \frac{\sigma}{2} + \eta_2 \sin \frac{\sigma}{2}, & \epsilon_2 &= \eta_2 \cos \frac{\sigma}{2} - \eta_1 \sin \frac{\sigma}{2} \\ \epsilon_3 &= \eta_3 \cos \frac{\sigma}{2} + \eta_4 \sin \frac{\sigma}{2}, & \epsilon_4 &= \eta_4 \cos \frac{\sigma}{2} - \eta_3 \sin \frac{\sigma}{2} \end{aligned} \quad (3.21)$$

Finally, to describe the motion relative to the orbital plane, DROMO theory introduces three variables to describe the dynamic state of the particle, ζ_1 , ζ_2 and ζ_3 . They are defined in function of the non-dimensional angular momentum modulus h of the particle and the eccentricity vector \mathbf{e} in the ideal frame:

$$\mathbf{e} = \zeta_1 \mathbf{u}_1 + \zeta_2 \mathbf{u}_2 \quad (3.22)$$

$$\zeta_3 = \frac{1}{h} \quad (3.23)$$

As said before, the independent variable in DROMO theory is the *ideal anomaly* σ ; as a consequence, the time derivative for all the different magnitudes needs to be calculated in the ideal frame, it is, the time derivatives are expressed as *ideal anomaly* derivatives. As a result, the equations which govern the motion *in* the orbital plane and *of* the orbital plane (included the very derivative of the non-dimensional time) are hereby presented:

$$\frac{d\tau}{d\sigma} = \frac{1}{\zeta_3^3 s^2} \quad (3.24)$$

$$\frac{d\zeta_1}{d\sigma} = +s \sin \sigma (\tilde{a}_{px}) + (\zeta_1 + (1+s) \cos \sigma) (\tilde{a}_{py}) \quad (3.25)$$

$$\frac{d\zeta_2}{d\sigma} = -s \cos \sigma (\tilde{a}_{px}) + (\zeta_2 + (1+s) \sin \sigma) (\tilde{a}_{py}) \quad (3.26)$$

$$\frac{d\zeta_3}{d\sigma} = -\zeta_3 (\tilde{a}_{py}) \quad (3.27)$$

$$\frac{d\eta_1}{d\sigma} = \frac{1}{2} \tilde{a}_{pz} \{ \eta_4 \cos \sigma - \eta_3 \sin \sigma \} \quad (3.28)$$

$$\frac{d\eta_2}{d\sigma} = \frac{1}{2} \tilde{a}_{pz} \{ \eta_3 \cos \sigma + \eta_4 \sin \sigma \} \quad (3.29)$$

$$\frac{d\eta_3}{d\sigma} = \frac{1}{2} \tilde{a}_{pz} \{ -\eta_2 \cos \sigma + \eta_1 \sin \sigma \} \quad (3.30)$$

$$\frac{d\eta_4}{d\sigma} = \frac{1}{2} \tilde{a}_{pz} \{ -\eta_1 \cos \sigma - \eta_2 \sin \sigma \} \quad (3.31)$$

These are the motion equation as presented by DROMO theory and they must be integrated considering the following additional relations:

$$s = 1 + \zeta_1 \cos \sigma + \zeta_2 \sin \sigma \quad (3.32)$$

$$\frac{1}{r} = \zeta_3^2 s \quad (3.33)$$

$$\frac{dr}{d\tau} = \zeta_3 (\zeta_1 \sin \sigma - \zeta_2 \cos \sigma) \quad (3.34)$$

$$\epsilon_1 = \eta_1 \cos \frac{\sigma}{2} + \eta_2 \sin \frac{\sigma}{2} \quad (3.35)$$

$$\epsilon_2 = \eta_2 \cos \frac{\sigma}{2} - \eta_1 \sin \frac{\sigma}{2} \quad (3.36)$$

$$\epsilon_3 = \eta_3 \cos \frac{\sigma}{2} + \eta_4 \sin \frac{\sigma}{2} \quad (3.37)$$

$$\epsilon_4 = \eta_4 \cos \frac{\sigma}{2} - \eta_3 \sin \frac{\sigma}{2} \quad (3.38)$$

3.3.3 Initial conditions

Obviously, the equations shown above must be integrated from the appropriate initial conditions, which should necessarily be derived from the initial *state vector* of M in non-dimensional form $(\mathbf{x}_0, \mathbf{v}_0)$ at the initial time t_0 . It is easy to obtain the unit vectors of the *departure perifocal frame* $Ox_p y_p z_p$ (and, for consequence, the component of the initial quaternion \mathbf{n}_0):

$$\mathbf{k}(0) = \frac{\mathbf{h}_0}{|\mathbf{h}_0|}, \quad \mathbf{u}_1(0) = \frac{\mathbf{e}_0}{|\mathbf{e}_0|}, \quad \mathbf{u}_2(0) = \mathbf{k}(0) \times \mathbf{u}_1(0) \quad (3.39)$$

and the unit vectors of the orbital frame $Oxyz$:

$$\mathbf{i}(0) = \frac{\mathbf{x}_0}{|\mathbf{x}_0|}, \quad \mathbf{j}(0) = \mathbf{k}(0) \times \mathbf{i}(0) \quad (3.40)$$

Finally, the DROMO initial vector at $\sigma(0) = \sigma_0$ is:

$$\begin{aligned}
\tau(0) &= 0, & \zeta_1(0) &= e_0, & \zeta_2(0) &= 0, & \zeta_3(0) &= \frac{1}{h_0} \\
\eta_1(0) &= \eta_{10}, & \eta_2(0) &= \eta_{20}, & \eta_3(0) &= \eta_{30}, & \eta_4(0) &= \eta_{40}
\end{aligned} \tag{3.41}$$

3.3.4 From DROMO variables to the state vector

Once the propagation in DROMO variables has taken place, the resulting vector must be converted in a classical *state vector* in the inertial space which is easily interpreted and manipulated. Thus, the state vector $(\mathbf{x}_1, \mathbf{v}_1)$ of the particle M in dimensional values and in the inertial frame $Ox_1y_1z_1$ is obtained:

$$\mathbf{x}_1 = \frac{L_c}{\zeta_3^2 s} [\mathbf{i}_1, \mathbf{j}_1, \mathbf{k}_1] P_0 \begin{bmatrix} \cos \sigma \\ \sin \sigma \\ 0 \end{bmatrix} \tag{3.42}$$

$$\mathbf{v}_1 = (\omega_c L_c) [\mathbf{i}_1, \mathbf{j}_1, \mathbf{k}_1] P_0 \begin{bmatrix} V_1 \\ V_2 \\ 0 \end{bmatrix} \tag{3.43}$$

where the values of V_1 and V_2 are defined as follows:

$$V_1 = -\zeta_3(\sin \sigma + \zeta_2), \quad V_2 = \zeta_3(\cos \sigma + \zeta_1) \tag{3.44}$$

3.4 DROMO propagator implementation

After the presentation of the DROMO propagator, the *main problem* approach is chosen in order to speed up the calculations.

DROMO theory generates an Initial Value Problem (IVP) whose derivative must be numerically integrated in function of the chosen independent variable. For a big number of objects, this operation needs a considerable amount of time. Looking for a faster propagation based on DROMO theory, it is reasonable to select only the main perturbation components acting on LEO objects and propagate them considering their perturbed motion. The inclusion of the sole Earth's oblateness in the perturbation term \mathbf{F}_p permits to create a fast and reasonably reliable first approximation solution of the problem. Nevertheless, this solution allows to draw important and clarifying conclusions about the objects future behaviour.

3.4.1 DROMO formulation of the *main problem*

As presented before in equation (3.4), the expression of the perturbation potential for the *main problem* is:

$$V_p = \frac{m\mu_\oplus R_\oplus^2 J_2}{2r^3} (3\sin^2 \varphi - 1) \tag{3.45}$$

where instead of the colatitude θ , the latitude φ of the satellite has been chosen. Thus the expression for the perturbation force is:

$$\mathbf{F}_p = -\nabla V_p = -\frac{\partial V_p}{\partial r} \mathbf{u}_r - \frac{1}{r} \frac{\partial V_p}{\partial \varphi} \mathbf{u}_\varphi = -\frac{3m\mu_\oplus J_2 R_\oplus^2}{2r^4} [(1 - 3\sin^2 \varphi) \mathbf{u}_r + \sin(2\varphi) \mathbf{u}_\varphi] \tag{3.46}$$

Where $r = |\mathbf{x}|$, \mathbf{u}_r is the unit vector in radial direction and \mathbf{u}_φ is the unit vector in the along-track direction. It is noticeable that this expression presents a *non-central* component of the

gravitational force, reducing to a central force when the latitude φ of the object is null. In that case, the orbit would lie in the Earth's equatorial plane, being the Earth oblateness symmetrical, not generating a non-central component. Also note that if $J_2 = 0$ the perturbation component of the force would be null, reducing the problem to a two body problem.

The perturbation force must be represented in the orbital frame $Oxyz$ by the means of three scalar products:

$$F_{px} = \mathbf{F}_p \cdot \mathbf{i}, \quad F_{py} = \mathbf{F}_p \cdot \mathbf{j}, \quad F_{pz} = \mathbf{F}_p \cdot \mathbf{k} \quad (3.47)$$

In the following part, every term will be developed. The first term is obtained directly from the previous expression:

$$F_{px} = \mathbf{F}_p \cdot \mathbf{i} = -\frac{3}{2} \frac{m\mu_\oplus}{r^2} J_2 \left(\frac{R_\oplus}{r} \right)^2 (1 - 3(\mathbf{i} \cdot \mathbf{k}_1)^2) \quad (3.48)$$

where it was substituted $\sin \varphi$ with the equal quantity $\frac{z_1}{r} = (\mathbf{i} \cdot \mathbf{k}_1)$. For the rest of the scalar products it is needed to project the perturbation force on the inertial frame $Ox_1y_1z_1$ obtaining:

$$\mathbf{F}_p = -\frac{3}{2} \frac{m\mu_\oplus}{r^2} J_2 \left(\frac{R_\oplus}{r} \right)^2 \left\{ \left(1 - 5 \frac{z_1^2}{r^2} \right) \left(\frac{x_1}{r} \mathbf{i}_1 + \frac{y_1}{r} \mathbf{j}_1 \right) + \left(3 - 5 \frac{z_1^2}{r^2} \right) \frac{z_1}{r} \mathbf{k}_1 \right\} \quad (3.49)$$

And, expressing the unit vector of the orbital frame in terms of the inertial frame:

$$\mathbf{i} = \frac{x_1}{r} \mathbf{i}_1 + \frac{y_1}{r} \mathbf{j}_1 + \frac{z_1}{r} \mathbf{k}_1 \quad (3.50)$$

the following relation can be obtained:

$$\mathbf{F}_p = -\frac{3}{2} \frac{m\mu_\oplus}{r^2} J_2 \left(\frac{R_\oplus}{r} \right)^2 \left\{ \left(1 - 5 \frac{z_1^2}{r^2} \right) \mathbf{i} + \frac{2z_1}{r} \mathbf{k}_1 \right\} \quad (3.51)$$

The expression for the three terms of perturbation is thus:

$$\begin{aligned} F_{px} &= -\frac{3}{2} \frac{m\mu_\oplus}{r^2} J_2 \left(\frac{R_\oplus}{r} \right)^2 \left[\frac{1}{2} - \frac{3}{2} (\mathbf{i} \cdot \mathbf{k}_1)^2 \right] \\ F_{py} &= -\frac{3}{2} \frac{m\mu_\oplus}{r^2} J_2 \left(\frac{R_\oplus}{r} \right)^2 (\mathbf{i} \cdot \mathbf{k}_1) (\mathbf{j} \cdot \mathbf{k}_1) \\ F_{pz} &= -\frac{3}{2} \frac{m\mu_\oplus}{r^2} J_2 \left(\frac{R_\oplus}{r} \right)^2 (\mathbf{i} \cdot \mathbf{k}_1) (\mathbf{k} \cdot \mathbf{k}_1) \end{aligned} \quad (3.52)$$

which must be modified following the DROMO non-dimensionalization:

$$\mathbf{F}_p = mL_c \omega_0^2 \mathbf{a}_p, \quad \omega_0 = \frac{\mu_\oplus}{L_c^3} \quad (3.53)$$

Hence leading to the non-dimensional expressions for the acceleration (the force per unit mass):

$$a_{px} = \mathbf{a}_p \cdot \mathbf{i} = -3\varepsilon \chi^4 \left[\frac{1}{2} - \frac{3}{2} (\mathbf{i} \cdot \mathbf{k}_1)^2 \right] \quad (3.54)$$

$$a_{py} = \mathbf{a}_p \cdot \mathbf{j} = -3\varepsilon \chi^4 (\mathbf{i} \cdot \mathbf{k}_1) (\mathbf{j} \cdot \mathbf{k}_1) \quad (3.55)$$

$$a_{pz} = \mathbf{a}_p \cdot \mathbf{k} = -3\varepsilon \chi^4 (\mathbf{i} \cdot \mathbf{k}_1) (\mathbf{k} \cdot \mathbf{k}_1) \quad (3.56)$$

where:

$$\varepsilon = J_2 \left(\frac{R_\oplus}{L_c} \right)^2 \quad \text{and} \quad \chi = \frac{1}{r} = \zeta_3^2 \cdot s = \zeta_3^2 \cdot (1 + \zeta_1 \cos \sigma + \zeta_2 \sin \sigma)$$

Thus, for the study of the J_2 perturbation in DROMO formulation, the equations of motion are expressed as follows:

$$\frac{d\tau}{d\sigma} = \frac{1}{\zeta_3^3 s^2} \quad (3.57)$$

$$\frac{d\zeta_1}{d\sigma} = -3\varepsilon s \zeta_3^4 \left\{ s \left[\frac{1}{2} - \frac{3}{2} (\mathbf{i} \cdot \mathbf{k}_1)^2 \right] \sin \sigma + [\zeta_2 + (1 + s) \cos \sigma (\mathbf{i} \cdot \mathbf{k}_1) (\mathbf{j} \cdot \mathbf{k}_1)] \right\} \quad (3.58)$$

$$\frac{d\zeta_2}{d\sigma} = -3\varepsilon s \zeta_3^4 \left\{ -s \left[\frac{1}{2} - \frac{3}{2} (\mathbf{i} \cdot \mathbf{k}_1)^2 \right] \cos \sigma + [\zeta_2 + (1 + s) \cos \sigma (\mathbf{i} \cdot \mathbf{k}_1) (\mathbf{j} \cdot \mathbf{k}_1)] \right\} \quad (3.59)$$

$$\frac{d\zeta_3}{d\sigma} = 3\varepsilon s \zeta_3^5 (\mathbf{i} \cdot \mathbf{k}_1) (\mathbf{j} \cdot \mathbf{k}_1) \quad (3.60)$$

$$\frac{d\eta_1}{d\sigma} = -3\varepsilon s \zeta_3^4 \{ \eta_4 \cos \sigma - \eta_3 \sin \sigma \} (\mathbf{i} \cdot \mathbf{k}_1) (\mathbf{k} \cdot \mathbf{k}_1) \quad (3.61)$$

$$\frac{d\eta_2}{d\sigma} = -3\varepsilon s \zeta_3^4 \{ \eta_3 \cos \sigma + \eta_4 \sin \sigma \} (\mathbf{i} \cdot \mathbf{k}_1) (\mathbf{k} \cdot \mathbf{k}_1) \quad (3.62)$$

$$\frac{d\eta_3}{d\sigma} = -3\varepsilon s \zeta_3^4 \{ -\eta_2 \cos \sigma + \eta_1 \sin \sigma \} (\mathbf{i} \cdot \mathbf{k}_1) (\mathbf{k} \cdot \mathbf{k}_1) \quad (3.63)$$

$$\frac{d\eta_4}{d\sigma} = -3\varepsilon s \zeta_3^4 \{ -\eta_1 \cos \sigma - \eta_2 \sin \sigma \} (\mathbf{i} \cdot \mathbf{k}_1) (\mathbf{k} \cdot \mathbf{k}_1) \quad (3.64)$$

and they must be integrated starting from the same initial conditions defined in section 3.3.3 for $\sigma(0) = \sigma_0$:

$$\begin{aligned} \tau(0) &= 0, & \zeta_1(0) &= \zeta_{10}, & \zeta_2(0) &= \zeta_{20}, & \zeta_3(0) &= \zeta_{30} \\ \eta_1(0) &= C_1, & \eta_2(0) &= C_2, & \eta_3(0) &= C_3, & \eta_4(0) &= C_4 \end{aligned} \quad (3.65)$$

where C_1, C_2, C_3, C_4 are the components that define the position of the perifocal frame in the initial instant.

3.4.2 Propagation

All the processed objects are given in the form of an inertial state vector in the GCRF reference frame at a common instant of time. They must be firstly converted in suitable DROMO state vectors following the passages in section 3.3.3.

Once an object is expressed through its DROMO state vector, the routine propagates it through a classical Runge-Kutta 4th order numeric integrator (RK4). This method is here summarized to clarify its implementation and to better explain a following interpolation concept.

The general IVP solved by the Runge-Kutta method is the following:

$$\dot{y} = f(t, y), \quad y(t_0) = y_0 \quad (3.66)$$

Applying the method to the current problem, t is the DROMO independent variable σ , y the object's DROMO state vector, \dot{y} the DROMO derivative with respect to σ and y_0 the initial DROMO vector. Moreover, in the case of the *main problem*, there is the simplification of a

derivative which is independent of the *ideal anomaly* σ , resulting in an autonomous ODEs system. The problem reduces to:

$$\dot{y} = f(y), \quad y(\sigma_0) = y_0 \quad (3.67)$$

And once the increment⁸ of σ has been defined, ($\Delta\sigma = h$), the $(n+1)^{\text{th}}$ DROMO vector is given by:

$$\begin{aligned} y_{n+1} &= y_n + k_n, \\ k_n &= \frac{1}{6}(k_1 + 2k_2 + 2k_3 + k_4), \\ \sigma_{n+1} &= \sigma_n + h \end{aligned} \quad (3.68)$$

where:

$$\begin{aligned} k_1 &= h f(y_n), \\ k_2 &= h f\left(y_n + \frac{k_1}{2}\right), \\ k_3 &= h f\left(y_n + \frac{k_2}{2}\right), \\ k_4 &= h f(y_n + k_3) \end{aligned} \quad (3.69)$$

The propagation is set up and the propagator continues to calculate state vectors till the proper stop conditions. In the case of the present work, the control variable is the time. It can be easily obtained given a state vector using equation (3.10).

Actually, the state vector of the propagated object is needed at precise intervals of time in order to create a database of the objects classical elements at given times. To do so, an interpolation process is needed because of the very foundations of the DROMO propagation: the propagation is made in the σ independent variable (a geometric variable), whilst the time is only a control variable. Hence, to seek the solution at a given instant of time (the *sampling time*) there is the necessity to interpolate.

Considering Fig. 3.4, at every propagation step two quantities are available: y_{n+1} and k_n . By consequence, from eq. (3.68) y_n is easily obtained too. The objective is to compute the value of the solution at the σ_{ST} corresponding to the defined *sampling time* t_{ST} . This is realized by a linear interpolation between the two known values of the solution at σ_n and σ_{n+1} .

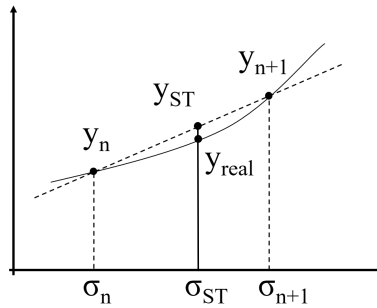


Figure 3.4: Linear interpolation scheme.

⁸In this case, the integration step h uses the same notation as the non-dimensional angular momentum h as defined in section 3.3.2. h symbol is traditionally used for both quantities.

Defined:

$$\phi = \frac{t_{ST} - t_n}{t_{n+1} - t_n} = \frac{\tau_{ST} - \tau_n}{\tau_{n+1} - \tau_n} \quad (3.70)$$

the interpolated value is obtained with the following relation:

$$y_{ST} = (1 - \phi) y_n + \phi y_{n+1} = y_{n+1} - (1 - \phi) k_n \quad (3.71)$$

The linear interpolation obtains the value y_{ST} which is slightly different from the real value y_{real} of the function at the corresponding value of σ_{ST} . In the optics of this work, this approximation is accepted and a further development of the tool could reduce this error considering a parabolic interpolation.

3.5 Propagation results

Once the object has been propagated, a database with all the sampling time steps and the corresponding DROMO state vectors is obtained. Every DROMO state vector is then processed and transformed to an inertial state vector which is finally transformed to a vector containing the six classic elements of the orbit: the *semi-major axis* a , the *eccentricity* e , the *inclination* i , the *argument of the perigee* ω , the *right ascension of the ascending node* Ω and the *true anomaly* θ .

In order to make the output of the data easily readable by any other interfacing program, it has been decided to store the results of the propagation in a text file. It can be further analysed in an easy way. Because the final objective of the work is to analyse the threats constituted by the space debris to the ISS, every space object orbit which is processed and propagated is directly compared with the ISS orbit. To do so, every line of the output file contains a timestamp, the name of the first object (the ISS), five orbital elements of it along with the name of the compared object (the space debris)⁹ and its five orbital elements. The 5 selected classical elements are: the *semi-major axis* a , the *eccentricity* e , the *right ascension of the ascending node* Ω , the *inclination* i and the *argument of the perigee* ω , presented in this order. It is important to underline that 5 elements are sufficient to define a unique orbit because the position in the orbit is finally uniquely defined by the *true anomaly* θ . Since the objective is the computation of the distance between orbits and not the distance between the very orbiting bodies (which varies much faster and it is not representative), finally it has been decided to output these elements per each object at exactly the same instant of time (the timestamp).

Every line of the output file is thus composed by thirteen fields separated by spaces containing the useful information for the next analysis (Fig. 3.5).

| | | | | | | | | | | | | |
|------------------------|----------------------|----------|---------|----------------|-----------|----------------|------------------------------|----------|---------|----------------|-----------|----------------|
| <i>Timestamp</i> [MJD] | <i>ISS' TLE name</i> | a [km] | e [-] | Ω [rad] | i [rad] | ω [rad] | <i>Space Object TLE name</i> | a [km] | e [-] | Ω [rad] | i [rad] | ω [rad] |
|------------------------|----------------------|----------|---------|----------------|-----------|----------------|------------------------------|----------|---------|----------------|-----------|----------------|

Figure 3.5: Propagation output line format.

Once the ISS and the space object propagations lines have ended, the file presents a *new* couple of objects beginning from the starting time (the first of them being once again the ISS) and the pattern continues till the last object present in the TLEs input file is analysed and his propagation is printed.

⁹Actually, the name of the debris is followed by its NORAD's Catalog Number in order to differentiate between debris pertaining to the same initial object (e.g. FENGYUN-1C-DEB-35088).

4 MOID calculation

After the propagation of all the objects of interest has been carried out, it is time for the Minimum Orbital Intersection Distance (MOID) to be computed. Two orbits are defined at equispaced instants of time in the interval of propagation. It is now very useful to calculate the MOID at each one of the timestamps in order to have the overall MOID variation in the period of interest. To reach the objective of an effective and rapid MOID computation, the method developed by the Space Dynamics Group (SDG - UPM) (Hedo, Ruíz and Peláez) [23] has been used. It is a newly developed iterative method proposed by the SDG in 2018 which ensures a “fast and precise [...] MOID computation”.

4.1 Basis of the method

The Minimum Orbital Intersection Distance is, by definition, the distance between the closest points of the osculating orbits of two bodies. The principal field of application of the MOID is obviously related to the avoidance of space collisions between objects orbiting a common primary. They could be possible collisions between the Earth and any hazardous object from the solar system or could be collisions between different objects orbiting the Earth (spacecraft and space debris for instance).

The problem can be formulated as the search of the minimum distance between two sets of points embedded in the Euclidean 3-space (\mathbb{R}^3). In most MOID calculations, the two orbits can be considered as confined, thus the problem is the computation of the minimum distance between two confocal Keplerian osculating ellipses. One of the orbits is considered as the target or the reference (the primary) while any other orbit which is coupled to the primary and studied is called secondary, but the roles can be exchanged as well (Fig. 4.1).

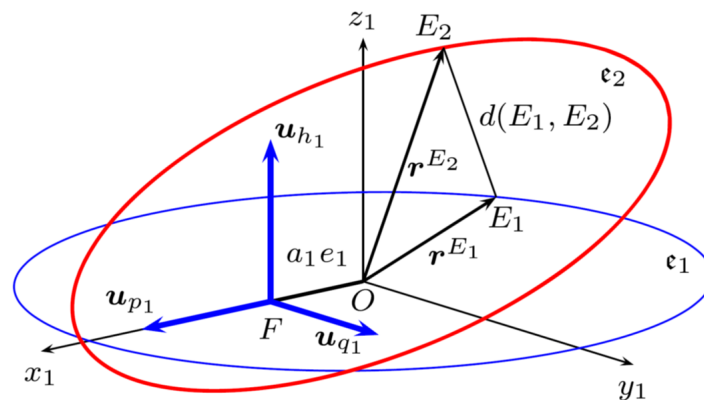


Figure 4.1: Relative geometry of two confocal elliptical orbits [23].

This problem has been studied since the mid-20th century because of its great importance. A considerable number of methods has been developed since then and they can be divided in three main categories: algebraic methods, which mainly deal with the geometry of the problem and rely on algebraic calculations; numerical methods which seek the minimum by numerical

iterations; hybrid methods which try to unify the best of the two previous approaches. The method here presented is a numerical iterative method that is based on two algorithms:

- Algorithm 1: For a given point P_0 its distance to the primary ellipse ϵ_1 is computed (Fig. 4.2).
- Algorithm 2: As the point P_0 moves along the secondary ellipse, the implementation of Algorithm 1 at every passage leads to a set S of minimum distances to ϵ_1 . The absolute minimum of the set is then selected being it the MOID (Fig. 4.1).

These two algorithms are successfully embedded in a tool which permits the MOID obtention in a very fast way.

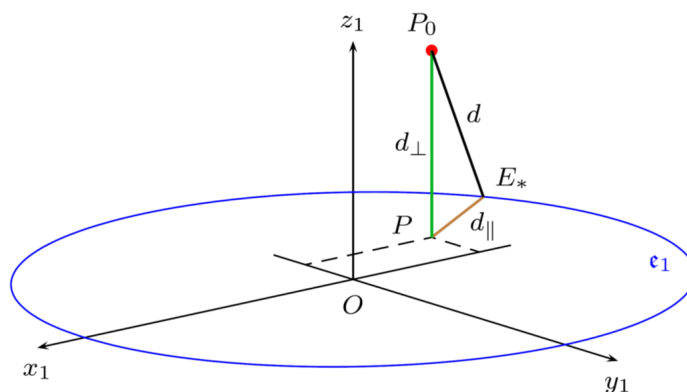


Figure 4.2: Distance from a point to an ellipse in \mathbb{R}^3 [23].

4.2 Algorithm 1

Considering the two ellipses ϵ_1, ϵ_2 defined in Fig. 4.1 with common focus in F , the MOID is the minimum Euclidean distance between them:

$$MOID = d(\epsilon_1, \epsilon_2) = \min_{E_1 \in \epsilon_1, E_2 \in \epsilon_2} d(E_1, E_2) \quad (4.1)$$

This distance is easily obtainable if it is expressed in function of the eccentric anomalies:

$$d(\epsilon_1, \epsilon_2) = \min_{u_1, u_2 \in 2\pi} d[E_1(u_1), E_2(u_2)] \quad (4.2)$$

For the distance between two generic points in the ellipses (Fig. 4.1), the general expression is:

$$\mathbf{E}_1 \mathbf{E}_2 = d(u_1, u_2) = |\mathbf{O} \mathbf{E}_1(u_1) - \mathbf{O} \mathbf{E}_2(u_2)| = \sqrt{\sum_{i=1}^3 (x_i^{E_1}(u_1) - x_i^{E_2}(u_2))^2} \quad (4.3)$$

where:

$$x_i^{E_j}(u_j), \quad i = 1, 2, 3 \quad (4.4)$$

are the parametric equations of Ellipse j expressed in cartesian coordinates as function of the eccentric anomaly u_j ($j = 1, 2$).

It can be observed that the MOID calculation is an unconstrained minimization of a two variables function. Moreover, the function $d(u_1, u_2)$ is 2π -periodic in both eccentric anomalies. The final domain of the equation 4.3 is thus defined by $(u_1, u_2) \in [0, 2\pi] \times [0, 2\pi]$ which is a topological torus in the Euclidean space \mathbb{R}^3 .

4.2.1 Distance computation

The basis of Algorithm 1 is constituted by dividing the distance from a point to an ellipse into two main components: the distance normal to the plane of the ellipse and the distance in the plane of the ellipse.

Considering Fig. 4.2, $P_0 \in \mathbb{R}^3$ is a generic point and $\mathbf{e}_1 \in \mathbb{R}^3$ an ellipse whose eccentric anomaly is $u \in [0, 2\pi]$. The distance between them is defined as:

$$d(P_0, \mathbf{e}_1) = \min_{u \in [0, 2\pi]} d(P_0, E(u)) = \min_{u \in [0, 2\pi]} d(u) \quad (4.5)$$

Therefore, if P is the orthogonal projection of P_0 on the plane of \mathbf{e}_1 its distance to the ellipse can be expressed as follows:

$$d(P_0, \mathbf{e}_1)^2 = d_{\perp}^2 + d_{\parallel}^2 = |\mathbf{P}_0 \mathbf{P}|^2 + |\mathbf{P} \mathbf{E}_*|^2 \quad (4.6)$$

where E_* is the point of the ellipse which gives minimum distance.

As far as P_0 is kept fixed, the out-of-plane distance d_{\perp} is constant. Hence, only the in-plane distance needs to be minimized. Since $Ox_1y_1z_1$ are symmetry axes of the ellipse, distance to point P_0 is invariant to symmetries respect to coordinate planes. The study is therefore reduced to the first octant of $Ox_1y_1z_1$, and considering the in-plane projection P the study can be reduced to the first quadrant of Ox_1y_1 .

Once the in-plane minimum distance is evaluated, equation 4.6 allows to obtain the minimum spatial distance between point P_0 and ellipse \mathbf{e}_1 .

4.2.2 In-plane distance between a point and an ellipse

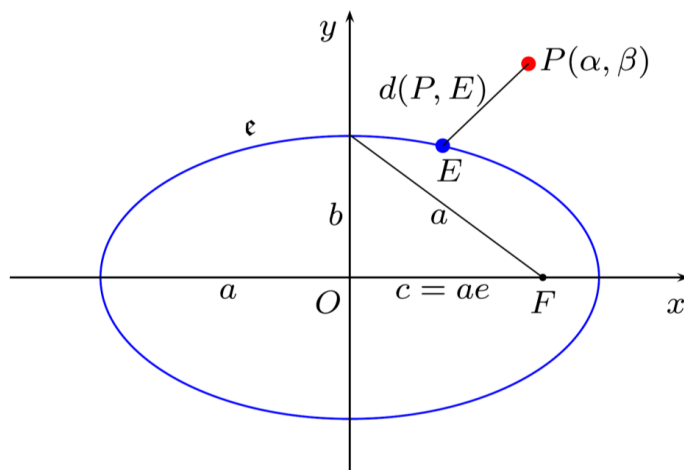


Figure 4.3: In-plane distances between an ellipse and a coplanar point [23].

Considering Fig. 4.3 which represents the ellipse ϵ whose axes of symmetry are Ox_1y_1 and whose semi-axes are a and b , the minimum distance between P and E is:

$$d(P, \epsilon) = \min_{E \in \epsilon} d(P, E) \quad (4.7)$$

and it can be expressed in function of the Cartesian coordinates of the point P in Ox_1y_1 , thus leading to the expression of the minimization problem to solve:

$$d^2(P, \epsilon) = \min_{(x,y) \in \epsilon} [(x - \alpha)^2 + (y - \beta)^2] \quad (4.8)$$

where x and y obviously must solve the ellipse equation:

$$\frac{x^2}{a^2} + \frac{y^2}{b^2} = 1. \quad (4.9)$$

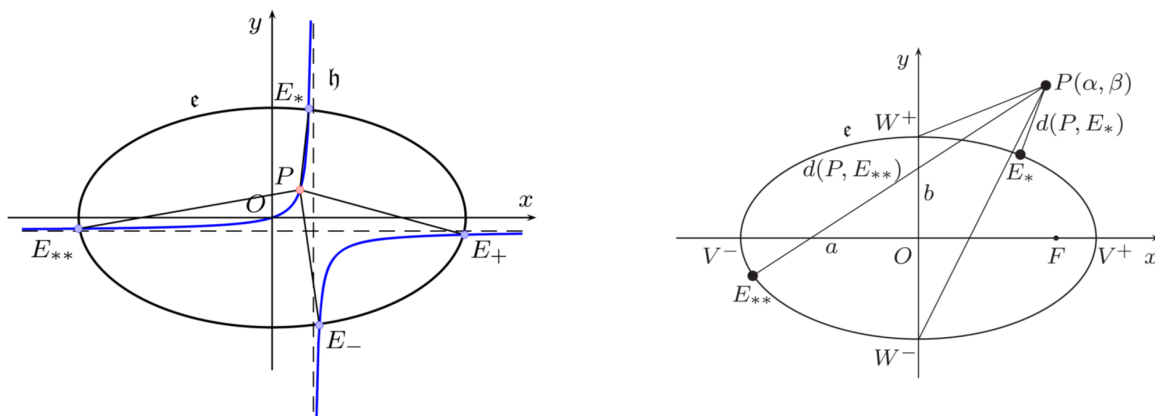
After some operations, the following equation must be satisfied together with eq. (4.9):

$$xy(a^2 - b^2) - \alpha a^2 y + \beta b^2 x = 0 \quad (4.10)$$

which is the implicit expression of an equilateral hyperbola \mathfrak{h} of asymptotes parallel to the axes, passing through P and O (Fig. 4.4a). Every intersection point between the two conics ϵ and \mathfrak{h} is a solution of equations 4.9 and 4.10 and in that points the distance to P has a stationary value. Eliminating y between equations 4.9 and 4.10 in fact produces:

$$x^4 e^4 - 2\alpha e^2 x^3 - (a^2 e^4 + \beta^2 e^2 - [\alpha^2 + \beta^2])x^2 + 2\alpha e^2 a^2 x - a^2 \alpha^2 = 0 \quad (4.11)$$

which is a quartic with real coefficients, thus the possible intersections between two conics consist of 0, 2 or 4 points counted with their multiplicities, and because the hyperbola \mathfrak{h} by construction passes by the centre O of the ellipse ϵ , the two curves have at least two points of intersection: it is deduced that the problem of extreme distances always has a solution.



(a) Intersections between the ellipse ϵ and the hyperbola \mathfrak{h} . (b) Extreme distances versus those to vertices W^+ and W^- .

Figure 4.4: Reference frames definition [23].

With some geometrical reasoning, it can be deduced from Fig. 4.4a and Fig. 4.4b that the distances between the point P and the extremes of the ellipse and the point P and the intersection points of the hyperbola and the ellipse are subjected to the following relation:

$$d(P, E_*) < \min(d(P, V^+), d(P, W^-)) < d(P, E_-) \leq d(P, E^+) < d(P, E_{**}) \quad (4.12)$$

Thus, it can be inferred that not only the problem has at least two extreme points, but also that one of them is the *global minimum* of the distance PE and the other is the *global maximum* of it.

Moreover, and other interesting result can be drawn introducing the concept of the *plane evolute*¹⁰. It is known in fact, that for critical distances, \mathbf{PE} is normal to the ellipse \mathbf{e} and tangent to its plane evolute \mathbf{p} (Fig. 4.5). Since all normals are tangent to the plane evolute, there are as many real roots of equation 4.11 as tangents from P to \mathbf{p} . The number depends on the position of P relative to \mathbf{p} . It is important to underline that there may be two different real roots that give minimum distance because of the symmetries.

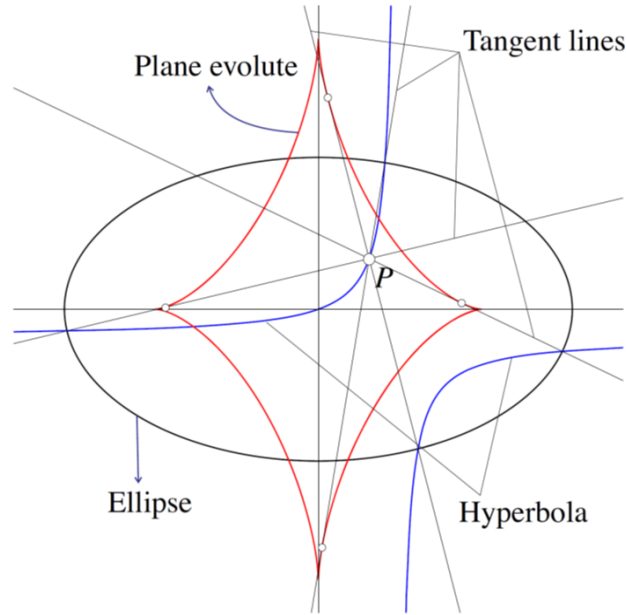


Figure 4.5: Tangent lines to the plane evolute of an ellipse from an interior point [23].

4.2.3 Parametric solution approach

Once a geometric analysis of the problem has been carried out, the values of the critical points must be found, it is, the roots of equation 4.11 must be computed. The SDG method is based on the parametric representation of this equation because of the possibility to solve it with a numerical iterative approach.

Thus, considering the parametric equations of the ellipse \mathbf{e} 4.6 in function of the eccentric anomaly $u \in [0, 2\pi]$:

$$x(u) = a \cos(u); \quad y(u) = b \sin(u) \quad (4.13)$$

¹⁰The *plane evolute* of a curve is the locus of all its centres of curvature. It means that if the centre of curvature of each point on the curve is drawn, the evolute would be the resulting figure.

The distance $d(P, E)$ is:

$$d(u; a, b, \alpha, \beta) = \sqrt{(\alpha - a \cos u)^2 + (\beta - b \sin u)^2} \quad (4.14)$$

where u is the independent variable and a, b, α, β are the four parameters of the problem. Using the squared distance, leads to a simplification in the computation of the stationary points u^* and they are searched by annulling the first derivative:

$$f(u; a, b, \alpha, \beta) = \frac{d[d^2(u; a, b, \alpha, \beta)]}{du} = \alpha a \sin u - \beta b \cos u - c^2 \sin u \cos u \quad (4.15)$$

whose real roots are the eccentric anomalies of the points of ellipse ϵ with stationary distance to $P(\alpha, \beta)$.

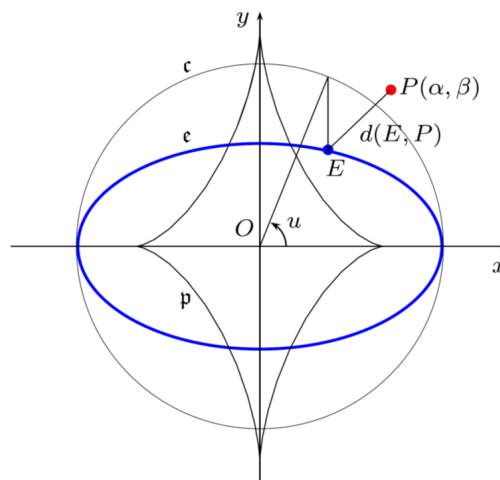


Figure 4.6: Geometry of the in-plane distance problem in parametric equations. [23]

In order to solve equation 4.15, the SDG group [23] considers a generic case and assumes that P is in the first quadrant of Ox_1y_1 ($\alpha > 0, \beta > 0$) and solves it with the application of a numerical method, preferring it to the classic quartic polynomial solution because of its higher rapidity and accuracy respect to the analytic solution.

Numeric iterative method

In the generic conditions above mentioned, the problem of finding the in-plane minimum distance between $P(\alpha > 0, \beta > 0)$ and ϵ reduces to the search of the root of the univariate function $f(u)$ (Equation 4.15) in the open interval $(0, \frac{\pi}{2})$, because other cases (when P is upon one of the axes, $\alpha = 0$ and/or $\beta = 0$) give trivial solutions.

In order to solve equation 4.15, which is transcendental, an iterative root-finding method is needed; moreover, being the function non-linear and of class C^∞ , high-order iterative methods can be used. To ensure convergence, the SDG method applies the fixed-point theorem in order to demonstrate the existence and uniqueness of a solution:

$$\Phi(u) = \arctan \left(\frac{\beta \sqrt{1 - e^2} + a e^2 \sin u}{\alpha} \right) = u. \quad (4.16)$$

Finally, Halley's iterative method is preferred because of its higher speed respect to a more conventional Newton-Raphson method.

4.3 Algorithm 2

As anticipated in section 4.1, Algorithm 2 is a routine loop which executes Algorithm 1 at every passage. In particular, the following steps are executed:

1. Discretization of the secondary orbit ϵ_2 , Algorithm 1 call for each anomaly value of ϵ_2 in order to compute the minimum distance to ϵ_1 and isolation of each minimum in an anomaly interval.
2. Refinement of the search by a golden section search algorithm.
3. Selection of the global minimum between the former values.

4.3.1 Discretization and minimum distance computation

Orbit ϵ_2 is divided in an uniform grid of $N + 1$ values $\{u_2^0, u_2^1, \dots, u_2^N\}$ in the interval $u_2 \in [0, 2\pi]$ where u_2 is the eccentric anomaly of ϵ_2 . A corresponding grid of N image points $\{E_2^0, E_2^1, \dots, E_2^{N-1}\}$ is defined in ϵ_2 ($E_2^0 = E_2^N$). Because there can be more than one minimum of the distance between the points of two confocal ellipses (actually there can be up to four minima), the choice of the value of N is subordinated to the detection of all of them in every case for an accuracy reason. Moreover, the value for N must be the smallest number possible for speed reasons. The SDG method makes an analysis of all possible cases and finally selects $N = 50$ as a value which satisfies both the criteria.

The application of Algorithm 1 for each u_2 respect to the ellipse ϵ_1 allows to have a reticular approximation of the function:

$$\Phi(u_2) = \min_{u_1 \in [0, 2\pi]} d(u_1, u_2) \quad (4.17)$$

which is used to insulate the abscissa of each relative minimum of $\Phi(u_2)$ within an interval.

4.3.2 Global minimum search

Once the analysis of $\Phi(u_2)$ finds the intervals isolating a minimum, each interval is narrowed until the requested precision is reached. A *Golden section search* is applied in the defined interval because of its superiority relatively to other interval search algorithms as bisection and ternary search.

The smallest local minimum among the ones found during this last search is by definition the *global minimum* of the distance between two confocal elliptical orbits, and that is the MOID.

4.4 Implementation

The routine has been used in order to calculate the MOIDs between the ISS and every space object or space debris analysed through the TLEs' database.

As said in the previous chapter, the output of the DROMO propagator is a text file which contains at every line a timestamp and the elements defining the two osculating orbits in that instant of time. The MOID computation routine reads this file as an input and computes the

MOID between the ISS and the corresponding space debris at every specified instant of time. As underlined in the previous chapter, the selected orbital elements are: the *semi-major axis* a , the *eccentricity* e , the *right ascension of the ascending node* Ω , the *inclination* i and the *argument of the perigee* ω . These classical elements are sufficient for the osculating orbit definition and thus, the SDG routine utilises them to calculate timestep by timestep the MOID between the two objects.

The results are presented in an output file. In this case, every line of it presents: the timestamp, the name of the first object (actually it is always the ISS), the name of the object whose orbit is being compared to the first and the corresponding MOID (Fig. 4.7)

| <i>Timestamp</i> [MJD] | <i>ISS TLE name</i> | <i>Space Object TLE name</i> | <i>MOID</i> [km] |
|------------------------|---------------------|------------------------------|------------------|
|------------------------|---------------------|------------------------------|------------------|

Figure 4.7: MOID calculation output line format.

5 Results analysis

The two theories developed by the SDG have been implemented and adapted to form an operative tool for MOID monitorization (DROMOID). Now, after the exposition of the theoretical basis of the methods, some experimentation is needed in order to characterize the solution and validate the tool.

It is important to remember that the main interest of this work is the analysis of the time evolution of the MOID of two objects orbiting the Earth. This leads to the comprehension of MOID's behaviours over time and ultimately its reasonable and logical monitorization.

By the study of some representative cases, some general behaviours and trends can be deduced, allowing to discriminate between hazardous and not-hazardous cases.

5.1 DROMO theory and MOID computation implementation

In the previous chapters, the data processing has been detailed at every stage in order to have an idea of its direct implementation; nevertheless, the whole process will be now recapitulated to create a clear vision of the data flow.

The main stages of the process are summarized as follows:

1. The data are downloaded from the CelesTrak website (<https://celestrak.com>) in the form of text files containing the TLEs which are going to be analysed. The first TLE of the file corresponds to the object with respect to all the other objects will be compared. In the case of this work, the first object shall be the ISS (Zarya module, as declared in the TLE).
2. The TLE data file is given to the first module which receives it as input.
3. The first module processes the data: every TLE is propagated with the SGP4/SDP4 to a common instant of time, the resultant state vector is transformed to the GCRF reference frame and propagated for a specified interval of time; its value is finally saved at equispaced intervals of time.
4. The module saves the data in an output file: every line of it contains (Fig. 3.5) the information of the ISS and a space debris at every timestamp.
5. The file is given as an input to the second module.
6. The second module computes for every line of the input file the MOID between the two objects at the specified instant of time and saves the result in a new line of a new output file.
7. The output file contains the information of the MOID evolution between two space objects over time. It can be now easily visualized.

As a little example of many objects propagation, different space debris are considered along with the ISS and the MOID is evaluated over 1 day period time with 1 s sampling interval. The initial time is midnight, 11th of October 2018, which corresponds to 58 402.000 MJD. The general results are displayed in Fig. 5.1, while a more detailed graphics shows the lower MOIDs (Fig. 5.2).

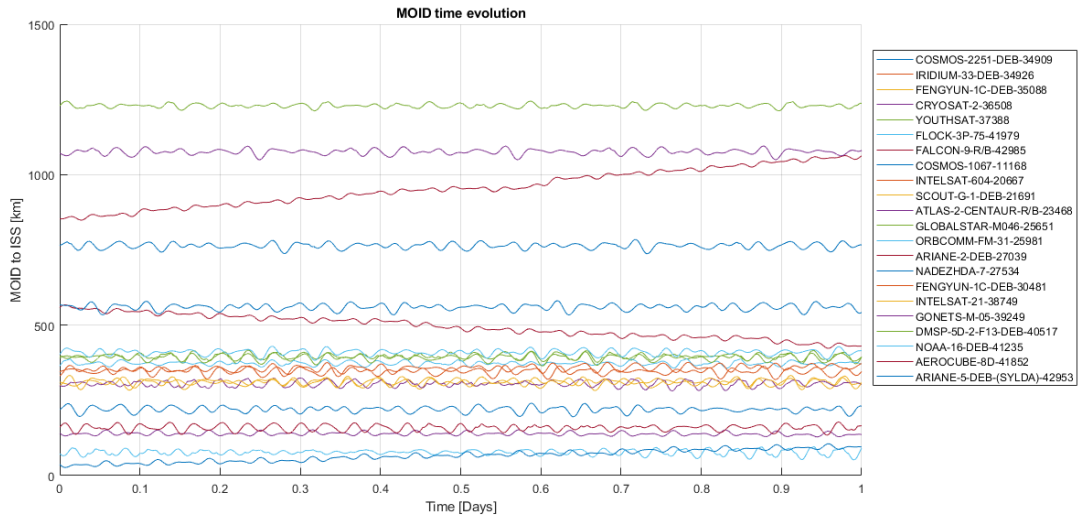


Figure 5.1: ISS MOID evolution of some representative debris during 1 day.

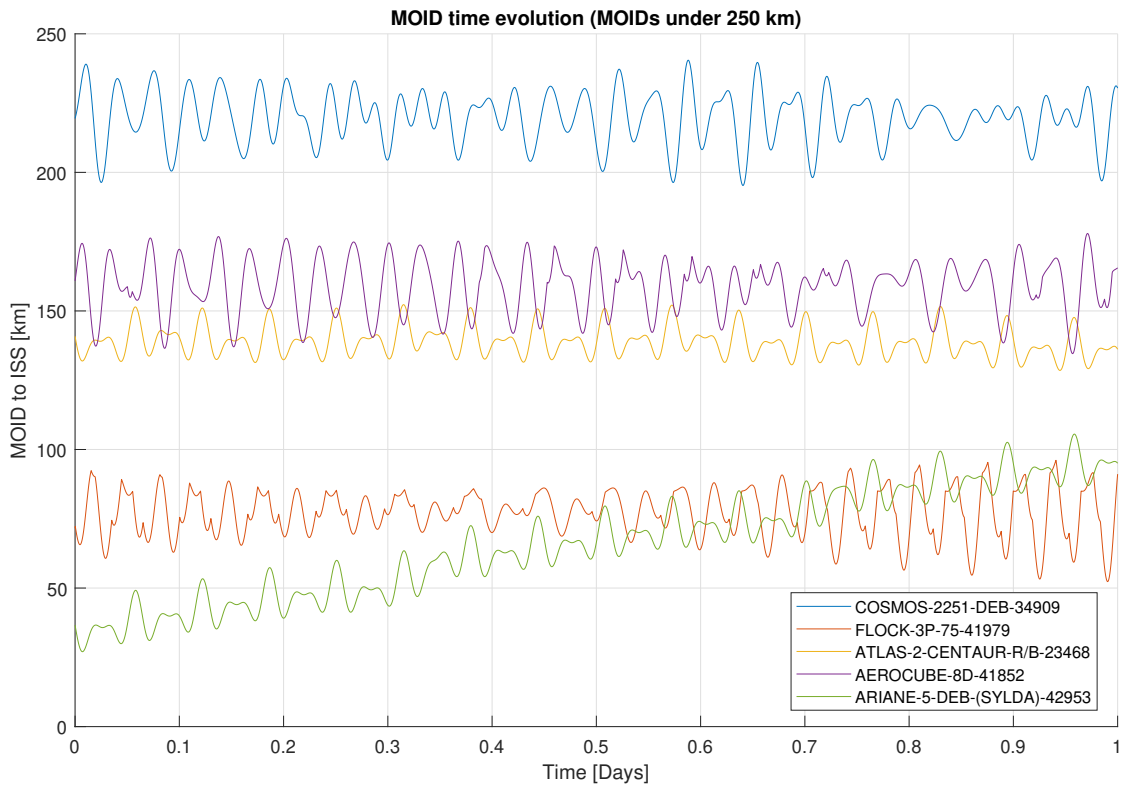


Figure 5.2: ISS MOID evolution of some representative debris during 1 day, MOIDs under 250 km.

The above graphics represent a typical result of the tool. Many MOID evolutions are plotted at the same time in order to distinguish the most *critical* cases in the considered period. The most *dangerous* cases are selected for a detailed analysis, while the others can be discarded at least till a following new analysis.

As can be observed in the graphics, the MOID evolution over time is a complex phenomenon. By a rapid analysis of the MOID time variation curve, different timescales can be appreciated. Almost every curve presents a very curly behaviour as the MOID variation has a *periodic* (in the sense of *non secular*) component which makes the MOID vary quite rapidly. Moreover, a *secular* component can be clearly observed in some particular cases such as the *Ariane 5 SYLDA adapter* in Fig. 5.2; in this case of one day evolution the MOID appears to secularly increase. The MOID varies because the very objects osculating orbits are subjected to perturbations which make them vary over time. Thus, the different timescales which govern the MOID evolution are strongly related to the different timescales in which the orbits vary.

Several associated periods can be found in the MOID time evolution. It is important to investigate the different periodic variations at all timescales in order to correctly discriminate the causes which originate the orbits variability and, by consequence, the MOID variability. In order to approach the MOID time evolution study, it is thus convenient to split it in two parts. The first and most immediate analysis is the short term analysis (1-2 days in the future) which can explain the periodic variations and thus the intervening frequencies observed in the examples. The second is the long term analysis (months, years in the future) and it is needed to investigate the causes of MOID evolution in a larger period allowing to draw conclusions over its far future behaviour.

5.2 Short term analysis

Considering the short term analysis, some examples can be studied to investigate what frequencies determine the MOID instantaneous evolution. As in the example of Fig. 5.1, the starting point of the propagation is 58 402.000 MJD. The considered TLEs are hereby presented:

```
ISS (ZARYA)
1 25544U 98067A 18283.21590318 .00001824 00000-0 35183-4 0 9990
2 25544 51.6419 165.4892 0003533 264.2491 242.0238 15.53798400136402
COSMOS 2251 DEB
1 34909U 93036ADE 18283.15415979 .00000295 00000-0 57285-4 0 9996
2 34909 74.0161 105.9568 0105857 179.6894 180.4360 14.64503102509204
AURORA 1
1 2876U 67065B 18282.06295526 .00000002 00000-0 53043-3 0 9993
2 2876 90.1303 307.5600 0073145 249.4948 109.8026 8.36563268944563
BREEZE-M DEB
1 35546U 06006CP 18282.11456277 .00004477 00000-0 96335-2 0 9999
2 35546 51.2368 245.7644 2624037 129.9059 256.3566 9.27265999231244
FENGYUN 1C DEB
1 33733U 99025DHW 18282.97750442 .00001077 00000-0 66022-3 0 9997
2 33733 99.1887 277.6016 0109684 322.4944 92.7425 14.05101153534640
GLOBALSTAR M046
1 25651U 99012C 18283.05307701 -.00000129 00000-0 -44829-3 0 9999
2 25651 52.0036 128.4381 0003063 57.7532 104.9932 12.09333481888528
```

Figure 5.3: Considered TLEs for the short term analysis.

Cosmos 2251 debris

The first example presents a debris from the Iridium-Cosmos collision of 2009 (NORAD Catalog Number: 34909). It belonged to the Cosmos 2251 satellite that moved in a polar orbit at an altitude of nearly 800 km (778 km perigee, 803 km apogee). The ISS and the fragment from the Cosmos 2251 satellite have been propagated for one day at 1 s sampling interval.

As shown in Fig. 5.4, the MOID daily evolution appears as a collection of maximum and minimum values following one another in a rapid succession. The visualization of all the critical points is assured by the very narrow sampling time of 1 second.

The MOID variability appears to have a possible harmonic behaviour. It seems to be the superposition of different sinusoidal and cosinusoidal functions with different frequencies. It spans a range of dozens of kilometres and no immediate conclusions can be drawn by a simple sight. For this reason, a Discrete Fourier Transform (DFT) is applied on the MOID evolution function in order to study its frequency spectrum. The resultant DFT will present the characteristic frequencies contributing to its generation and some explication can be formulated to explain their presence. Appendix A summarizes the DFT fundamental theoretical basis and how it is applied to the present analysis.

The DFT theory is based on the analysis of periodic functions. It is important to observe that the MOID daily evolution is not necessarily a periodic function by itself. For this reason, an assumption is necessary: the MOID function will be considered to be periodic, with a period of one day. In this case, the set of 86 400 MOID samples representing one day evolution (1 sample per second) will be the sampling period for the DFT ($f_0 = 1 \text{ d}^{-1}$ is the base frequency of this DFT analysis). The MOID DFT will be studied in order to understand the *Fundamental frequencies* of the considered objects motion and their multiples, the *harmonics*.

From the analysis of Fig. 5.5, interesting results can be observed. There are two peaks on the right which correspond to multiples 15 and 16 of the base frequency¹¹ f_0 . These two frequencies correspond to the first not null contributions of the DFT. They are not multiple of a previously found frequency, thus it can be derived that they correspond to two *fundamental frequencies*. The height of the peaks represent the influence of the corresponding frequencies to the overall MOID evolution. The next peaks in the graphic are the 30 and 32 multiples. Looking for possible divisors, it is found out that they are exactly twice the fundamental frequencies, they are the second harmonics. The further visible peaks are the 45 and 48 multiples and correspond to three times the fundamental frequencies. After them, no other appreciable peak can be deduced in the graphic. The MOID evolution for the two object is thus reduced to the contributions of its two fundamental frequencies and their second and third harmonics. Furthermore, after the first six peaks, the DFT analysis shows very screened data and no more peaks can be reasonably deduced.

Now, the two fundamental frequencies must be somehow related to the two satellites orbital movements. The more obvious figures to which the frequencies can be related are the satellites orbital periods. Looking at the ISS and Cosmos TLEs in Fig. 5.3, it is observed that they take the 15.54 and 14.65 values respectively. They match very close the two fundamental frequencies obtained by the DFT analysis. It is logical to associate these frequencies to revolution per day of the two objects, as they are the most immediate periodic behaviour of the satellites. The deduction applies also to the corresponding harmonics.

Another result to observe is that the peaks are not perfectly resolved, i.e, they are hard to distinguish from other spurious peaks. It is the logical consequence of the discretization made for

¹¹Appendix A explains how to correctly interpret this fact.

the analysis. The two satellites daily revolutions are not integer values, their frequencies cannot be expressed as integer multiples of the base frequency. Nevertheless, the frequency contributions in Fig. 5.5 are an approximation of the real values and they can be easily associated with the two satellites.

This last explanation allows not to misinterpret the apparently congruence of the two orbits. The 15 and 16 fundamental frequencies have a least common multiple ($15 \times 16 = 240$), leading to a possible *orbital resonance* between the two objects. It could be deduced that the two objects will never collide thanks to this fact. Considering that the DFT analysis is an approximate result and that the real daily revolutions of the two objects do not have a least common multiple (they are real numbers) the *orbital resonance* concept is discarded.

Aurora 1 satellite

The ISS and the Cosmos 2251 debris have too similar orbital periods. If the orbital periods are the principal contribution to the MOID evolution frequency spectrum, it is possible to better differentiate between the frequency contributions by the optimal selection of the two studied objects. Another satellite has been considered, with the aim to obtain DFT contributions easy to identify. The inactive Aurora 1 satellite (NORAD Catalog Number: 2876) was a scientific satellite for auroras study, launched by the United States in 1967. It has a high inclination orbit, needed for the purposes of its field of study. It has a period of 172.1 min thus making 8.37 revolutions per day. As for the first example, the MOID has been computed over one day at 1 second sampling interval.

It is important to understand the illustrative purpose of the example. The satellite was selected for its orbit characteristics: its orbital period is different from the ISS orbital period making it a good candidate for frequency analysis. Nevertheless, it has a very low eccentricity thus making the orbit nearly circular (like the ISS). The obvious deduction is that the two orbits are at very different heights because of the inverse proportionality between the height and the orbital period. As shown in Fig. 5.6 the MOID is above 3000 km during all the considered period, confirming the reasoning. The satellite is a non-dangerous case¹².

The analysis of the MOID evolution DFT (Fig. 5.7) shows again interesting results. The first peak to be observed is the multiple 9 of the base frequency; it is a fundamental frequency. The following peak to be observed is the multiple 16 and again, it is a fundamental frequency. From now on, the visible peaks are: the 18 peak, which can be associated to the first fundamental frequency second harmonic and the 26 peak which can be associated to the third harmonic. The 32 and 48 peaks are very similar to the ones observed in the Cosmos 2251 debris case. Following the previous analysis, these frequencies can be associated with the Aurora 1 and ISS revolutions per day. The 8.37 orbits per day of Aurora 1 can be in fact the main cause of the 9, 18 and 26 contributions of the DFT analysis. The ISS contributions have already been discussed in the previous case.

¹²Actually, a filter like the first geometrical filtering stage proposed by Hoots (the perigee-apogee filter [8]), would have discarded the Aurora 1 satellite in the first place.

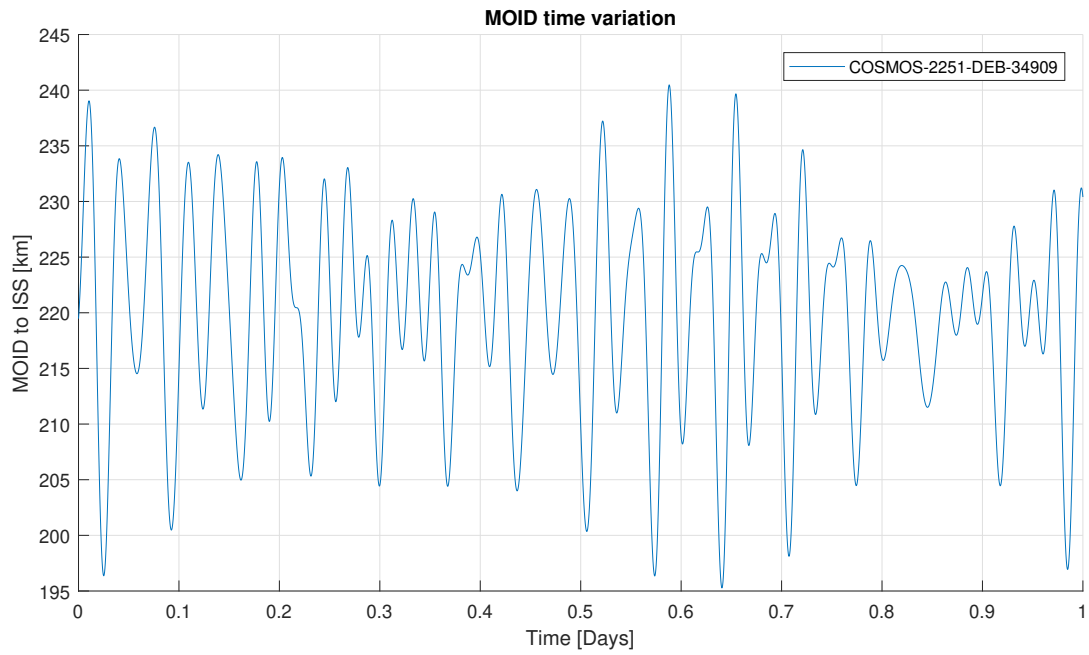


Figure 5.4: Cosmos 2251 debris MOID to ISS evolution during 1 day.

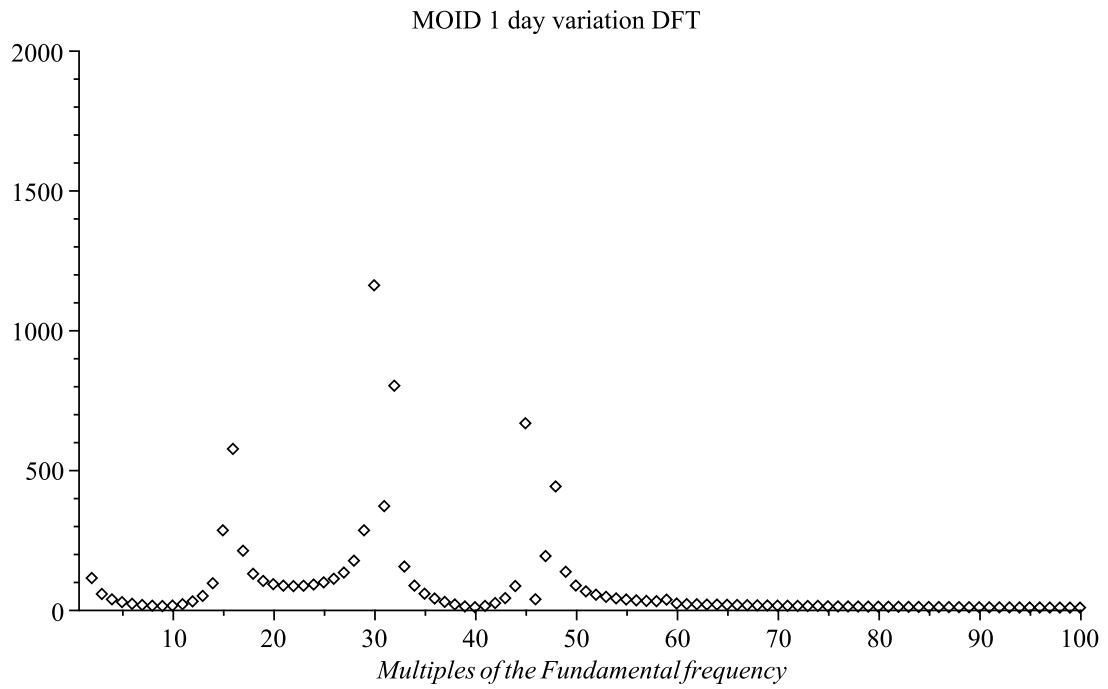


Figure 5.5: Cosmos 2251 debris MOID to ISS evolution DFT.

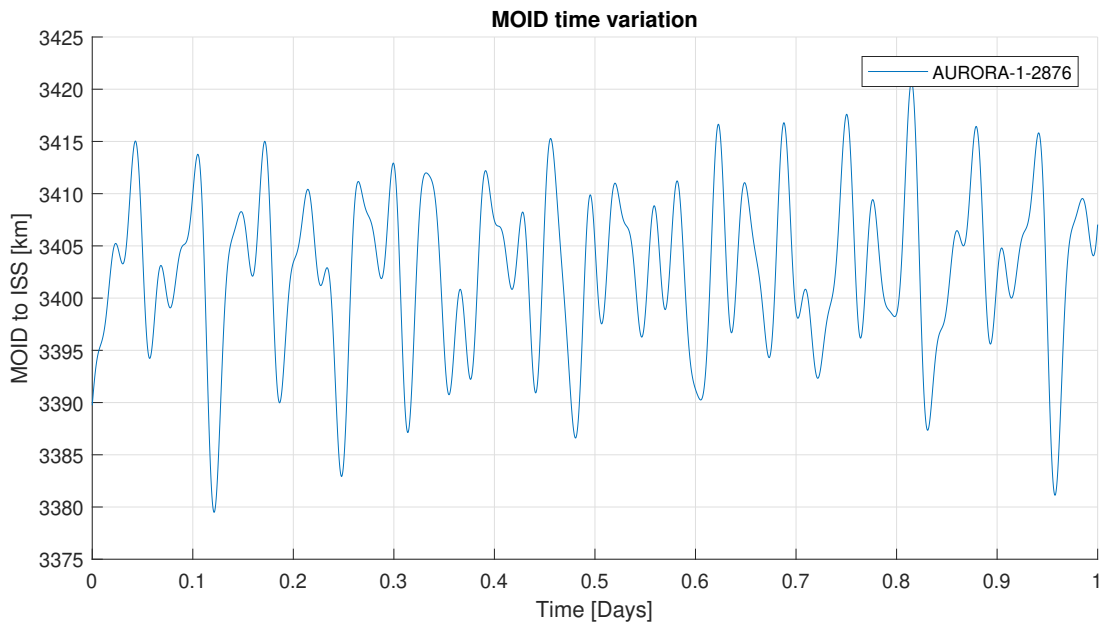


Figure 5.6: Aurora 1 MOID to ISS evolution during 1 day.

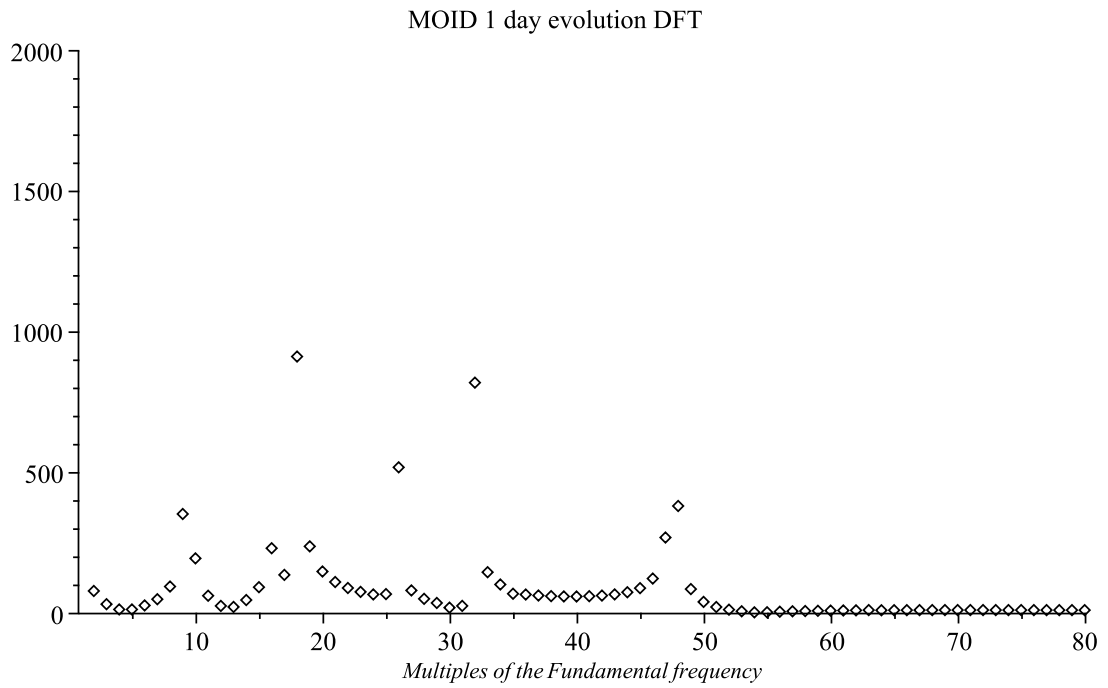


Figure 5.7: Aurora 1 MOID to ISS evolution DFT.

Breeze M debris

The Breeze M debris (NORAD Catalog Number: 35546) belonged to the Briz-M Russian liquid-propellant rocket orbit insertion upper stage (Briz-M is the Russian name). It has almost the same inclination as the ISS but its orbit is more elliptical ($e = 0.2624037$). It makes 9.27 revolutions per day. The ISS and the Briz-M debris have been propagated for one day at 1 s sampling interval.

In this case, the analysis of the MOID evolution over only one day suggests that, again, the debris does not constitute a threat in the studied period. The MOID is above 1000 km and it evolves in an overall rapid increase during the day; a following MOID diminution is highly probable (Fig. 5.8).

The frequency analysis (Fig. 5.9) shows the three peaks which have been previously associated to the ISS orbital motion. They are the 16, 32 and 48 peaks, corresponding to the first, second and third harmonics. For the Briz-M debris, some peaks can be deduced amongst the graphic *noise*. The not very visible peak corresponding to 10 can be associated with the fundamental frequency. In this case, more peaks can be observed: the 19 peak corresponding to the second harmonic, the 29 and 38 peaks corresponding to the third and fourth harmonics and perhaps a fifth harmonic evidence in the 47 peak, although this last case is most likely associated to the ISS third harmonic. After that, the *noise* does not allow further observations.

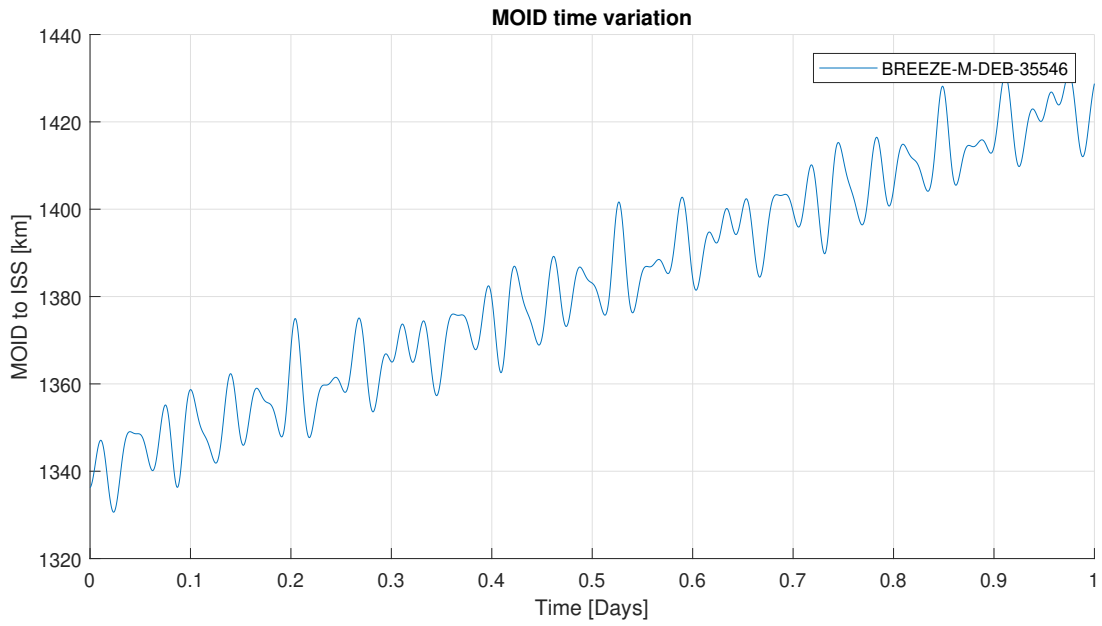


Figure 5.8: Breeze M debris MOID to ISS evolution during 1 day.

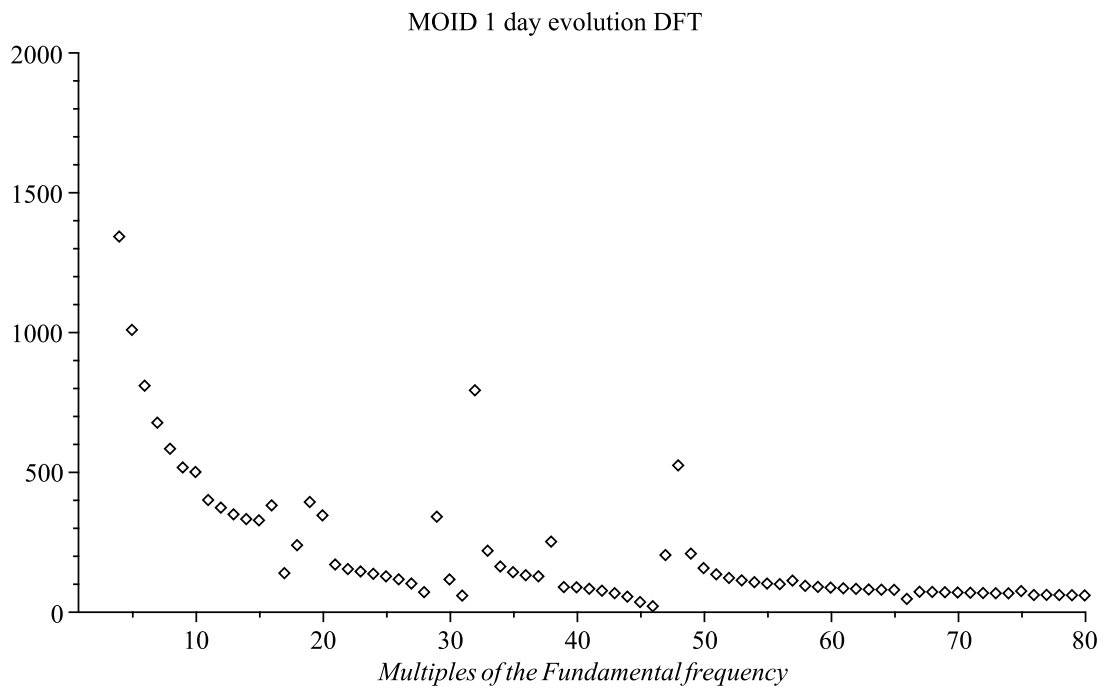


Figure 5.9: Breeze M debris MOID to ISS evolution DFT.

Fengyun 1C debris

A debris from the 2007 Chinese ASAT test against the Fengyun 1C satellite has been selected mainly because of its orbital period (NORAD Catalog Number: 33733). Being the inclination higher than 90° the debris has a retrograde motion. It has a low eccentricity and makes 14.05 revolutions per day. The example has been selected because of its similarity to the Cosmos 2251 debris in terms of eccentricity and orbital period. The ISS and the Fengyun 1C debris have been propagated for one day at 1 s sampling interval.

As can be observed in Fig. 5.10, the MOID evolution has a more *ordered* pattern and the variation spans a range of almost 50 km. In the considered period, the MOID does not appear to go below 400 km. This case presents a very curious behaviour: the MOID variation in some cases does not appear as smooth as the other examples. There are many cusp points, especially visible in the correspondence of some local maxima.

The DFT shows interesting results (Fig. 5.11). The ISS frequencies are not easy to identify. From the previous examples experience it can be deduced that the 32 and 48 peaks correspond to the second and third harmonics. There is not a clear evidence of the fundamental frequency.

In the case of the Fengyun 1C debris instead, there are at least five peaks which can be associated to multiples of the fundamental frequency. The first peak at 15 is interpreted as the fundamental frequency; the second peak at 29 represents the second harmonic and it seems to be very relevant in its contribution to the frequency spectrum; the 43, 57 and 71 peaks are interpreted as the third, fourth and fifth harmonics.

Globalstar M046

The Globalstar M046 satellite (NORAD Catalog Number: 25651) from the satellite phone service Globalstar constellation has also been selected because of its orbital period. It has a very circular orbit at an altitude of almost 1650 km. It orbits the Earth at 12 revolutions per day in a 52° inclined orbit. It has been propagated along with the ISS for one day at 1 s sampling interval.

The MOID evolution shows an expected result (Fig. 5.12). It maintains its value above 1200 km in the considered period, hence, the satellite does not constitute a hazard for the ISS. Its variation spans almost a 50 km range.

From the DFT analysis (Fig. 5.13), in the case of Globalstar satellite, three multiples of the fundamental frequency can be clearly observed. The 13 peak corresponds to the fundamental frequency while the 25 and 37 peaks correspond to the second and third harmonics respectively.

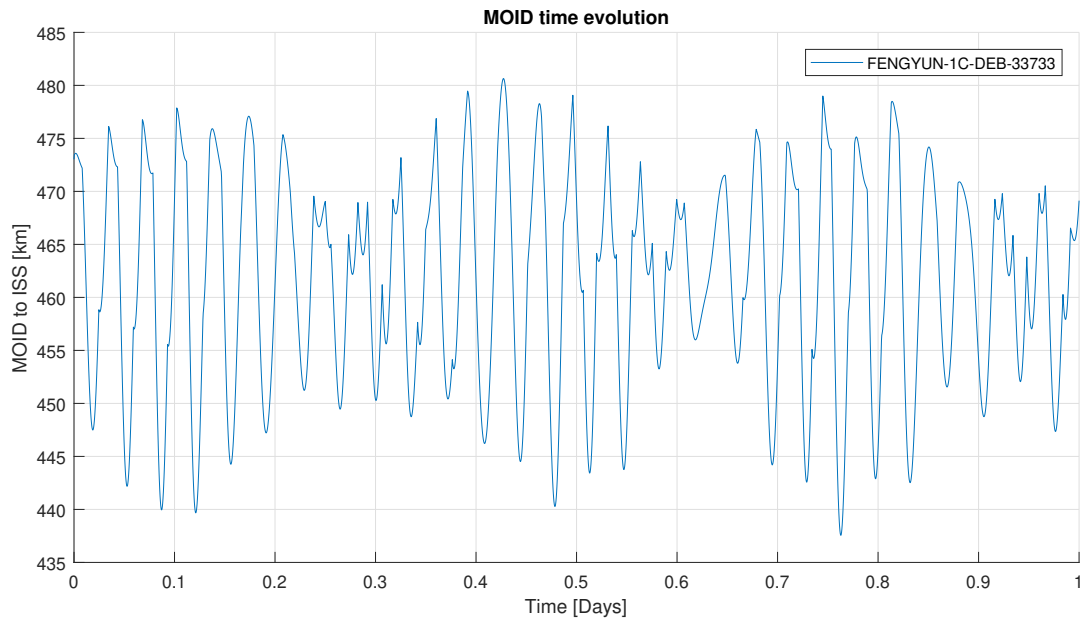


Figure 5.10: Fengyun 1C debris MOID to ISS evolution during 1 day.

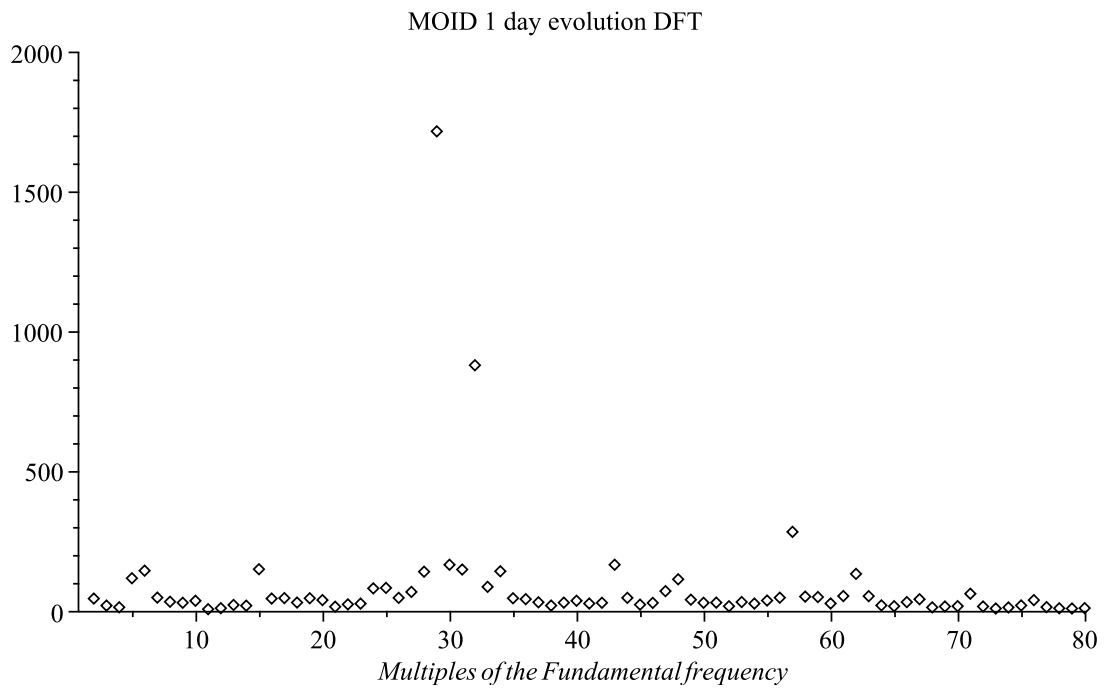


Figure 5.11: Fengyun 1C debris MOID to ISS evolution DFT.

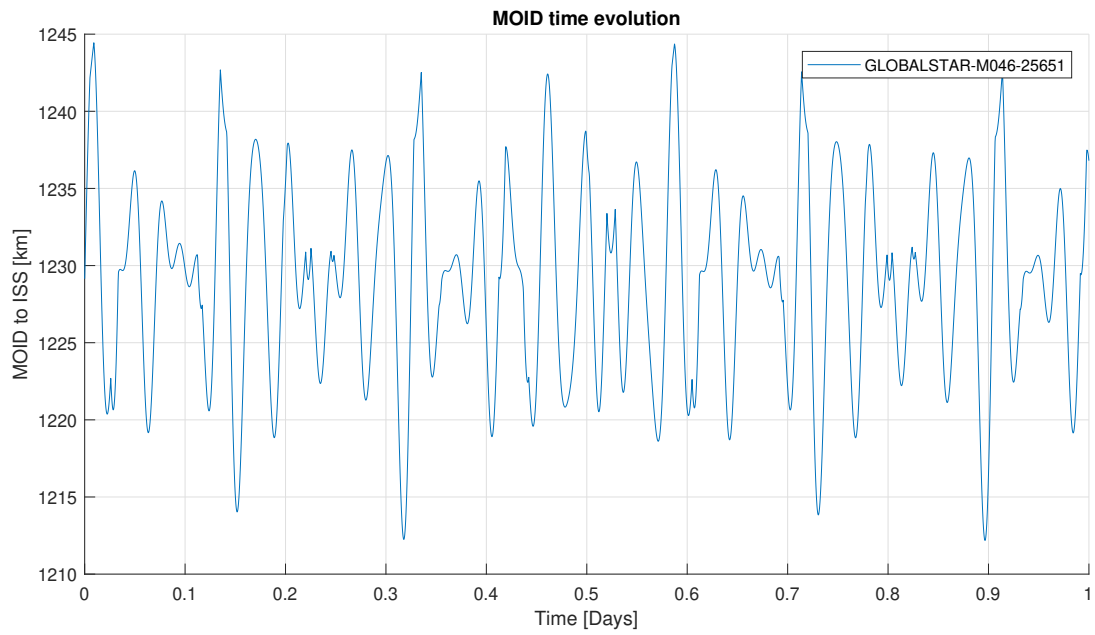


Figure 5.12: Globalstar M046 MOID to ISS evolution during 1 day.

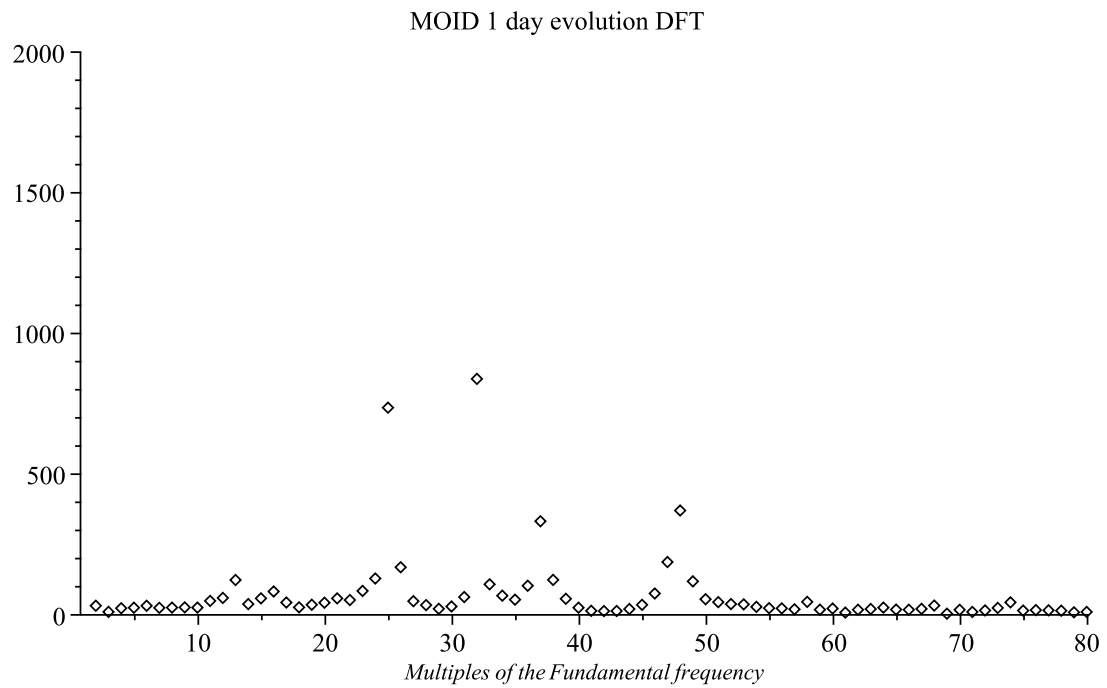


Figure 5.13: Globalstar MOID to ISS evolution DFT.

5.3 Long term analysis

For the long term analysis, some objects shall be taken as examples to study their ISS MOID over a larger period. The analysis looks for specific patterns in the long term period, in order to understand possible periodic or quasi-periodic behaviours and discover possible hazardous situations repetitions. As in the example of Fig. 5.1, the starting point of the propagation is 58402.000 MJD. The considered TLEs are hereby presented:

```
ISS (ZARYA)
1 25544U 98067A 18283.21590318 .00001824 00000-0 35183-4 0 9990
2 25544 51.6419 165.4892 0003533 264.2491 242.0238 15.53798400136402
COSMOS 2251 DEB
1 34909U 93036ADE 18283.15415979 .00000295 00000-0 57285-4 0 9996
2 34909 74.0161 105.9568 0105857 179.6894 180.4360 14.64503102509204
BREEZE-M DEB
1 35546U 06006CP 18282.11456277 .00004477 00000-0 96335-2 0 9999
2 35546 51.2368 245.7644 2624037 129.9059 256.3566 9.27265999231244
ARIANE 5 DEB (SYLDA)
1 42953U 17059D 18282.75174361 .00017498 00000-0 32072-2 0 9995
2 42953 6.4751 0.7883 7026250 144.2971 294.2329 2.61492641 8974
FALCON 9 R/B
1 40108U 14046B 18283.05502860 .00033212 -34253-6 67240-3 0 9993
2 40108 23.9685 198.3530 6461274 95.9211 335.6856 3.44403125 43801
```

Figure 5.14: Considered TLEs for the long term analysis.

Cosmos 2251 debris

The debris from the Iridium-Cosmos collision of 2009 used in the short term analysis has been considered. It has been selected to have a consistent comparison study. The ISS and the object have been propagated for 1250 days at 6 hours sampling interval with the same starting point of the short term propagation.

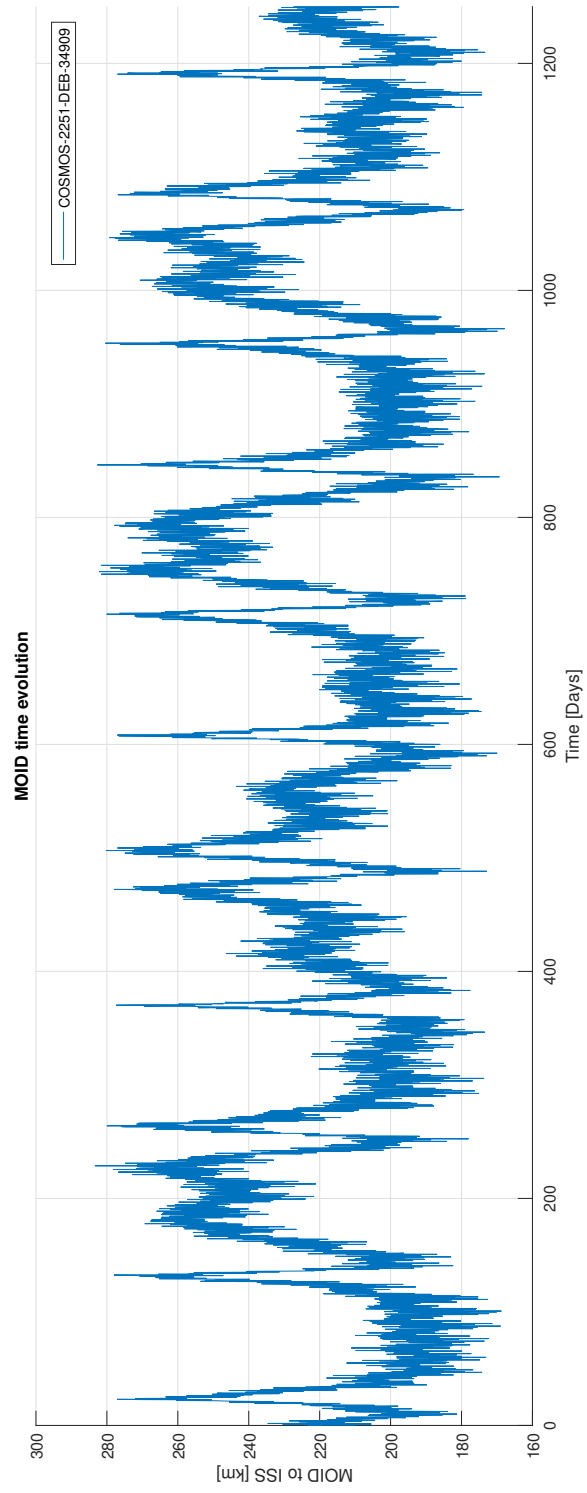


Figure 5.15: Cosmos 2251 MOID to ISS evolution over 1250 days.

It can be observed in this example that the MOID presents high variability. Its minimum is near to 170 km while its maximum is higher than 280 km, and they gather in time intervals which in some cases are less than 50 days.

The MOID variation over time presents some periodicities. The first and most noticeable *period*, although it is not a proper one, is the shorter one, confined in the region between two *peaks* of the MOID. Looking for a repetitive pattern, it can be deduced that after seven *short periods* there is a clear repetition of the same behaviour (it is easy to see the same peaks and valleys repetition in exactly the same order). In this case the second and larger period clearly presents a repetitive pattern¹³. Its duration is between 800 and 850 days and as said, it embraces seven shorter repetitions of more than 100 days each.

Some explications for this behaviour can be deduced from the analysis of the two objects' orbital parameters. Considering the mean orbital elements as presented in the TLE set (Fig. 5.14), a simple analysis can be done.

The Earth parameters used in the calculation are:

$$\begin{aligned}\mu_{\oplus} &= 398\,600.4415 \text{ km}^2 \text{ s}^{-1} \\ J_2 &= 1.082\,626\,683\,55 \times 10^{-3} \\ R_{\oplus} &= 6378.1363 \text{ km}\end{aligned}\tag{5.1}$$

For the ISS:

$$\begin{aligned}i_1 &= 51.6419^\circ = 0.901\,32 \text{ rad} \\ e_1 &= 1.824 \times 10^{-5} \\ n_1 &= 15.53798 \text{ rev d}^{-1}\end{aligned}\tag{5.2}$$

The ISS orbital angular velocity around the Earth and its period are thus obtained (the geocentric inertial reference is hereinafter indicated with the 0 subscript):

$$\begin{aligned}\omega_{10} &= 1.129\,95 \times 10^{-3} \text{ rad s}^{-1} \\ T_{10} &= 92.676 \text{ min}\end{aligned}\tag{5.3}$$

One of the mayor effects of the Earth's oblateness is that the bulge of the equator generates a gravitational force on the satellite which is not directed towards the Earth's centre. This effect creates a torque on the satellite's orbit which induces a gyroscopic precession of it. The direction of precession is opposite to the direction of revolution. For this reason, the node precession for prograde orbits is also called *node regression*. The precession rate of the ascending node depends on the orbital eccentricity as well as the inclination of the orbital plane relative to the equatorial plane¹⁴. It can be computed with the following expression:

$$\dot{\Omega}_{10} = \frac{d\Omega_{10}}{dt} = -\frac{3}{2}J_2 \cos i_1 \left(\frac{R_{\oplus}}{p_1}\right)^2 n_1 = -1.384\,21 \times 10^{-2} \text{ rev d}^{-1}\tag{5.4}$$

¹³The function does not repeat perfectly as a real periodic function, but in the limit of this analysis, the two objects orbits follow the same evolution, creating a repetitive pattern. Given this premise, the MOID evolution can be considered as *periodic*

¹⁴This fact is wisely exploited for *Heliosynchronous orbits*. The J_2 effect on the node precession is adjusted with the correct selection of the orbit eccentricity and inclination in order to make the orbital plane precess at the same rate of the Earth's revolution around the Sun. The result is an orbital plane which maintains a nearly constant angle relative to the Sun direction.

where:

$$p_1 = a_1(1 - e_1^2) = 6783.784779 \text{ km}, \quad a_1 = \sqrt[3]{\frac{\mu_{\oplus}}{\omega_{10}^2}} = 6783.784781 \text{ km} \quad (5.5)$$

are respectively the semilatus rectum and the semi-major axis of the orbit.

For Cosmos 2251 debris:

$$\begin{aligned} i_2 &= 74.0161^\circ = 1.29182 \text{ rad} \\ e_2 &= 2.95 \times 10^{-6} \\ n_2 &= 14.64503 \text{ rev d}^{-1} \\ \omega_{20} &= 1.06502 \times 10^{-3} \text{ rad s}^{-1} \\ T_{20} &= 98.32687 \text{ min} \end{aligned} \quad (5.6)$$

Thus, the ascending node regression rate is:

$$\dot{\Omega}_{20} = \frac{d\Omega_{20}}{dt} = -5.34987 \times 10^{-3} \text{ rev d}^{-1} \quad (5.7)$$

The differential node precession rate $\dot{\Omega}_{21}$ of the debris respect to the ISS (considering the ISS orbit fixed in space and accounting for the relative precession rate of Cosmos ascending node respect to it) is easily obtained:

$$\dot{\Omega}_{21} = \dot{\Omega}_{20} - \dot{\Omega}_{10} = 5.33582 \times 10^{-2} \text{ rev d}^{-1} \quad (5.8)$$

which corresponds to a relative precession period of:

$$T_{21} = 117.75472 \text{ d rev}^{-1}. \quad (5.9)$$

This means that, neglecting other perturbations, after a period of almost 118 days the two orbital planes return in the same relative position. It perfectly fits the results found when considering the MOID variation over time. There is a period of 118 days which repeats over time and which is directly attributable to the relative node precession of the two orbits. The fit is very accurate, the proof of it is the fact that $7 \times T_{21} \simeq 824$ days which is approximately the duration of the larger period in Fig. 5.15.

Breeze M debris

The Breeze M debris considered in the short term analysis has been also considered for a longer propagation. It has been selected observing its ISS MOID evolution during one day, which supposed a secular increase. Further analysis was needed to understand the overall behaviour. The ISS and the debris have been propagated for 1250 days at 6 hours sampling interval.

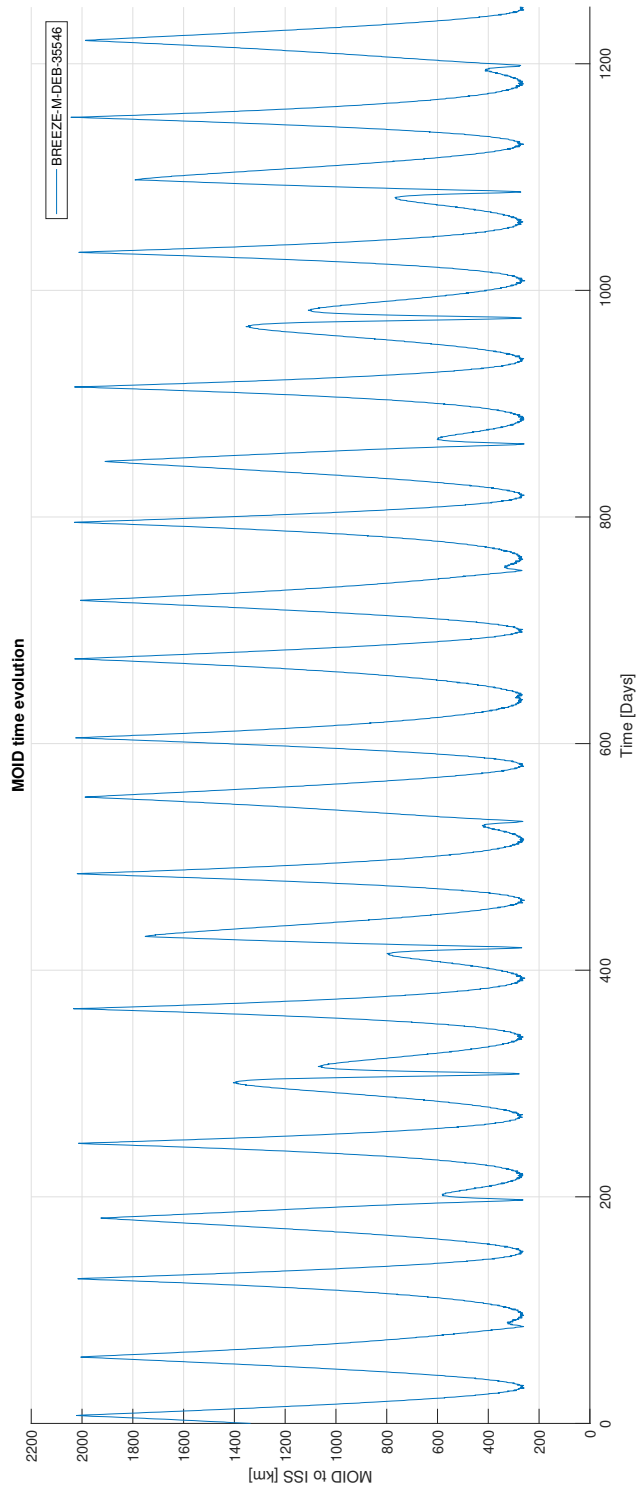


Figure 5.16: Breeze M debris MOID to ISS evolution over 1250 days.

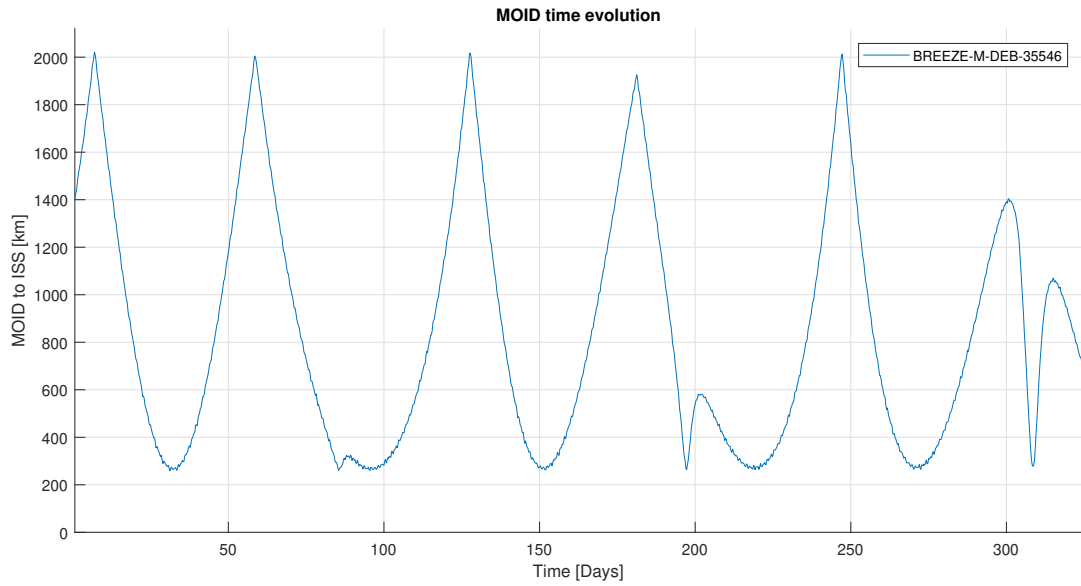


Figure 5.17: Breeze M debris MOID to ISS evolution during the first 300 days.

In this case, one of the most visible differences is the fact that the MOID evolution in the long period is much less *curly* than the one of the Cosmos 2251 debris. There are some *periodic* (in the sense of *not secular*) variations especially in correspondence of the lower values, as illustrated in Fig. 5.17 which is a zoom of the first 300 days evolution.

The two cases are very different for several reasons. The Breeze M debris orbit is not quasi-circular with a semi-major axis $a_3 = 9570.448$ km. There is evidence of a MOID spanning a higher range of distances: the maximum value is higher than 2000 km while the minimum value is of 256.1 km. The evolution is constituted by more *regular* periods which are interrupted by some not-sinusoid like behaviour. There is an identifiable pattern which in this case has been easily measured. The pattern duration is of about 667 days and like in the previous case this is due to the differential node precession rate between the Breeze M debris and the ISS.

From the Breeze M debris TLE the following values can be obtained:

$$\begin{aligned}
 i_3 &= 51.2368^\circ = 0.89452 \text{ rad} \\
 e_3 &= 0.2624 \\
 n_3 &= 9.27266 \text{ rev d}^{-1} \\
 \omega_{30} &= 6.7433 \times 10^{-4} \text{ rad s}^{-1} \\
 T_{30} &= 155.295 \text{ min}
 \end{aligned} \tag{5.10}$$

Thus, the ascending node regression rate of the Breeze M debris is:

$$\dot{\Omega}_{30} = \frac{d\Omega_{30}}{dt} = -4.82958 \times 10^{-3} \text{ rev d}^{-1} \tag{5.11}$$

The differential node precession rate $\dot{\Omega}_{31}$ of the debris respect to the ISS is:

$$\dot{\Omega}_{31} = \dot{\Omega}_{30} - \dot{\Omega}_{10} = 9.01252 \times 10^{-3} \text{ rev d}^{-1} \tag{5.12}$$

which corresponds to a relative precession period of:

$$T_{31} = 110.956\,71 \text{ d rev}^{-1}. \quad (5.13)$$

In the previous example (Cosmos 2251 debris), it was found that the period T_{21} perfectly fitted an evident low order period of the MOID evolution graphic. In the case of the Breeze M debris, unlike the previous one, there is not direct evidence of a lower order period in the graphic which perfectly fits the result. Nevertheless, it is interesting to notice that the observed pattern period is 667 days long. This value is nearly six times the T_{31} period already obtained ($6 \times T_{31} = 665.74$). From this observation, it can be deduced that the 667 days period is again a multiple of the ascending node differential precession period.

Ariane 5 SYLDA adapter

One Ariane 5 SYLDA adapter¹⁵ (NORAD Catalog Number: 42953) has been selected to be another example for long term MOID behaviour analysis. Deployment adapters are an undesired *collateral* effect of multiple launches. They are indispensable for correctly deploy more than one satellite, but the obvious consequence is that their orbits share a lot of common features with the orbits of the deployed bodies (they remain almost in the same orbital zone of the deployed satellites). It means that like orbital injection upper stages, they tend to rest in orbit for very long time (i.e. they are not designed for a rapid atmospheric re-entry). They are big orbital debris which can constitute a big threat active spacecraft.

The orbit of SYLDA presents high eccentricity ($e_4 = 0.7026$), with an inclination of 6.475° . The low inclination makes it nearly an equatorial orbit. The debris has been propagated along with the ISS for 1250 days at 6 hours sampling interval (Fig. 5.18).

¹⁵SYLDA (French: *SYstème de Lancement Double Ariane*) deployed the Intelsat 37E and BSAT-4A satellites, launched on the 29th of September, 2017.

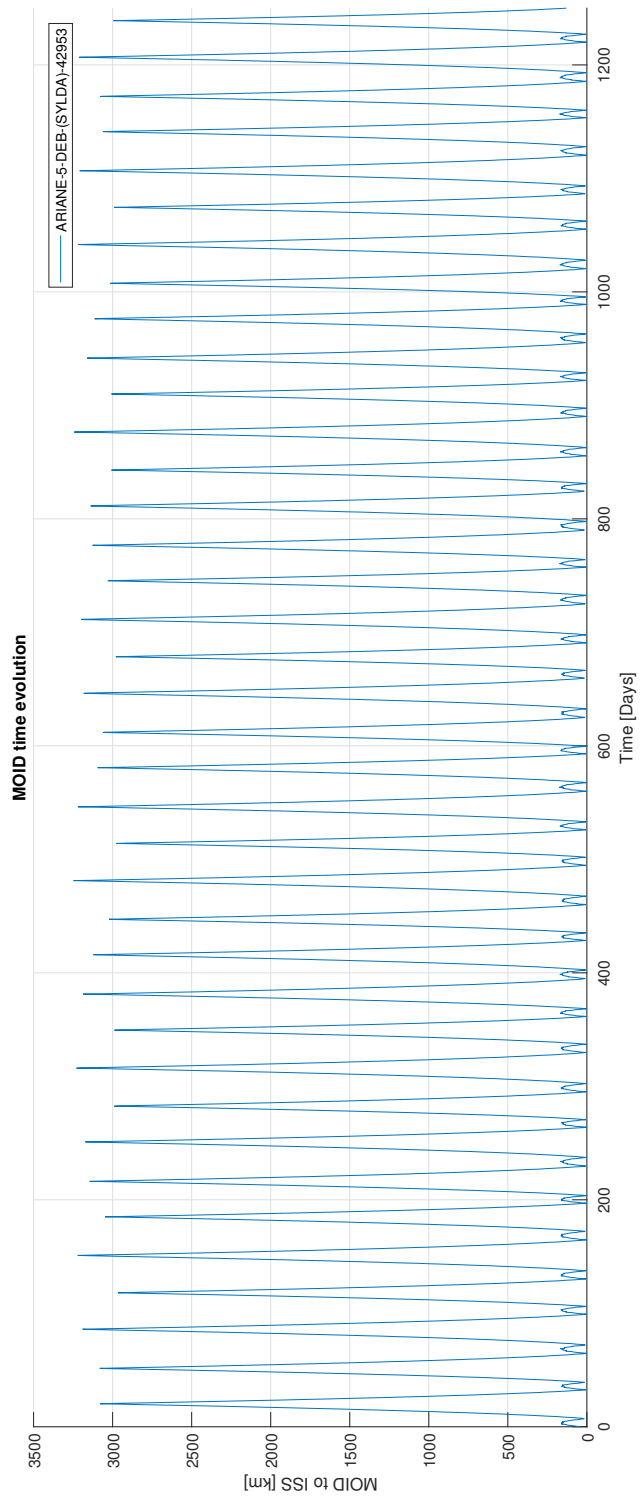


Figure 5.18: SYLDA MOID to ISS evolution over 1250 days.

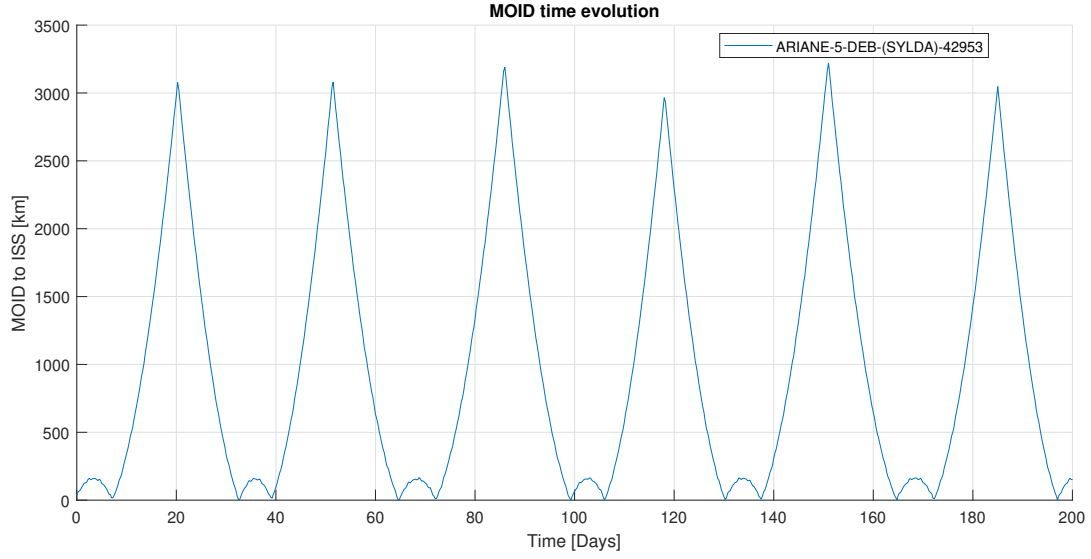


Figure 5.19: SYLDA MOID to ISS evolution during the first 200 days.

In the case of SYLDA, the MOID evolution graphics show a very ordinate, periodic behaviour (Fig. 5.19). Again, as in the case of Breeze, SYLDA (whose orbit semi-major axis is $a_4 = 22\,255$ km) presents a high variability in the MOID values, they span a range of almost 3300 km. Although there is evidence of a period of almost 33 days (the time interval between two main peaks has a mean value of 32.97 days) it is observed that the peaks do not repeat equally. Thus, the study focused on the individuation of a higher period pattern which repeated exactly the same. The identification is not easy, but carefully observing, there is a periodic pattern which repeats nearly every 561 days. It involves 17 33-days MOID *oscillations* as previously defined.

Also in this case, this pattern can be associated with the differential node precession rate between SYLDA and the ISS. In fact, from the SYLDA TLE the following values are obtained:

$$\begin{aligned}
 i_4 &= 6.4751^\circ = 0.113\,01 \text{ rad} \\
 e_4 &= 0.702\,63 \\
 n_4 &= 2.614\,93 \text{ rev d}^{-1} \\
 \omega_{40} &= 1.902 \times 10^{-4} \text{ rad s}^{-1} \\
 T_{40} &= 550.685 \text{ min}
 \end{aligned} \tag{5.14}$$

Thus, the ascending node regression rate of SYLDA is:

$$\dot{\Omega}_{40} = \frac{d\Omega_{40}}{dt} = -1.351\,86 \times 10^{-3} \text{ rev d}^{-1} \tag{5.15}$$

The differential node precession rate $\dot{\Omega}_{41}$ of the debris respect to the ISS is:

$$\dot{\Omega}_{41} = \dot{\Omega}_{40} - \dot{\Omega}_{10} = 1.249\,02 \times 10^{-2} \text{ rev d}^{-1} \tag{5.16}$$

which corresponds to a relative precession period of:

$$T_{41} = 80.062\,53\text{ d rev}^{-1}. \quad (5.17)$$

The two orbital planes return at almost the same relative position after 561 days. Observing this high order period with the calculated period of relative nodal regression, it is noticed that 561 days correspond to almost 7 times the period T_{41} obtained before ($7 \times T_{41} = 561.45$). Again, the observed pattern period is a multiple of the node regression rate between the SYLDA and the ISS orbits.

Continuing the MOID evolution analysis, there is another interesting feature to point out. The MOID between the SYLDA and the ISS orbits has periodic minima which are lower than 10 km (Fig. 5.20). This constitutes a threat to the ISS and, in this case, the object should be further analysed.

Moreover, observing Fig. 5.19, there are intermediate lower peaks between two higher peaks. They seem to be the *negative* continuations of the MOID function whose sign has been changed. It is consistent with the MOID computation algorithm: the MOID cannot take negative values (a negative distance does not make any sense). During the computation process, the two orbits pass somehow from a configuration to the opposite. During this operation, two minima are recorded, and they correspond to the two central minima of the lower order period of 33 days.

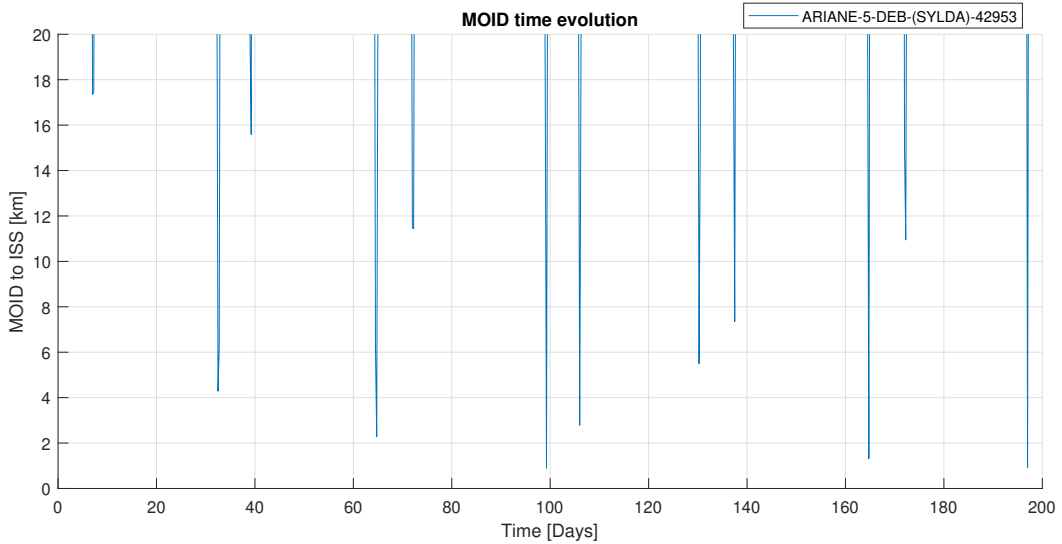


Figure 5.20: Detailed view of SYLDA MOID to ISS evolution in 200 days for lower MOID values.

Falcon 9 Rocket Booster

In order to better analyse the long term MOID variation on very eccentric orbits, a Falcon 9 Rocket Booster (NORAD catalog number: 40108) has been selected because of its characteristics. It has an eccentricity $e_5 = 0.6461$ and an inclination $i_5 = 23.9685^\circ$. It has been propagated along with the ISS for 600 days at 6 hours sampling rate.

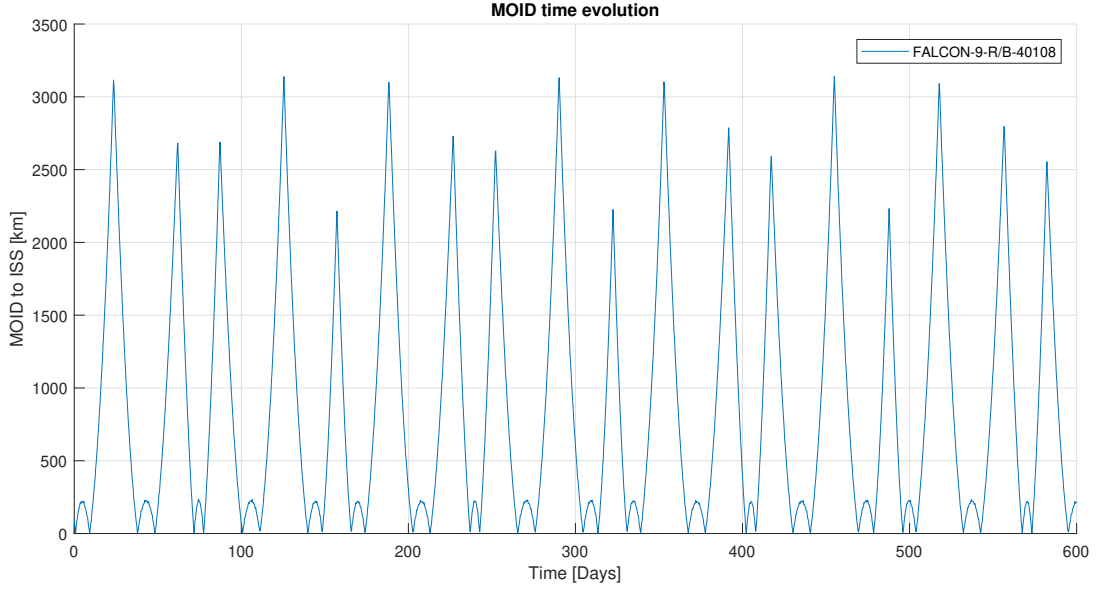


Figure 5.21: Falcon 9 Rocket Booster MOID to ISS evolution over 600 days.

The graphic shows a similar behaviour respect to the SYLDA MOID evolution: the MOID spans a high range of distances, the maximum values being over 3000 km while the minimum values approach zero.

It seems that for very eccentric orbits the MOID variability is higher than the one observed in the case of quasi-circular orbits. This trend is confirmed in the last three examples. Moreover, for the SYLDA adapter ($e_4 = 0.7026$, $a_4 = 22\,255$ km,) and the Falcon 9 Rocket Booster ($e_5 = 0.6461$, $a_5 = 18\,522$ km) the variability range is higher than the Breeze M debris ($e_3 = 0.2624$, $a_3 = 9\,570$ km) variability range.

Continuing the analysis of Fig. 5.21, there is a clear period of nearly 33 days (32.957 d) which repeats constantly although the peaks does not reach the same value. A high order pattern involving five 33 days periods can be observed. It has a mean period of about 165 days.

Considering the orbital values which appear in the Falcon 9 TLE, the ascending node regression rate is:

$$\dot{\Omega}_{50} = \frac{d\Omega_{50}}{dt} = -1.785\,91 \times 10^{-3} \text{ rev d}^{-1} \quad (5.18)$$

Which gives a differential node precession rate $\dot{\Omega}_{51}$ respect to the ISS:

$$\dot{\Omega}_{51} = \dot{\Omega}_{50} - \dot{\Omega}_{10} = 7.575\,129 \times 10^{-2} \text{ rev d}^{-1} \quad (5.19)$$

and this corresponds to a relative precession period:

$$T_{51} = 82.95 \text{ d rev}^{-1}. \quad (5.20)$$

It can be observed that the high order period of about 165 days is twice as large as the T_{51} period ($2 \times T_{51} = 165.89$). Again, it results that the observed pattern period corresponds to a

multiple of the ascending node differential precession rate.

Finally, as in the SYLDA example, it has to be highlighted the fact that the Falcon 9 R/B ISS MOID reaches values very close to 0. Again, in this example MOID *inversions* can be seen, i.e. the MOID function seems to present the *negative* values symmetrically transformed respect to the x axis in the positive semi-plane.

5.4 Real time monitoring

One of the advantages of the tool is the possibility of a fast and nearly real time threats assessment. Because of its speed in fact, the tool can process a large quantity of space debris against a common primary. This means that the second filter proposed by Hoots [8] can be applied to almost all the space debris which endanger a spacecraft. This is a benefit in terms of the orbit planners risk assessment capacity.

In order to put into practice the MOID evolution filter to assess a spacecraft threats, the steps could be the following:

1. Select the spacecraft whose threats shall be analysed, i.e., the spacecraft against which all the other space objects will be compared. This will be the primary spacecraft.
2. Select the TLEs which can endanger the primary spacecraft. If the analysis is conducted for the first time, it could be ran on all the TLEs database in order to understand which classes of debris are more dangerous (for instance, it could be found out that some debris clusters do not constitute a danger for the primary). Another option is to run the analysis only on those objects which have firstly passed by the first filter proposed by Hoots (the Apogee-Perigee filter).
3. The analysis is ran for a specified period (a two week period for instance), in order to understand the MOID evolution of all the considered objects. The number of MOID samples in the selected period does not need to be very dense because further analysis will be done on potential threats.
4. Based on the MOID behaviour in the selected period, the most *interesting* objects are selected (i.e., they pass the filter) for further and more detailed analysis. The selection criteria can be various: the potential threats can be selected based on the minimum MOID (all the objects whose minimum MOID is lower that a fixed threshold are selected); they can be selected based on MOID secular variation (if the MOID decreases secularly in the study period they are chosen for further analysis); finally, they can be selected by a combination of the two previous criteria.
5. This analysis can be ran every determined period (every one or two days, for instance) in order to update the situation with a new available database. The *refreshing* period is selected in function of the forecast period duration and the approximation which is needed for the analysis.

The process detailed above has been applied to the ISS, as an example to better visualise the work flow.

To understand the possible threats to the ISS in the immediate future, five groups of space debris are selected to be compared against it in order to find out potential hazardous situations.

The ISS MOID evolution of every one of the space debris will be displayed in a determined interval of time and further decision are proposed. The TLE data are made available in the Celestrak website already divided by debris group and are updated several times a day.

The analysis will embrace a period of 14 days starting from midnight, the 16th of June 2019 (58 650 MJD). The MOID sampling time is 1 hour.

Breeze M debris cloud

In the following graphic (Fig. 5.22), the MOID evolution of all the Breeze M debris to date still in space is displayed. After this example, all the graphics will present only the *significant cases*, it is, all the cases whose MOID is under a determined value. This is done for presentation purposes, in fact, it would be useless to plot hundreds of MOIDs evolutions if the values were always (during the considered period) higher than a *safe* value.

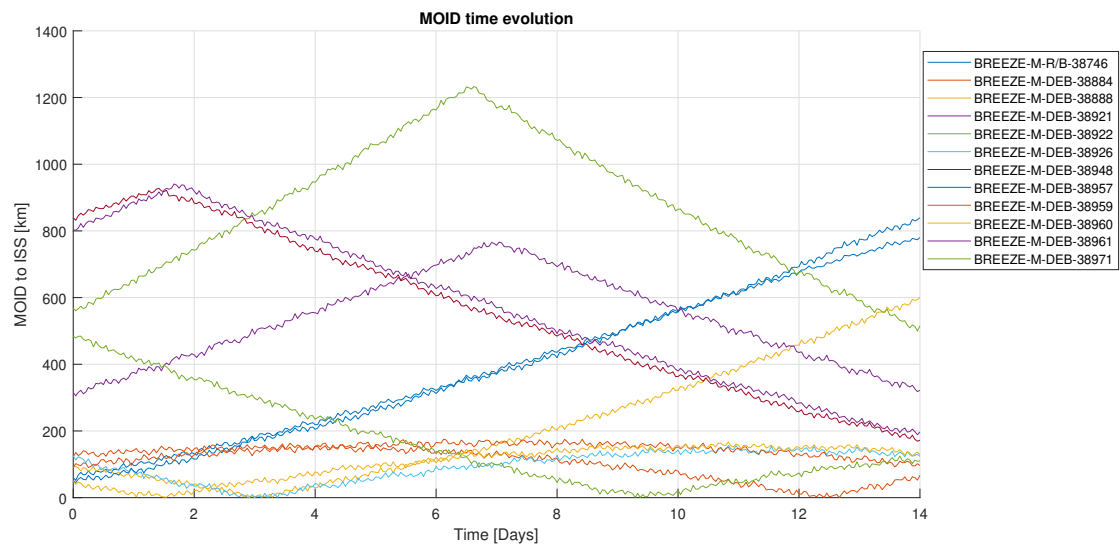


Figure 5.22: Breeze M debris cloud MOID to ISS analysis over 14 days.

For the purpose of this analysis, in order to make the examples clear, in Fig. 5.23 only MOIDs under 125 km are displayed.

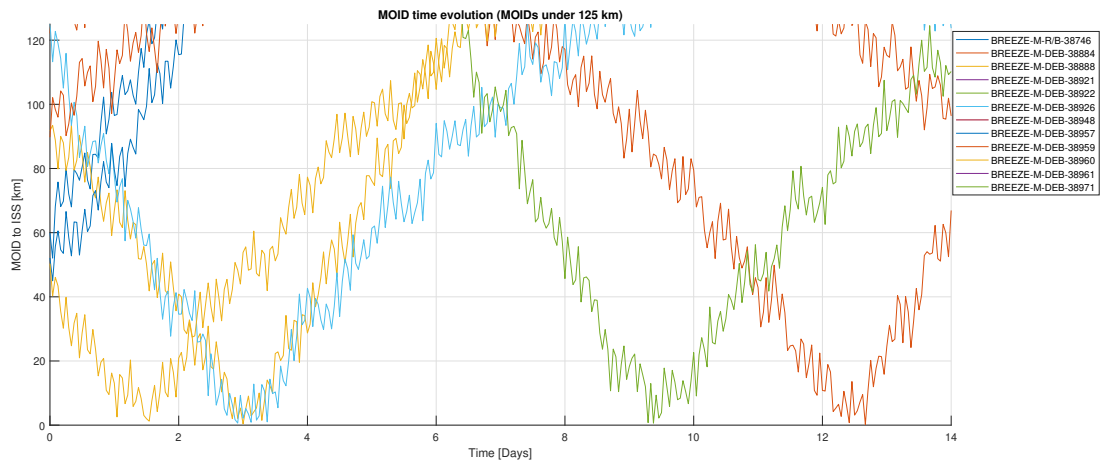


Figure 5.23: Breeze M debris cloud MOID to ISS analysis over 14 days (MOIDs under 125 km).

Iridium 33 debris cloud

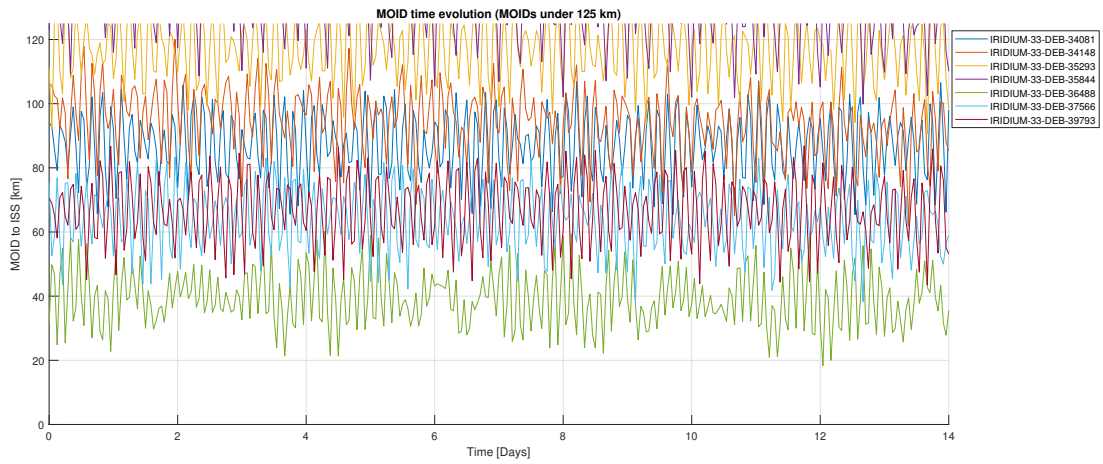


Figure 5.24: Iridium 33 debris cloud MOID to ISS analysis over 14 days (MOIDs under 125 km).

Cosmos 2251 debris cloud

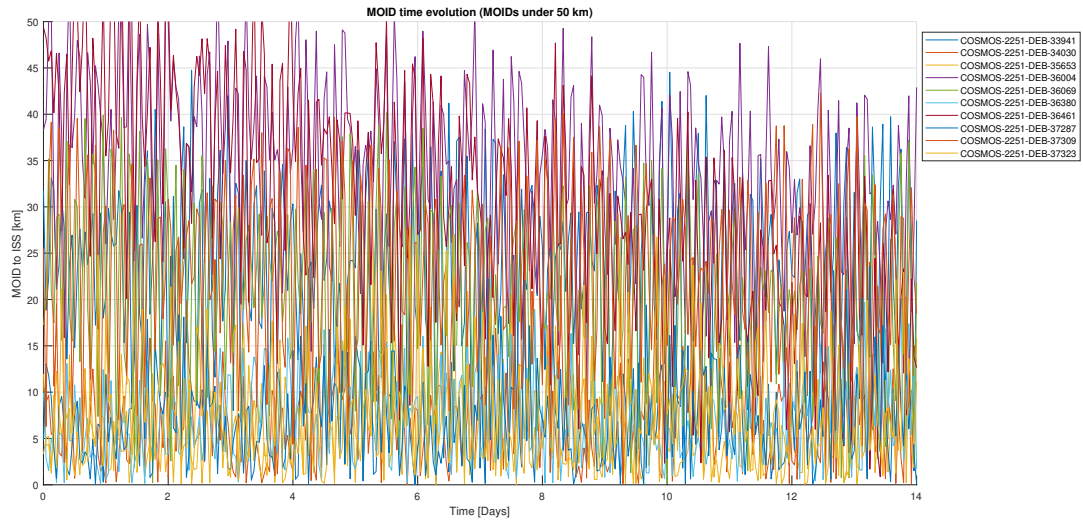


Figure 5.25: Cosmos 2251 debris cloud MOID to ISS analysis over 14 days (MOIDs under 50 km).

Fengyun 1C debris cloud

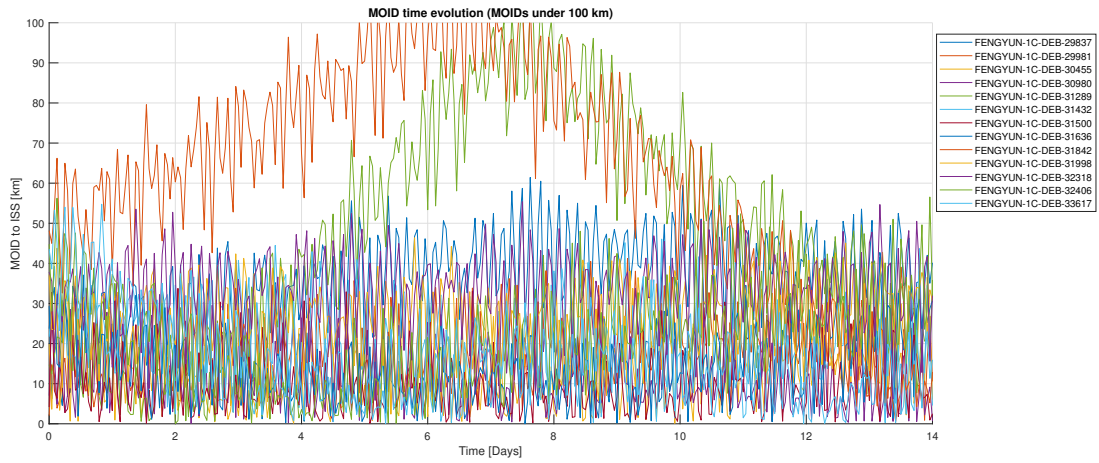


Figure 5.26: Fengyun 1C debris cloud MOID to ISS analysis over 14 days (MOIDs under 100 km).

Microsat R debris cloud (2019 Indian ASAT Test)

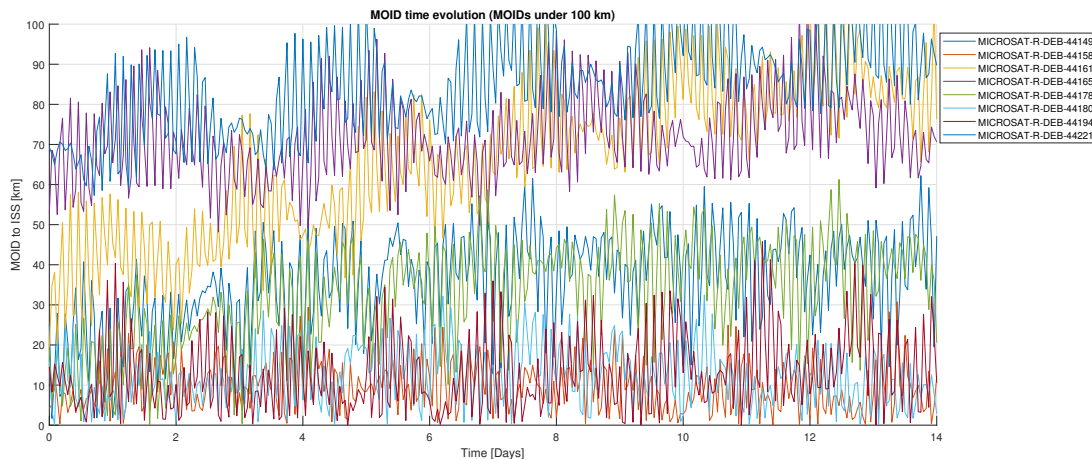


Figure 5.27: Microsat R debris cloud MOID to ISS analysis over 14 days (MOIDs under 100 km).

Given the MOID time evolution of five debris clouds respect to the ISS, the analysis can be carried out. As mentioned before, the data are not complete (the debris are actually more than the few ones displayed), only the lower MOIDs have been displayed. Even though, the graphics of above show interesting cases in which some debris could constitute hazard in the immediate future. Four out of five examples show some debris ISS MOIDs which assume dangerous values. In those cases, there are at least 3 objects per debris cloud whose ISS MOID almost becomes zero. Those cases would be selected for further analysis, i.e., they would pass the filter.

Collision risk assessment needs rapid filters in order to reduce rapidly and effectively the databases of dangerous objects. From this point of view, it is interesting to observe the computational time needed for these last analysis (Table 5). It is remembered that the propagation time is of 14 days at 1 hour sampling rate, obtaining 337 MOIDs per analysed object.

Table 5: 3812 debris propagation and MOID calculation computational time.

| Debris cloud | # obj | Prop. time [ms/obj] | MOID comp. t. [μ s/MOID] | t_{TOT} [s] |
|--------------|-------|---------------------|-------------------------------|---------------|
| Breeze M R/B | 12 | 1402.556 | 185 | 17.580 |
| Iridium 33 | 300 | 1761.689 | 247 | 553.524 |
| Cosmos 2251 | 1010 | 1706.420 | 226 | 1731.185 |
| Fengyun 1C | 2490 | 1643.058 | 190 | 4251.335 |
| Microsat R | 44 | 1746.437 | 211 | 79.974 |
| TOTAL | 3812 | | | 6633.598 |

The time needed to assess 3812 objects is of about $6634\text{ s} \approx 1\text{ h } 51\text{ min}$. Thus, the assessment of the most dangerous space debris clouds respect to the ISS took nearly 2 hours. The whole

NORAD SATCAT encompasses 44 336 publicly released objects¹⁶. Between them, 24 672 had already decayed, leaving 19 664 ephemerides still valid in the TLE data set. Given this quantity and the results of above, a rapid calculation can be made: it would take 34 222 s \approx 9.5 h to span all the TLE database for a 2 weeks propagation at 1 h sampling rate. This means that the calculation can be run on the whole available data set on a daily basis, leaving time for further data analysis.

5.5 Hazardous situations

In order to prove the validity of the tool against an already existing software, an example from the SOCRATES database has been selected.

The Satellite Orbital Conjunction Reports Assessing Threatening Encounters in Space (SO-CRATES) update the *Top 10 Conjunctions by Maximum Probability* and *Top 10 Conjunctions by Minimum Range* lists in order to warn orbital planners over the risk of close encounters in space. These two lists are available in the CelesTrak website. An example from the *Top 10 Conjunctions by Minimum Range* list has been selected in the CelesTrak website. This list presents 10 pairs of objects which from the STK/CAT software models are reported to come close within a week time. The list also presents the latest TLEs of all the presented pairs.

The chosen example is constituted by STEX (Space Technology EXperiments) satellite, an inactive space technology demonstrator, and a debris from CBERS 1 satellite which suffered a break up on the 18th of February 2007. The two objects were reported to have a close approach with a minimum range of about 0.638 km, expected by the 21st of June 2019, at 18:57:58.129 UTC (Fig. 5.28).

| Action | NORAD Catalog Number | Name | Days Since Epoch | Max Probability | Dilution Threshold (km) | Min Range (km) | Relative Velocity (km/sec) |
|----------|----------------------|-----------------|------------------|--------------------------|--------------------------|--------------------------|----------------------------|
| | | | | Start (UTC) | TCA (UTC) | Stop (UTC) | |
| Analysis | 25489 | STEX [-] | 6.508 | 1.000E+00 | 0.000 | 0.638 | 9.707 |
| | 35387 | CBERS 1 DEB [-] | 6.645 | 2019 Jun 21 18:57:57.618 | 2019 Jun 21 18:57:58.129 | 2019 Jun 21 18:57:58.640 | |

Figure 5.28: A pair of close encountering space objects as reported by SOCRATES.

The corresponding objects TLEs are presented for completeness:

```

STEX
1 25489U 98055A 19166.28218498 .00000086 00000-0 17306-4 0 9995
2 25489 84.9856 60.8335 0009471 169.8415 190.2980 14.48706984 92955
CBERS 1 DEB
1 35387U 990575S 19166.14569785 .00000541 00000-0 15430-3 0 9990
2 35387 98.4825 130.1300 0003444 149.7841 210.3552 14.49116830597434

```

Figure 5.29: TLEs of the two objects with high probability of collision.

The two objects have been propagated with the DROMOID tool in order to confirm its capability to detect close encounters in space. They have been propagated for 7 days at 1 minute sampling interval. The starting date is noon, 16th of June 2019 (58 650.5 MJD). The 1 week propagation time allows to include the 21th of June 2019 which is a date of particular interest, as the two objects are reported to get very close on that date.

¹⁶As of the 20th of June, 2019.

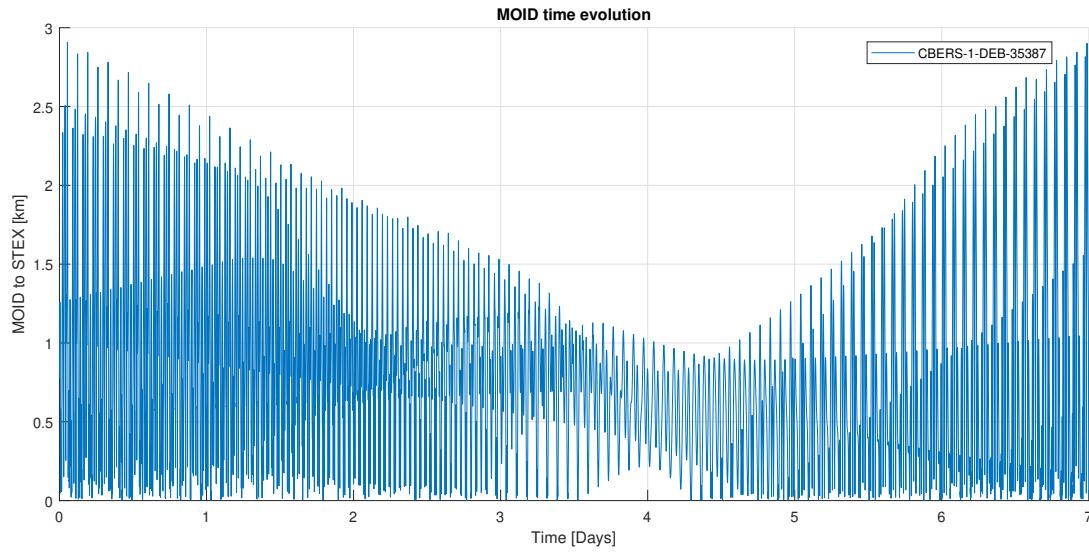


Figure 5.30: CBERS 1 DEB MOID to STEX evolution over 1 week since 2019, June the 16th 12:00.

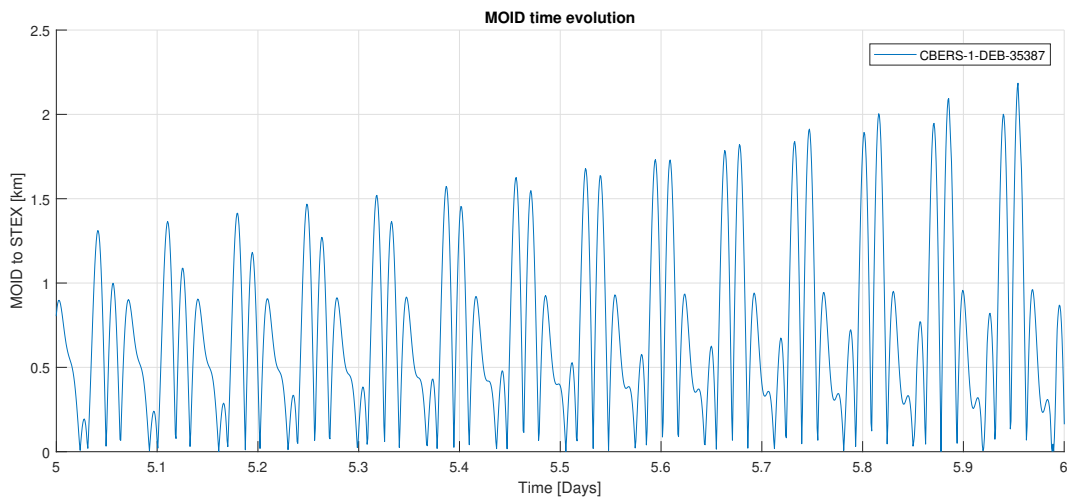


Figure 5.31: CBERS 1 DEB MOID to STEX evolution between day 5 and day 6 since 2019, June the 16th 12:00.

As can be seen in Fig. 5.30, the DROMOID tool gives a MOID evolution in the considered week which is quite clarifying. The MOID value between the two objects appears to be below 3 km during the whole week; moreover, it oscillates very fast between a maximum value of 3 km and the null value. The two orbits maintain a minimum distance for a long period. Given this orbits relative position, it means that the probability of the two objects to come very close and possibly collide is very high. In particular, it can be observed that the range of variability is even shorter (under 2 km) between approximately day 2 and 6 after the starting point. This can

be interpreted as an even higher probability of close encounter.

In Fig. 5.31 the MOID evolution between day 5 and day 6 is detailed because in this period SOCRATES forecasts the close encounter. It can be observed how the MOID oscillates and presents many peaks following one another. They can be interpreted (like in the case of SYLDA and Falcon 9 R/B propagation) as the *negative* parts of the function which have been transformed to the positive semi-plane. It could be explained with the fact that the two orbits are *crossing* each other many times at some point in the space.

Unfortunately the STEX satellite is inactive, thus making impossible to realise useful collision avoidance manoeuvres. In the case of a collision, SOCRATES shows a collision relative velocity of about 9.707 km s^{-1} . Such a violent impact would mean the formation of a dangerous cloud of hundreds (even thousands) of new space debris.

DROMOID tool shows similar results for the other cases from the same list as well. This is a further and very valuable confirmation of this method efficiency to detect hazardous situations.

6 Conclusions

The whole process of theoretical analysis and software development detailed in the present work has conducted to an operative tool for MOID evolution analysis. The DROMOID application allows to study the MOID evolution between any two selected objects from the TLEs database over the convenient period. The DROMOID development and the MOID evolution analysis lead to interesting results and reflections over them.

6.1 Software development

The DROMOID software development has constituted a considerable effort of theory implementation and code debugging. The complications raised during the development have been successfully overcome and many lessons have been learnt during the process. In particular, it is worth mentioning:

- The DROMOID tool allows to combine the power of two optimized tools for celestial mechanics applications. The propagator based on DROMO theory has been of fundamental importance because of its accuracy and speed. Its solid theoretical foundations make possible a rapid propagation which does not present singularities. This ensures that once the state vector is expressed in DROMO variables, the propagation is easily conducted. Nevertheless, is very important to carefully transform the state vector between different notation conventions. The MOID computation algorithm also ensures speed in the calculations. Once again, the strong theoretical foundations of the tool make it a strong and reliable calculator.
- The *modularity* of the DROMOID tool is very important. The integration between the two basic tools, as exhaustively described in this work, is done through an interfacing text file. This fact constitutes a big advantage: every time a new version of the DROMO propagator or the MOID calculator are available, they can be simply updated and integrated in the DROMOID tool. The only thing to care is the correct data interface between the tools. This reduces to the correct writing and reading of the interface file ensuring the fastest and most secure data flow. The *modularity* is an important advantage of the software.
- DROMOID allows to analyse a big database of space objects in near real time. One of the advantages of this tool is that it uses publicly available data for the propagation. The TLE database is used by NASA and it can be thus considered one of the most reliable sources of space debris ephemerides. Data can be downloaded at any time and the tool ensures a rapid propagation (depending on the refinement of the propagation tool and the propagation sampling, the whole TLE database can be analysed in a few hours time). The propagation is available for the desired period and sampling time.

6.2 MOID time evolution analysis

Once a rapid and reliable tool is set up, the MOID time evolution is made available for a big number of space objects and this constitutes a privileged and powerful analysis tool. Some important conclusions can be derived by its analysis:

- The MOID between two orbits evolves according to the evolution of the two object's very orbits. It is important to consider the different time scales at which the phenomena take place in order to make good predictions on future MOID behaviour.

- The short term MOID evolution is characterized by high variability and it seems to have a harmonic behaviour which rules the continuous variations in minutes and hours scale. There is evidence of the fact that the principal detected harmonics of MOID variation are due to the orbital periods of the considered objects. The revolutions per day of the objects in fact, determine the two first fundamental frequencies and the second and third harmonics as well. In the majority of the studied cases, there was no evidence of further harmonics nor their combinations. This result can be considered for instance when assessing the collision risk between spacecraft: similar configurations and hence similar risks can repeat in hours time thus highlighting the necessity of immediate actions to change orbital paths.
- The long term MOID evolution is characterized by some recognizable *periodicity* although not in the strict sense of the term. There is evidence of MOID evolution high order patterns which repeat almost in the same way over time. This effect has been correlated to the precession of the orbit ascending node in all the studied cases. There is evidence of a connection between the differential precession of the ascending nodes and the duration of the high order period. It manifests in the fact that the high order period duration is a multiple of the differential node precession rate. This result can be useful to orbit planners who can assess the collision risk before the mission start, thus allowing an appropriate and solid orbit design.
- The MOID evolution of thousands of objects can be used as an advanced application of the second filtering stage concept as proposed by Hoots. It is important to define the right criteria in order to properly create a filter which effectively discards the harmless space debris and only takes in consideration the hazardous cases. Two weeks time MOID evolution seems a reasonable time period over which extend the propagation. This allows to draw significant conclusions over MOID time evolution. Nevertheless, this filter must be repetitive over time. It means that it cannot be considered as an *exhaustive* filter over time. To work properly, it needs to be periodically run over the whole database of space debris because their orbital changes can affect significantly the future behaviour.
- The MOID evolution can be used simply to identify possible dangerous MOID minima. It means that what ultimately helps in the danger identification is the MOID instant value. If two orbits present a MOID evolution which at some time in the future present an unexpected dangerous minimum, this fact constitutes a sufficient proof for their further analysis.

6.3 Future development

The DROMOID tool, as every software, presents the possibility to be further developed. New functionalities and capabilities can be implemented and, as already said, the two constituting modules can be changed as well if a new version is available. Further development could be:

- To consider how the TLEs determination errors can propagate over time and how they affect the MOID computation accuracy. The TLEs database does not provide covariance matrix to understand their position and velocity errors. If new ephemerides (along with their covariance matrices) would be made available, an interesting improvement would be to compute the error evolution along with the corresponding object state vector evolution.
- To analyse all the possible pairs of objects within a TLE database. The work addresses to all the MOID variations between a studied object and the rest of objects present in the database. In order to look for all the possible collisions in space (including the collisions

between two debris, just for information and knowledge purposes) a sweep on all the database is necessary. It means that if a database presents N objects, $\frac{N(N-1)}{2}$ MOID evolution computations are necessary, thus increasing the number of computations of one order.

- To develop an analytical approximation of the DROMO derivatives in the case of the *main problem* to speed up the computation. In the simplification constituted by considering only the J_2 term, the DROMO theory can be approximated by an *Asymptotic solution* which can ensure a considerable time saving. This approximation has been investigated in [25] and there are evidences of one order computational time reduction respect to the DROMO propagator. The theory in [25] needs to be further revised and correctly set up, but it promises to be a powerful candidate to upgrade the propagation module. The basis of the *Asymptotic solution* theory are presented in Appendix B along with some methods comparison.

Appendix A Discrete Fourier Transform

A.1 Discrete Fourier Transform theory

The Discrete Fourier Transform (DFT) is the approximation of the continuous Fourier transform for functions known only at N instants separated by sample times Δt in the period T_1 ($N\Delta t = T_1$, the minimum frequency being $f_1 = \frac{1}{T_1}$), it is, when only a finite sequence of data is available.

Let $f(t)$ be the continuous time signal which is the source of the data. Its Fourier Transform would be:

$$F(\omega) = \int_{-\infty}^{+\infty} f(t)e^{-i\omega t} dt \quad \omega \in (-\infty, +\infty) \quad (\text{A.1})$$

where i is the imaginary unit and ω is the frequency.

In the case of having only N samples over one period of the function ($f(t_n) = f(n\Delta t) = f[n]$, $n = 0, \dots, N-1$), $f(t)$ can be approximated by a sum of finite impulses:

$$f(t) = \sum_{n=0}^{N-1} \delta(t - t_n) f(t_n) \quad (\text{A.2})$$

where $\delta(t - t_n)$ is the *Dirac delta function* and $t_n = n\Delta t$. Substituting and operating:

$$F(\omega) = \int_{-\infty}^{+\infty} \sum_{n=0}^{N-1} \delta(t - t_n) f(t_n) e^{-i\omega t} dt = \sum_{n=0}^{N-1} f(t_n) e^{-i\omega t_n} \quad (\text{A.3})$$

where $\omega = 2\pi f$. Having only N sample points, only N fundamental frequencies can be studied. Hence:

$$F(f) = \sum_{n=0}^{N-1} f(n\Delta t) e^{-i2\pi f n \frac{T_1}{N}} \quad (\text{A.4})$$

Expressing the multiples of the minimum frequency by $f_k = kf_1$, ($k = 0, \dots, N-1$) and remembering that $f_1 T_1 = 1$ it remains:

$$F[k] = \sum_{n=0}^{N-1} f[n] e^{-i2\pi k \frac{n}{N}}, \quad (k = 0, \dots, N-1) \quad (\text{A.5})$$

$F[k]$ is the Discrete Fourier Transform of the sequence $f[n]$. It represents the frequency amplitudes constituting the frequency spectrum of the original signal. The set of N amplitudes (which in general can be complex numbers) are evaluated at angular frequencies: $\frac{2\pi k}{N\Delta t}$, $k = 0, \dots, N-1$.

The previous equation can be written in matrix form:

$$\begin{Bmatrix} F[0] \\ F[1] \\ F[2] \\ \vdots \\ F[N-1] \end{Bmatrix} = \begin{bmatrix} 1 & 1 & 1 & 1 & \dots & 1 \\ 1 & W_N^{-1} & W_N^{-2} & W_N^{-3} & \dots & W_N^{-(N-1)} \\ 1 & W_N^{-2} & W_N^{-4} & W_N^{-6} & \dots & W_N^{-2(N-1)} \\ 1 & W_N^{-3} & W_N^{-6} & W_N^{-9} & \dots & W_N^{-3(N-1)} \\ \vdots & \vdots & \vdots & \vdots & \ddots & \vdots \\ 1 & W_N^{-(N-1)} & W_N^{-2(N-1)} & W_N^{-3(N-1)} & \dots & W_N^{-(N-1)(N-1)} \end{bmatrix} \begin{Bmatrix} f[0] \\ f[1] \\ f[2] \\ \vdots \\ f[N-1] \end{Bmatrix} \quad (\text{A.6})$$

where $W_N = e^{\frac{i2\pi}{N}}$, $W_N^k = e^{\frac{i2\pi k}{N}}$, $k = 0, \dots, N-1$ and $W_N^{kN} = 1$, $k = 0, \dots, N-1$.

A.2 MOID evolution DFT

The Discrete Fourier Transform (DFT) is used in order to convert the finite number of MOID samplings taken at equidistant instant of time into a complexed-value function of frequency. Applying the DFT theory to the MOID evolution frequency spectrum study, it is important to very well define the sampled data and the interesting frequencies.

As said in the previous section, the DFT is rigorously applied to periodic functions. In this case thus, an assumption is made and it correspond to consider the MOID evolution function as 1-day-periodic although it is not necessary true. The MOID function DFT is then applied to a collection of N discrete samplings corresponding to one *period* of it. From this point of view, the *base period* of MOID evolution is thus:

$$T_1 = 86\,400 \text{ s} \quad (\text{A.7})$$

while the *sample period* is:

$$\Delta t = 1 \text{ s}. \quad (\text{A.8})$$

The sample size is then $N = 86400$, corresponding the the 86 400 MOIDs evaluated one every second during one day. The sample points are $t_n = n\Delta t$, $n = 0, \dots, N - 1$, while the sampled values are $x[n] = x(t_n)$, $n = 0, \dots, N - 1$.

The DFT is calculated¹⁷:

$$X_k = \frac{1}{\sqrt{N}} \sum_{n=0}^{N-1} x[n] e^{-i2\pi k \frac{n}{N}} \in \mathbb{C}, \quad (k = 0, \dots, N - 1) \quad (\text{A.9})$$

in a rigorous sense, it corresponds to the function x_n which is obtained by the *inverse transform* and which is not exactly the *same* MOID function of the beginning:

$$x_n = \frac{1}{\sqrt{N}} \sum_{k=0}^{N-1} X_k e^{i2\pi k \frac{n}{N}} \in \mathbb{R}, \quad (n = 0, \dots, N - 1) \quad (\text{A.10})$$

It is important to observe that the DFT base frequency is $f_1 = \frac{1}{T_1}$ because of the very assumption that have been made. All the resulting frequencies will be thus expressed as multiples of it. The base frequency is a fictitious *fundamental frequency* when the signal is not T_1 -periodic, then, it must not be considered in the count of the *fundamental frequencies*. They are the frequencies which determine the MOID oscillatory behaviour in the short period, and f_1 is clearly not one of them.

The l possible *fundamental frequencies* f_i which may appear in the DFT analysis are given by the following relation:

$$f_i = \frac{n_i}{T_1}, \quad i = 1, \dots, l \quad (\text{A.11})$$

where

$$n_i = \min_k \left\{ |X_k| \gg 0 : k > n_{i-1}, \frac{k}{n_{i-m}} \notin \mathbb{N} \quad \forall 1 \leq m < i - 1 \right\} \quad (\text{A.12})$$

This means that the possible fundamental frequencies constituting the MOID function must satisfy the following conditions:

¹⁷The DFT leaves some freedom in the choice of the frequencies amplitude set normalization value. *MAPLE* software utilises $\frac{1}{\sqrt{N}}$ as normalization value for the DFT and the *inverse transform* default functions. It is important to remember this normalization when analysing the graphics of section 5.2.

1. The X_k complex number representing the k frequency amplitude must have a positive modulus and must be very well *identifiable* respect to the rest of the *almost null* moduli of the series.
2. The k frequency amplitude index must be higher than the prior identified fundamental frequency index.
3. The k frequency amplitude index must not be multiple of any of the previous identified fundamental frequencies indexes.

All the frequencies satisfying the first two conditions but not the third (i.e., they are multiple of any of the fundamental frequencies), are called *harmonics* and they are numbered according to their corresponding multiplier (i.e., the double of the fundamental frequency is the *second harmonic*, etc.). Obviously, all the frequencies will appear as multiple of the base frequency f_1 , but, as said in the previous explanation, this is a necessary consequence of the theory assumptions.

Appendix B DROMO Asymptotic Solution

The asymptotic solution developed by Sánchez Fernández-Mellado [25] is based on the on the simplification represented by the *main problem* formulation. Considering only the J_2 coefficient of the geopotential expansion, the asymptotic solution looks for an analytical DROMO formulation for orbit propagation. Once set up, the new formulation could suppose large savings in terms of propagation time. This makes the asymptotic solution suitable to be applied to the problem of the rapid propagation of large amounts of space debris.

B.1 Asymptotic solution theory

The ε term which was introduced in section 3.4.1:

$$\varepsilon = J_2 \left(\frac{R_\oplus}{L_c} \right)^2 \quad (\text{B.1})$$

is little (10^{-3}) compared to the main term of the Earth's gravitational field spherical expansion which is of order unity. If the only term in the gravitational perturbation is the one containing J_2 , as described in section 3.2, it means that the exact solution of the DROMO formulation of the *main problem* is still an approximate solution. From this viewpoint, even the *exact* solution of the equations will not be pursued, and an asymptotic solution to solve the *main problem* is presented [25].

The objective in this case is to analytically solve the equations of motion described in the DROMO theory, saving the time of a numerical propagation. In order to do so, the asymptotic solution consists in the following approximation of DROMO variables:

$$\begin{aligned} \tau &= \tau^{(0)} + \varepsilon\tau^{(1)} + \dots & \eta_1 &= \eta_1^{(0)} + \varepsilon\eta_1^{(1)} + \dots \\ \zeta_1 &= \zeta_1^{(0)} + \varepsilon\zeta_1^{(1)} + \dots & \eta_2 &= \eta_2^{(0)} + \varepsilon\eta_2^{(1)} + \dots \\ \zeta_2 &= \zeta_2^{(0)} + \varepsilon\zeta_2^{(1)} + \dots & \eta_3 &= \eta_3^{(0)} + \varepsilon\eta_3^{(1)} + \dots \\ \zeta_3 &= \zeta_3^{(0)} + \varepsilon\zeta_3^{(1)} + \dots & \eta_4 &= \eta_4^{(0)} + \varepsilon\eta_4^{(1)} + \dots \end{aligned} \quad (\text{B.2})$$

The work presented in [25] develops the expansion for the first two terms of the asymptotic solution starting from the pericenter position. It obtains an approximate solution which neglects 10^{-6} order terms. This approximation is consistent with the *main problem* formulation, it in fact already neglects terms of the same order. The approximation is thus the same of the *exact* solution for the DROMO equations but leads to a considerable gain of time.

Here are summarized the expansion terms presented in the work.

First of all, the order 0 terms are quite trivial to define, because (except for the non-dimensional time) they are constant and depend only on the initial condition:

$$\begin{aligned} \zeta_1^{(0)} &= \zeta_{10}, & \zeta_2^{(0)} &= \zeta_{20}, & \zeta_3^{(0)} &= \zeta_{30} \\ \eta_1^{(0)} &= C_1, & \eta_2^{(0)} &= C_2, & \eta_3^{(0)} &= C_3, & \eta_4^{(0)} &= C_4 \end{aligned} \quad (\text{B.3})$$

The non-dimensional time term instead requires a deeper definition, being a function of the orbit's eccentric anomaly u :

$$\tau^{(0)}(u) = \frac{1}{\zeta_{30}^3 (1 - e_0^2)^{3/2}} (u - e_0 \sin u) \quad (\text{B.4})$$

For the ε order terms, their value is obtained in [25] through a symbolic manipulator. Again, every term apart from the non-dimensional time has a common definition. For this reason they are presented with the following expression:

$$\begin{pmatrix} \zeta_1^{(1)} \\ \zeta_2^{(1)} \\ \zeta_3^{(1)} \\ \eta_1^{(1)} \\ \eta_2^{(1)} \\ \eta_3^{(1)} \\ \eta_4^{(1)} \end{pmatrix} = \mathcal{A} \begin{pmatrix} 1 \\ \sigma - \sigma_0 \\ \cos \sigma - \cos \sigma_0 \\ \cos(2\sigma) - \cos(2\sigma_0) \\ \cos(3\sigma) - \cos(3\sigma_0) \\ \cos(4\sigma) - \cos(4\sigma_0) \\ \cos(5\sigma) - \cos(5\sigma_0) \\ \sin \sigma - \sin \sigma_0 \\ \sin(2\sigma) - \sin(2\sigma_0) \\ \sin(3\sigma) - \sin(3\sigma_0) \\ \sin(4\sigma) - \sin(4\sigma_0) \\ \sin(5\sigma) - \sin(5\sigma_0) \end{pmatrix}, \quad \mathcal{A} = \begin{bmatrix} A_{1,1} & A_{1,2} & \dots & A_{1,12} \\ A_{2,1} & A_{2,2} & \dots & A_{2,12} \\ \vdots & \vdots & \ddots & \vdots \\ A_{7,1} & A_{7,2} & \dots & A_{7,12} \end{bmatrix} \quad (\text{B.5})$$

where \mathcal{A} is a matrix of 7×12 size which only depends on the initial conditions. The value of its coefficients is detailed in [25].

The non-dimensional time term, as in the case of 0 order, has a specific and more complicated definition, its expression being the following:

$$\tau^{(1)} = \sum_{i=0}^5 g_i(\sigma) \quad (\text{B.6})$$

where the g_i terms are function of the ideal anomaly σ and they are hereby expanded. The value of the H_i terms intervening in the definitions of the g_i terms are collected in [25] as well.

$$\begin{aligned} g_0(\sigma) &= -\frac{H_0}{16} \cdot \frac{1}{(1 - e_0^2)^{5/2}} \cdot \left[\frac{1}{2}(2 + e_0^2)u - 2e_0 \sin u + \frac{1}{4}e_0^2 \sin(2u) \right] \\ g_1(\sigma) &= -\frac{H_1}{16} \cdot \frac{1}{(1 - e_0^2)^{5/2}} \cdot \left[-\frac{3}{2}e_0 u + (1 + e_0^2) \sin u - \frac{1}{4}e_0 \sin(2u) \right] \\ g_2(\sigma) &= -\frac{H_2}{16} \cdot \frac{1}{(1 - e_0^2)^2} \cdot \left[1 - \cos u + \frac{1}{4}e_0(\cos(2u) - 1) \right] \\ g_3(\sigma) &= -\frac{H_3}{16} \cdot \frac{1}{(1 - e_0^2)^{5/2}} \cdot \left[\frac{3}{2}e_0^2 u - 2e_0 \sin u + \frac{1}{4}(2 - e_0^2) \sin(2u) \right] \\ g_4(\sigma) &= -\frac{H_4}{16} \cdot \frac{1}{(1 - e_0^2)^2} \cdot \left[2e_0(\cos u - 1) + \frac{1}{2}(1 - \cos(2u)) \right] \\ g_5(\sigma) &= -\frac{H_5}{16} \cdot \frac{1}{2} \cdot \frac{1}{(1 - e_0^2)^{3/2}} \cdot \left[\sigma(u) \frac{(1 - e_0 \cos u)^2}{(1 - e_0^2)^{1/2}} - u + e_0 \sin u \right] \end{aligned} \quad (\text{B.7})$$

B.2 Application and results

The *asymptotic solution propagator*, has been programmed and tested in a *C++* routine in order to proof its validity and efficiency.

The routine is intended to substitute the *DROMO numeric propagator* once it is perfectly set up and validated. It would be used for the MOID evolution study as described in this work. The

modularity of the DROMOID tool in fact, ensures the ability to change either the propagator or the MOID computation tool in a rapid way.

The *asymptotic solution propagator* needs to be reliable and fast. In order to check its validity, the results obtained with it are compared with two other propagators: a traditional Cowell's method propagation, implemented through a 4th order Runge-Kutta integrator and the *DROMO numeric propagator* (which will be called *DROMO propagator*) implemented through the same RK4 integrator.

The asymptotic solution routine, implemented as a function called in the main program, is a relatively simple one. It is needed to analytically calculate the final state vector of the propagation. In the main code, the object state vector is firstly converted in DROMO variables as seen in section 3.3.3. It is then inserted as an argument to the *Asymptotic Solution* function. After the propagation, the vector is transformed from DROMO variables to a state vector in the inertial frame. The whole process is included in the computation time because the two conversions are part of the calculation. The function uses the initial conditions to calculate only once the 0 order solution as well as the A_{ij} and H_i coefficients. The asymptotic solution, after the initialization of all the constants, is able to evaluate the final DROMO vector.

The Cowell's method propagator is implemented with a function called in the main program as well. It receives the initial state vector in the inertial frame, not needing any conversion. The state vector is propagated for the considered time and it is finally presented as an output of the function. In this case, only the propagation time is included in the whole computation time.

The DROMO propagator is implemented in the code as another function called by the main program. After having converted the state vector in DROMO variables, it is given to the function which propagates it for the specified time. The function returns the final DROMO vector, which needs to be converted into an inertial state vector. Again, the double conversion of the vectors is considered in the propagation time computation, being the two operations essential for the result.

It is possible to make a comparison between the three propagation tools in order to evaluate the benefits of each one of them. A sample state vector is presented:

Table 6: Sample LEO object.

| Initial state vector | |
|----------------------|--|
| x | 2568.067 822 101 631 00 |
| y | 5574.251 441 585 716 70 km |
| z | 3543.409 444 444 444 90 |
| v_x | 3.314 425 337 758 61 |
| v_y | -5.740 753 082 891 55 km s ⁻¹ |
| v_z | 6.628 850 675 517 22 |

This vector is propagated for 1 day (86 400 s) by the different routines and the results are compared in terms of precision and computational time. The final error is computed in terms of the position and velocity relative error after the propagation. The DROMO propagator is taken as a reference, being it the most accurate method. The computational time is calculated following the aforementioned rules.

Table 7: Comparison after 1 day propagation.

| | Cowell's method | DROMO propagator | Asymptotic solution | |
|-----------|-----------------|------------------|---------------------|--------------------|
| x | -453.598 36 | -453.439 | -329.9059 | |
| y | -18 869.539 | -18 869.318 | -18 710.335 | km |
| z | 1962.491 | 1962.7339 | 2157.5694 | |
| v_x | -1.821 086 2 | -1.821 088 5 | -1.821 280 2 | |
| v_y | -2.524 197 6 | -2.524 294 | -2.604 796 1 | km s^{-1} |
| v_z | -2.775 642 7 | -2.775 632 6 | -2.763 677 7 | |
| Pos. err. | 365.0165 | - | 280 172.97 | m |
| Vel. err. | 0.096 955 | - | 81.385 161 | m s^{-1} |
| Time | 1 885 488 | 43 971 | 6774 | μs |

In the above comparison table, the different precisions of the methods are compared against the DROMO propagator. It can be seen that Cowell's method has a very little error while the asymptotic solution presents a far bigger one. Nevertheless, it is observed how the Asymptotic solution constitutes a big gain of time (one order of magnitude lower than the DROMO propagator computational time), compared to Cowell's method, which has a computational time of two orders of magnitude higher than DROMO propagator.

In the following graphics, the three methods are visually compared in terms of the position vector modulus and the velocity vector modulus time evolutions. The Cowell's method completely overlaps the DROMO propagator vector evolutions, thus only two curves are visible.

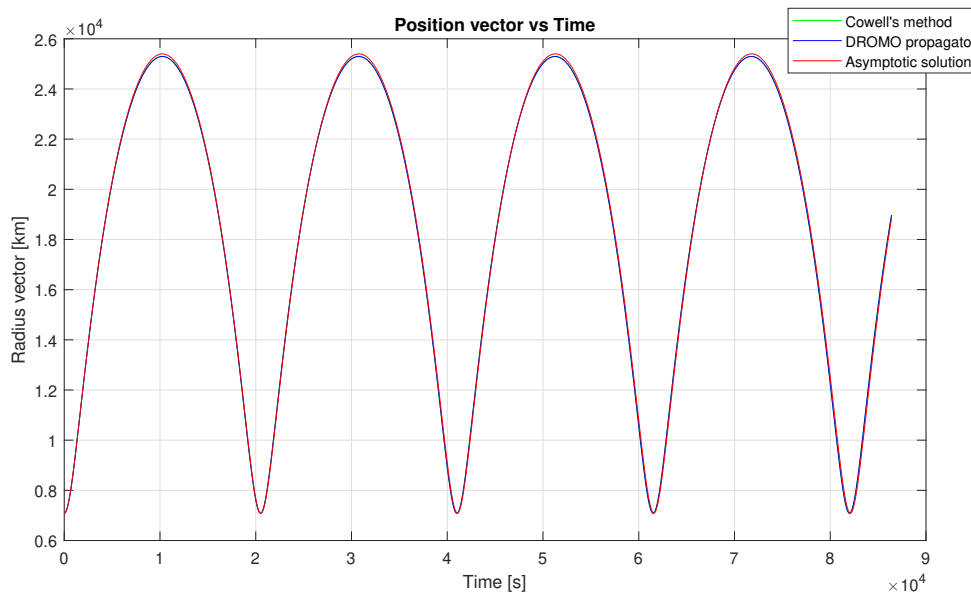


Figure B.1: Radius vector

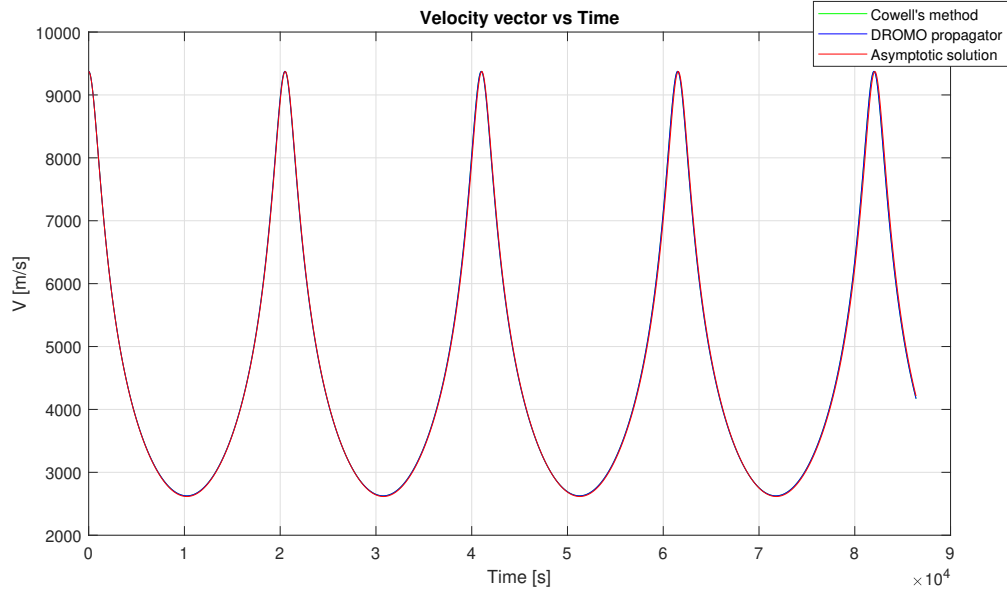


Figure B.2: Velocity vector

As can be seen in the Fig. B.1 and Fig. B.2, the asymptotic solution represents a good approximation of the satellite evolution over time. Nevertheless a computation of the error evolution over one day time has been done in order to understand how the error is propagated. Again, the DROMO propagator has been considered as a reference and the error has been evaluated for the asymptotic solution and for Cowell's method. The errors computations have been done according to the following relations:

$$\begin{aligned}
 \Delta \mathbf{r} &= \frac{|\mathbf{r} - \mathbf{r}_{\text{DROMO}}|}{|\mathbf{r}_{\text{DROMO}}|} & \Delta \mathbf{r} [\%] &= \frac{|\mathbf{r} - \mathbf{r}_{\text{DROMO}}|}{|\mathbf{r}_{\text{DROMO}}|} \cdot 100 \\
 \Delta \mathbf{v} &= \frac{|\mathbf{v} - \mathbf{v}_{\text{DROMO}}|}{|\mathbf{v}_{\text{DROMO}}|} & \Delta \mathbf{v} [\%] &= \frac{|\mathbf{v} - \mathbf{v}_{\text{DROMO}}|}{|\mathbf{v}_{\text{DROMO}}|} \cdot 100
 \end{aligned} \tag{B.8}$$

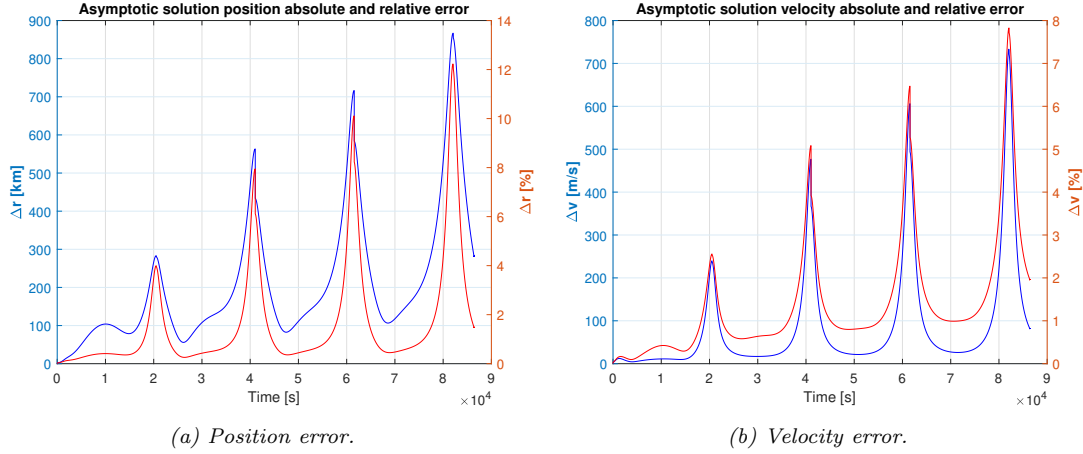


Figure B.3: Asymptotic solution error evolution over 1 day.

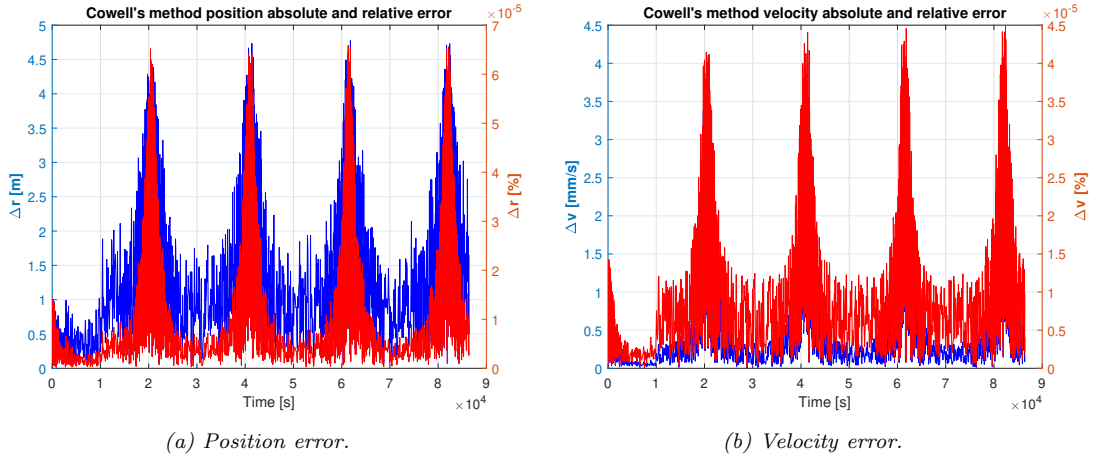


Figure B.4: Cowell's method error evolution over 1 day.

As can be seen in the above images, the position error for the DROMO asymptotic solution appears to be very high and it presents an overall increase over time. On the contrary, the Cowell's numeric solution position error appears to be very low and does not present an overall increase during time¹⁸. The same behaviour appears in the velocity error evolution.

The actual version of the Asymptotic solution software presents an unacceptable error propagation, not allowing its implementation in the current DROMOID tool. It needs to be further developed and consolidated. Once the solution is completed and successfully tested, it would imply a considerable gain of propagation time coupled to accuracy preservation, as its approximation is of the same order of that of the *main* problem simplification.

¹⁸The drop in the error curve which appears almost every 20000 seconds in Fig. B.3a is due to an error in the program when it resets the σ angle every orbit (in order to maintain it in the $[0, 2\pi]$ interval).

References

- [1] https://www.esa.int/Our_Activities/Space_Safety/Space_Debris/Space_debris_by_the_numbers
- [2] NASA Orbital Debris Program Office, *Orbital Debris Quarterly News*, 11(2), (April 2007).
- [3] NASA Orbital Debris Program Office, *Orbital Debris Quarterly News*, 13(2), (April 2009).
- [4] NASA Orbital Debris Program Office, *Orbital Debris Quarterly News*, 23(1&2), (May 2019).
- [5] Dana M. Lear and Eric L. Christiansen and James L. Hyde and Jeph Herrin and Frances Lyons and Justin Hamilton Kerr and Silke Ryan, *Investigation of Shuttle Radiator Micro-Meteoroid & Orbital Debris Damage*, AIAA 2009-2361, (2009).
- [6] ESA, *SPACE DEBRIS: THE ESA APPROACH*, ESA publications Brochures, BR-336, (March 2017).
- [7] T. S. Kelso, S. Alfano, *Satellite orbital conjunction reports assessing threatening encounters in space (SOCRATES)*, Modeling, Simulation, and Verification of Space-based Systems III, vol. 6221, International Society for Optics and Photonics, (2006).
- [8] Felix R. Hoots, Linda L. Crawford, and Ronald L. Roehrich: *An analytic method to determine future close approaches between satellites*, *Celestial Mechanics*, 33(2), 143-158, (1984).
- [9] <https://celestrak.com/NORAD/documentation/>
- [10] David A. Vallado, Paul J. Cefola: *Two-Line Element Sets - Practice and Use*, IAC-12-A6.6.11, 63rd International Astronautical Congress, Naples, Italy, (2012).
- [11] David A. Vallado, Paul Crawford, Richard Hujak and T. S. Kelso: *Revisiting Spacetrack Report #3: Rev 2*, AIAA-2006-6753-Rev2, (2006).
- [12] <https://celestrak.com/columns/v04n03/>
- [13] Felix R. Hoots, Ronald L. Roehrich: *SPACETRACK REPORT NO.3 Models for Propagation of NORAD Element Sets*, (1980).
- [14] Felix R. Hoots, Paul W. Schumacher Jr and Robert A. Glover: *A History of the Analytical Orbit Modelling in the United States Space Surveillance System*, (2004).
- [15] Michael F. Henry: *The OrbitTools Libraries. NORAD SGP4/SDP4 Implementations in C++ and C#*, <http://www.zeptomoby.com/satellites/>
- [16] David A. Vallado, Paul Crawford: *SGP4 Orbit Determination*, AIAA-2008-6770, (2008).
- [17] David A. Vallado, Wayne D. McClain: *Fundamentals of Astrodynamics and Applications*, Springer, New York, (2007).
- [18] Sean E. Urban, P. Kenneth Seidelmann, *Explanatory Supplement to the Astronomical Almanac*, University Science Books, (2013).
- [19] International Astronomical Union: *Standards of Fundamental Astronomy*, <http://www.iausofa.org/>
- [20] William E. Wiesel: *Modern Astrodynamics*, Aphelion Press, (2010).

- [21] André Deprit, Arnold Rom: *The main problem of artificial satellite theory for small and moderate eccentricities*, *Celestial Mechanics*, 2(2), (1970).
- [22] Hodey Urrutxua, Manuel Sanjurjo-Rivo Jesús Peláez: *DROMO propagator revisited*, *Celestial Mechanics & Dynamical Astronomy*, 124(1), 1-31, (2016).
- [23] José M. Hedo, Manuel Ruíz and Jesús Peláez: *On the minimum orbital intersection distance computation: a new effective method*, *Monthly Notices of the Royal Astronomical Society*, 479(3), 3288-3299 (2018).
- [24] Willian L. Briggs et Al.: *The DFT An Owner's manual for the Discrete Fourier Transform*, Society for Industrial and Applied Mathematics, Philadelphia, 45, 1995.
- [25] Luis Sánchez Fernández-Mellado: *Desarrollo de un propagador orbital a partir de una aproximación asintótica de la Teoría DROMO aplicado a un planificador de pases. Master's thesis, Escuela Técnica Superior de Ingeniería Aeronáutica y del Espacio, UPM, Madrid, (2016).*